NEW MATERIALS FOR ECO-SUSTAINABLE ELECTROCHEMICAL PROCESSES: OXYGEN EVOLUTION REACTION AT DIFFERENT ELECTRODE MATERIALS

Francesca Ferrara

DOTTORATO DI RICERCA IN INGEGNERIA INDUSTRIALE
UNIVERSITÀ DEGLI STUDI DI CAGLIARI
XX CICLO

NEW MATERIALS FOR ECO-SUSTAINABLE ELECTROCHEMICAL PROCESSES: OXYGEN EVOLUTION REACTION AT DIFFERENT ELECTRODE MATERIALS

FRANCESCA FERRARA

Supervisor:
Prof. Simonetta Palmas

Dottorato di Ricerca in Ingegneria Industriale
Università degli Studi di Cagliari
XX Ciclo

Acknowledgements

I wish to thank Prof. Simonetta Palmas for her support and precious advice during this three years.

I would like to express my deep gratitude to Prof. Anna Maria Polcaro for giving me the opportunity to work in her research group, for her advice and helpful discussions.

I’m very grateful to my colleagues: Michele Mascia, Annalisa Vacca and Jesus Rodriguez Ruiz.

Thanks also to the research group of Prof. Piccaluga (Dipartimento di Scienze Chimiche di Cagliari), the research group of Prof. Cocco (Dipartimento di Chimica di Sassari) and the research group of Prof. Anedda (Dipartimento di Fisica di Cagliari) for the useful collaborations.

Finally, my highest appreciation is addressed to Francesco and my family.

Contents

Abstract 10

Chapter 1 - Introduction.. 14

1.1 Introduction 16
1.2 References 22
1.3 Thesis Organization.. 26
1.4 Publications and presentations... 27

Chapter 2 - General aspects of electrochemical processes................................ 32

2.1 Introduction 34
2.2 The electrical double layer.. 35
2.3 Faradaic processes 37
2.3.1 The Butler-Volmer equation 39
2.4 References 43

Chapter 3 - Electrochemical techniques.. 44

3.1 Introduction 46
3.2 Cyclic voltammetry 48
3.2.1 Reversible electrode systems 51
3.2.2.Irreversible electrode systems... 53
3.2.3 Quasi-reversible systems 54
3.2.4 Electrochemical porosity and morphology factor 54
3.3 Steady-state polarisation.. 59
3.4 Electrochemical impedance spectroscopy 62
3.4.1 Common Equivalent Circuit Models 69
3.4.2 EIS and Mott-Schottky analysis.. 76
3.5 References 82

Chapter 4 - Active electrodes in alkaline media: Cobalt oxide electrodes 84

4.1 Introduction 86
4.2 Experimental conditions... 88
4.3 Results and discussion 90
4.3.1 Physicochemical analysis 90

4.3.2 Electrochemical analysis ... 91
4.3.2.1 Open circuit potential ... 91
4.3.2.2 Cyclic voltammetric studies ... 92
4.3.2.3 Steady-state polarisation analysis ... 95
4.3.2.4 Morphology factor of the sol-gel Co_3O_4 electrodes ... 98
4.3.2.5 EIS analysis at sol-gel Co_3O_4 electrodes ... 100
4.3.2.6 Modeling of OER at sol-gel Co_3O_4 electrodes. ... 107
4.4 Conclusions ... 121
4.5 References ... 122

Chapter 5 - Active electrodes in acid media: Sn-Ru oxide electrodes ... 126
5.1 Introduction ... 128
5.2 Experimental conditions ... 131
5.3 Results and Discussion ... 132
5.3.1 Physicochemical analysis ... 132
5.3.2 Electrochemical analysis ... 134
5.3.2.1 Cyclic voltammetric studies ... 134
5.3.2.2 Steady-state polarisation analysis ... 137
5.3.2.3 Electrochemical impedance spectroscopy analysis ... 139
5.3.2.4. Preliminary investigation at RuO_2-SnO_2 mixed oxide systems ... 147
5.4 Conclusions ... 149
5.5 References ... 150

Chapter 6 - Non-active electrodes: Boron-doped diamond ... 154
6.1 Introduction ... 156
6.2 Experimental conditions ... 157
6.3 Results and discussion ... 159
6.3.1 Relationship between electrochemical activity and ageing time at highly doped BDD sample. ... 159
6.3.2 Relationship between electronic structure and electrochemical activity ... 171
6.3.2.1 Mott-Shottky analysis - Runs in sulphuric acid ... 171
6.3.2.2 Electrochemical activity – Runs in ferro/ferri cyanide ... 178
6.4 Conclusions ... 185
6.5 References ... 187

Chapter 7 - Conclusions ... 192

Table of symbols ... 197

Abstract

In this Thesis, the issue concerns the study of the oxygen evolution reaction *(OER)* at different electrode materials. The idea to carry out such research is connected with the key role, which oxygen evolution reaction plays in several electrochemical processes.

In a future energy scenario based on renewable energy, hydrogen is an attractive energy carrier. Among the others, hydrogen production by water electrolysis is a clean and simple way of storing energy from sources such as solar, wind and hydroelectric power. The hydrogen can then subsequently be utilized in fuel cells without concern of contaminants such as carbon monoxide. In this contest water electrolysis acquires a particular strategic role. Oxygen evolution reaction is very often the most difficult of the two electrolytic reactions in an electrochemical cell, so that the cell voltage is governed by that of the anodic reaction and the nature of the anodic material strongly influences the process selectivity and efficiency.

Moreover, oxygen evolution reaction is the most important side reaction of many other electrochemical applications such as electrosynthesis, incineration of organic pollutants for wastewater treatment and water disinfection.

Many catalytic materials for this reaction have been proposed in literature: depending on the case, either “active” or “non-active” electrodes can be used at which the reaction mechanism of oxygen evolution may be very different. At active electrodes, a strong interaction with hydroxyl radicals exists and the oxygen evolution reaction occurs via the formation of higher oxides. In contrast, at non active electrodes, the substrate does not participate in the process and the oxidation is assisted by hydroxyl radicals that are weakly adsorbed at the electrode surface.

In this work, the performances of both “active” and “non-active” electrodes have been evaluated. The criterions for choosing electrode materials for industrial

applications are based mostly on a compromise between electrocatalytic activity, long-term stability and cost. This work is addressed to clarify some of these aspects at different electrodes in light of the results obtained.

The attention has been firstly paid on the spinel-type Co_3O_4 electrodes obtained by a sol-gel method. The literature reports several studies on these electrodes showing good efficiency and long-term performance in alkaline solutions but, in spite of the large number of publications devoted to these electrodes, the mechanism of oxygen evolution on these anodes is still a matter of discussion. So, the properties of the sol-gel Co_3O_4 sample were firstly compared with those of commercial nanosized Co_3O_4 powder samples. Then, the attention has been paid on the sol-gel Co_3O_4 sample to obtain specific information about mechanism and kinetics of the oxygen evolution reaction at this electrode material. In particular, the relationships between Faradaic admittance equation, equivalent circuit and kinetic parameters have been derived.

Moreover, the behaviour of SnO_2 and SnO_2-RuO_2 electrodes, mechanically processed for different times, was investigated in acid media during oxidative runs. RuO_2 is known as the most active oxide for anodic oxygen evolution, however it suffers from instability and therefore should be stabilised with another oxide such as SnO_2. SnO_2 represents the search for a compromise between electrocatalytic activity, long-term electrode stability and cost. It is a relatively cheap oxide capable of stabilizing the electrode and partly producing catalytic effects. Many researchers activities are oriented toward preparing coatings containing high level of SnO_2 and, in recent years, to utilize SnO_2 as the main additive to the coatings or to obtain SnO_2-based active coatings is still one of the most studied topics. The preparation techniques affect the properties of the oxide layers so, the SnO_2-based electrodes prepared for the present work have been used to obtain information on the electrochemical properties of mechanically-processed powders and, in turn, on the modification of their chemical reactivity as a consequence of the accumulation of lattice defects.

Finally, the attention has been focused on the evolution of electronic structure and electrochemical activity of boron doped diamond *(BDD)* samples during oxidative ageing tests. The attention which boron doped diamond, with different levels of doping, has attracted in this last decade is so great that a new branch, known as the electrochemistry of diamond, has been opened. Despite this, many questions are still open and the comprehension of the electrochemical behaviour of *BDD* is not yet completely achieved. Actually, several factors may heavily influence the electrochemical performance of this material and an objective comparison between them is hard, due to the lack of a standard diamond electrode material to compare results against. So, an experimental study has been started in our laboratory to investigate the effect of an oxidative process on the structure of a highly doped *BDD* sample and then, the study has been extended to less doped samples. The study has been completed by an investigation of the capacitance-voltage characteristics that allowed calculation of the flat band potential and the energetic levels of conduction and valence bands of diamond, very important parameters in understanding the evolution of the sample behaviour with time.

Chapter 1

Introduction

1.1 Introduction

Energy is the most important issue of the 21st century. Despite the situation is complex and controversial, it is well known that the use of fossil fuels causes problems connected with source availability as well as with environmental compatibility.

Electrocatalysis can be the best way to bridge the global energy supply between the present era of fossil fuels and the future era based on hydrogen economy. Hydrogen is coming to become an important part of future energy systems: it is only needed to prepare electrocatalysts that will evolve hydrogen with the lowest possible energy consumption and later to use that hydrogen in fuel cells with minor voltage losses.

By using water electrolysis, the hydrogen can be produced efficiently without environmental impact if renewable energies, such as solar, wind and hydroelectric power are used as the power source and fuel cells have proved to be an interesting and very promising alternative to solve the problem of clean electric power generation with high efficiency [1]. The only input to this “energy cycle” is the clean renewable energy and the only output is electric power.

In this contest water electrolysis acquires a particular strategic role. Improvements of the performance and efficiency of water electrolysis cells can be made by using suitable and effective electrocatalysis: consequently, the search of more suitable materials to reduce both cathode and anode overpotentials has increased considerably. Various aspects of electrocatalysis must be reviewed and not only one property should be used for characterising and understanding the electrocatalysis process. Active surface area, specific activity, electronic resistance and particle/layer structure are all important properties which need to be optimised in order to achieve high efficiency and performance.

The oxygen evolution reaction (*OER*) is one of the most important technological reactions in electrochemistry taking place at the anode of water electrolysers.

$$Anode: 2H_2O \rightarrow 4H^+ + O_2 + 4e^- \tag{1.1}$$

$$Cathode: 4H^+ + 4e^- \rightarrow 2H_2 \tag{1.2}$$

$$Cell: 2H_2O \rightarrow 2H_2 + O_2 \tag{1.3}$$

OER is very often the most difficult of the two electrolytic reactions in an electrochemical cell, so that the cell voltage (i.e. the energy consumption of the process) is governed by that of the anodic reaction.

Although a significant amount of research work has dealt with *OER* [2, 3], the interest in the different aspects of its kinetics and mechanism still continues. It is well established that *OER* results from reactions in series and hydroxyl radicals are one of the most important intermediates produced during *OER*.

The first common step is the discharge of water molecules to hydroxyl radicals:

$$M + H_2O \rightarrow M\,(\bullet OH) + H^+ + e^- \qquad (1.4)$$

where M designates an active site at the anode surface.

The following steps depend on the strength of the interaction between hydroxyl radicals and the electrode surface which, in turn, depends on the nature of the electrode material. From this, two classes of materials can be distinguished: "active" or "non-active" electrodes [4-6]. It is well established that at active electrodes, a strong interaction with hydroxyl radicals exists and the oxygen evolution reaction occurs via the formation of higher oxides. In contrast, at non active electrodes, the substrate does not participate in the process and the oxidation is assisted by hydroxyl radicals that are weakly adsorbed at the electrode surface.

So, the nature of the anodic material strongly influences the process selectivity and efficiency. For this reason, by developing the electrocatalytic material used for oxygen evolving electrodes, great improvements in efficiency can be achieved. But the selection of electrode materials is not at all an easy task.

As “active” materials are concerned, according to the literature, a conflict of technical and economical issues may be evidenced: the best performing electrocatalysts as, e.g. Pt, Pd, Ru are expensive, while the cheaper substituents using less noble metals as, e.g. Ni, Co etc. suffer of corrosion, passivation or similar problems [7].

In particular, conductive metallic oxide electrodes have been considered at which oxygen overvoltage can be efficiently decreased. The interest in pure and mixed oxide layers was greatly increased after the introduction of dimensionally stables anodes (*DSA*®) [8] not only into the chloro-alkali industry but also into *OER*. The terminology “dimensionally stable anode” emphasizes the stability of these electrodes toward chemical and electrochemical deterioration. *DSAs* consist of an active transition metal oxide (RuO_2, IrO_2, Co_3O_4, perovskites, etc.) stabilized by a valve metal oxide (typically TiO_2, ZrO_2, SnO_2, Ta_2O_5, etc.). Although very comprehensive studies of the structural and electrochemical properties of *DSA* oxides have been carried out, an objective comparison between them is hard, because the wide range of preparation conditions affect the formation and properties of *DSA*-type oxide layers [9].

Tseung [10] and Trasatti [9] put forward guidelines for the choice of oxide electrodes for the oxygen evolution reaction. They emphasized that oxygen evolution can only proceed when the electrode potential is higher than the potential of the metal/metal oxide couple or the lower metal oxide/higher metal oxide couple. Thus the ideal couple should have potential lower or similar to the theoretical potential of the oxygen evolution reaction.

Moreover, the criterions for choosing mixed oxide electrode materials for industrial applications, which are based mostly on a compromise between electrocatalytic activity, long-term stability and cost, have led to the development of new anode materials.

However, the range of improvement of the activity of a mono-oxide can be rather limited. So mixed oxides are used to modulate the electrode properties through synergetic effects arising from the intimate electronic interaction of the components [11-12]. Since synergetic effects are possible as two or more oxides are mixed together, several studies of mixed oxides for electrochemical applications may be found in the literature [13-16]. In particular, the use of oxide anodes for *OER* in strongly acid media still demands improved materials, especially with respect to long-term performance [17]. Few oxides can withstand strongly oxidative conditions in acid environments: they are restricted essentially to RuO_2 and IrO_2. As reported above, modulation of electrode properties is best achieved by mixing two or more components: improved stability can often be obtained at the expenses of electrocatalytic activity. IrO_2 anodes are known to be much more stable for O_2 evolution in acid environment [18, 19] than RuO_2, while presenting only a slightly lower electrocatalytic activity [20]. RuO_2 is known as the most active oxide for anodic oxygen evolution [21], however it suffers from instability and therefore should be stabilised with another oxide such as IrO_2 [22] or SnO_2 [23]. Thus, IrO_2 has been shown [22] to improve the corrosion resistance of RuO_2 while reducing its activity [24]. However the improved stability of IrO_2 is costly, since this material is about 2-3 time more expensive than RuO_2, so that SnO_2 has received great attention because it is a cheap oxide which can acts partly as stabilizer and partly as catalyst. De Pauli and Trasatti [25-26] have shown that IrO_2–SnO_2 composites proceed, in the oxygen evolution in acidic media, with kinetic parameters close to those of pure IrO_2, for iridium contents down to about 10%. Moreover Tantalum is a wellknown addition to *DSA* electrodes, and Ir–Ta oxides have been suggested as effective electrocatalysts for oxygen evolution in acidic electrolytes due to the high activity and corrosion stability [27], although economical issues limit their use.

Different papers can be also found in the literature on *OER* in alkaline media, aiming to improve the performance of anodes for alkaline water electrolysis. The high overpotential of OER in alkaline water electrolysis leads to low energy efficiency and the efforts have been directed to the study of such low overpotential materials as transition metal oxides to obtain suitable oxygen evolving anodes in alkaline media. Ni and Co oxides exhibit interesting electrocatalytic activities, which make them attractive for O_2 evolution, in particular oxides presenting a spinel crystallographic structure (e.g. Co_3O_4, $NiCo_2O_4$, $CoFe_2O_4$) have received considerable attention due to their low cost, good conductivity, stability in alkaline solution and high electrocatalytic activity for *OER* [28-36].

The low cost of the spinel oxides has motivated intensive research, resulting in development of a strategy to stabilise the spinel also under acid conditions, this goal can be achieved by the formation of mixed rutile/spinel oxides [37-42].

Among “non-active” materials at which evolution of O_2 occurs with very high overpotential, boron doped diamond (*BDD*) has been widely investigated for different electrochemical applications such as electrosynthesis [43-45], incineration of organic pollutants for wastewater treatment [46-51], water disinfection [52-54], preparation of powerful oxidants [55] and electroanalysis [56-58]. In all these electrochemical processes *OER* is the most important side reaction to be considered. *BDD* has been chosen due to its remarkable properties of chemical inertness, very low background current, a large window available between hydrogen and oxygen evolution, and an extreme resistance to chemical and electrochemical attacks [59]. In particular, due to its chemical inertness, this material is considered an ideal "non-active" electrode on which oxidation of organics and oxygen evolution take place through the formation of weakly adsorbed and very reactive hydroxyl radicals.

Among the other electrochemical applications*,* *BDD* anodes have been widely proposed to oxidative treatment of synthetic and real wastewaters containing both inorganic and organic compounds. The interest was initially on oxidation of model substances or, in any case, of substances whose oxidation was already studied with other technologies, the results of which could be assumed as a comparison. Phenol [60, 61] and oxalic acid [62-64] were often considered to model the behaviour of the aromatic and aliphatic fractions of the waste, respectively. Then, the attention was focused also to different substances, such as substituted phenols or more complex molecules as those of dyes [65]. Depending on different factors, such as the nature of the organic substrate, the nature and composition of the supporting electrolyte and the imposed operative conditions, the whole process may be only controlled by one or more steps which can lead to different performances of *BDD* anodes. Granted that *BDD* performed well in all the examined cases, leading in most of the cases to complete mineralization of the pollutant, some doubts still remain on the comprehension of the reaction mechanism, which represents a crucial point when the best operative conditions have to be individuated in order to optimise the process in terms of yield and costs.

Many questions are still open and the comprehension of the electrochemical behaviour of *BDD* is not yet completely achieved. Actually, several factors may heavily influence the electrochemical performance of this material, such as doping level, morphological features (grain boundaries and point defects), non-diamond impurity content and surface group functionalities [66]. Several results have been published and different hypotheses have been proposed, but unfortunately an objective comparison between them is hard, due to the lack of a standard diamond electrode material to compare results against.

1.2 References

[1] H. Wendt, M. Gotz, M. Linardi, Tecnologia de Células a Combustìvel Quìmica Nova 4 (2000) 538

[2] A.C.C. Tseung, S. Jansen, Electrochim. Acta 22 (1977) 31

[3] B.E. Conway, B.V. Tilak, in: D.D. Eley, H. Pines, P.B. Weiss (Eds.), Advances in Catalysis, vol. 38, Academic Press, New York, 1992, p. 78-98

[4] Ch. Comninellis, Electrochim. Acta 39 (1994) 1857

[5] G. Foti, D. Gandini, Ch. Comninellis, Current Topics in Electrochemistry 5 (1997) 71

[6] B. Marselli, J. Garcia-Gomez, P.A. Michaud, M.A. Rodrigo, Ch. Comninellis, J. Electrochem. Soc. 150 (2003) D79

[7] S. Trasatti, in: H. Wendt (Ed.) The Oxygen Evolution Reaction in Electrochemical Hydrogen Technologies, Elsevier, Amsterdam, 1990, p. 1-14

[8] H.B. Beer, J. Electrochem. Soc. 127 (1980) 303

[9] S. Trasatti, Electrochim. Acta 36 (1991) 225

[10] A.C.C. Tseung, S. Jasem, Electrochim. Acta 22 (1977) 31

[11] R. Bertoncello, F. Furlanetto, P. Guerriero, M. Musiani, Electrochim. Acta 44 (1999) 4061

[12] S. Cattarin, P. Guerriero, M. Musiani, Electrochim. Acta 46 (2001) 4229

[13] M. Musiani, F. Furlanetto, P. Guerriero, J. Electroanal. Chem. 440 (1997) 131

[14] Ch. Comninellis, G.P. Vercesi, J. Appl. Electrochem. 21 (1991) 335

[15] B. Marsan, N. Fradette, G. Beaudoin, J. Electrochem. Soc. 139 (7) (1992) 1889

[16] R.N. Singh, A.K. Singh, J.P. Singh, Electrochim. Acta 47 (2002) 3873

[17] G.N. Martelli, R. Ornelas and G. Faita, Electrochim. Acta 39 (1994) 1551

[18] R. KoÈtz, S. Stucki, Electrochim. Acta 31 (1986) 1311

[19] Y. Kamegaya, K. Sasaki, M. Oguri, T. Asaki, H. Hobayashi, T. Mitamura, Electrochim. Acta 40 (1995) 889

[20] S. Trasatti, in: J. Lipkowski, P.N. Ross (Eds.) The Electrochemistry of Novel Materials, VCH Publishers, 1994, p. 207-295

[21] S. Trasatti, Electrochim Acta 29 (1984) 1503

[22] R. Kotz, S. Stucki, Electrochim Acta 31 (1986) 1311

[23] R. Hutchings, K. Muller, S. Stucki, J. Mater. Sci. 19 (1984) 3987

[24] C. Angelinetta, S. Trasatti, Lj.D. Atanasoska, Z.S. Minevski and R.T. Atanasoski, Mater. Chem. Phys. 202 (1989) 231

[25] C.P. De Pauli, S. Trasatti, J. Electroanal. Chem. 538–539 (2002) 145

[26] C.P. De Pauli, S. Trasatti, J. Electroanal. Chem. 396 (1995) 161

[27] Y. Roginskaya, O. Morozova, E. Loubnin, A. Popov, Y. Ulitina, V. Zhurov, et al., J. Chem. Soc.Faraday Trans 89 (1993) 1707

[28] B.E. Conway, in: S. Trasatti (Ed.), Electrodes of Conductive Metallic Oxides: Part B, Elsevier, Amsterdam, 1981, p. 433

[29] E.J.M. O'Sullivan, E.J. Calvo, in: R.G. Compton (Ed.), Comprehensive Chemical Kinetics, vol. 27, Elsevier, Amsterdam, 1987, p. 274

[30] R. Boggio, A. Carugati, S. Trasatti, J. Appl. Electrochem. 17 (1987) 828

[31] E. Conway, T.C. Liu, Ber. Bunseng. Phys. Chem. 91 (1987) 461

[32] L.G. Tejuca, J.L.F. Fierro, J.M. Tascon, Advances in Catalysis, vol. 36, Academic, New York, 1989,

[33] R.N. Singh, M. Hamdani, J.F. Koenig, G. Poillerat, J.L. Gautier, P. Chartier, J. Appl. Electrochem. 20 (1990) 442

[34] S.P. Singh, S. Samuel, S.K. Tiwari, R.N. Singh, Int. J. Hydrog. Energy 21 (1996) 171

[35] L.A. De Faria, M. Prestat, J.F. Koenig, P. Chartier, S.Trasatti, Electrochim. Acta 44 (1998) 1481

[36] R.N. Singh, J.P Pandey, N.K. Singh, B. Lal, P. Chartier, J.F. Koenig, Electrochim. Acta 45 (2000) 1911

[37] Da Silva, L.M.; Boodts, J.F.C.; De Faria, L.A.; Electrochim. Acta 46 (2001) 1369

[38] N. Krstajíc, S. Trasatti, J. Electrochem. Soc. 142 (1995) 2675

[39] L.A. De Faria, J.F.C. Boodts, S. Trasatti, Electrochim. Acta 37 (1992) 2511

[40] L.M. Da Silva, J.F.C. Boodts, L.A. De Faria, Electrochim. Acta 46 (2001) 1369

[41] L.M. Da Silva, J.F.C. Boodts, L.A. De Faria, Electrochim. Acta 45 (2000) 2719

[42] L.M. Da Silva, J.F.C. Boodts, L.A. De Faria, J. Electroanal. Chem. 532 (2002) 141

[43] K. Serrano, P.A. Michaud, C. Comninellis, A. Savall, Electrochim. Acta 48 (2002) 431

[44] F. Beck, W. Kaiser, H. Krohn, Electrochim. Acta 45 (2000) 4691

[45] J.D. Wadhawan, F.J. Del Campo, R.G. Compton, J.S. Foord, F. Marken, S.D. Bull, S.G. Davies, D.J. Walton, S. Ryley, J. Electroanalytical Chem. 507 (2001) 135

[46] M. Panizza, P.A. Michaud, G. Cerisola, C. Comninellis, Electrochemistry Communications 3 (2001) 336

[47] A. Morao, A. Lopes, M.T. Pessoa de Amorim, I.C. Goncalves, Electrochim. Acta 49 (2004) 1587

[48] R. Bellagamba, P.A. Michaud, C. Comninellis, N. Vatistas, Electrochemistry Communications 4 (2002) 171

[49] J. Iniesta, P. A. Michaud, M. Panizza, G. Cerisola, A. Aldaz, Ch. Comninellis, Electrochim. Acta 46 (2001) 3573

[50] M. Panizza, P.A. Michaud, G. Cerisola, Ch. Comninellis, J. Electroanal. Chem. 507 (2001) 206

[51] M.A. Rodrigo, P.A. Michaud, I. Duo, M. Panizza, G. Cerisola, Ch. Comninellis, J. Electrochem. Soc. 148 (2001) D60

[52] T. Furuta, H. Tanaka, Y. Nishiki, L. Pupunat, W. Haenni, P. Rychen, Diamond and Related Materials 13 (2004) 2016

[53] A. M. Polcaro, A.Vacca, M. Mascia, S. Palmas, R. Pompei and S. Laconi, Electrochim. Acta 52 (2007) 2595

[54] S. Palmas, A. M. Polcaro, A. Vacca, M. Mascia, F. Ferrara, J. of Apple. Electrochem. 35 (11) (2007) 1357

[55] P.A. Michaud, E. Mahe, W. Haenni, A. Perret, Ch. Comninellis, Electrochemical and Solid-State Letters 3 (2000) 77

[56] Y. Einaga, R. Sato, H. Olivia, D. Shin, T.A. Ivandini, A. Fujishima, Electrochimica Acta 49 (2004) 3989

[57] T.N. Rao, A. Fujishima, Diamond and Related Materials 9 (2000) 384

[58] K. Boonsong, S. Chuanuwatanakul, N. Wangfuengkanagul, O. Chailapakul, Sensors and Actuators B 108 (2005) 627

[59] Y.V. Pleskov, Russ. Chem. Rev. 68 (1999) 381

[60] J. Iniesta, P.A. Michaud, M. Panizza, G. Cerisola, A. Aldaz, Ch. Comninellis, Electrochim. Acta 46 (23) (2001) 3573

[61] A.M. Polcaro, A. Vacca, S. Palmas, M. Mascia, J. of Apple. Electrochem. 33 (10) (2003) 885

[62] C.A. Martinez-Huitle, S. Ferro, A. De Battisti, Electrochim. Acta 49 (2004) 4027

[63] C.A. Martinez-Huitle, S. Ferro, A. De Battisti, J. Appl. Electrochem. 35 (2005) 1087

[64] T.A. Ivandini, Y. Naono, A. Nakajima, Y. Einaga, Chem. Lett. 34 (2005) 1086

[65] M.A.Q. Alfaro, S. Ferro, C. A. Martinez-Huitle, Y. M. Vong, J. Braz. Chem. Soc. 17 (2006) 227

[66] I. Duo, A. Fujishima, Ch. Comninellis, Electrochem. Commun. 5 (2003) 695

1.3 Thesis Organization

The Thesis deals with the behaviour of different electrode material in the oxygen evolution reaction.

A brief overview of each Chapter is given below:

In the **Chapter 2** the electrochemical processes taking place at electrode surfaces are presented and a distinction between inner and outer-sphere processes is illustrated.

In the **Chapter 3** the fundamentals of the techniques of cyclic voltammetry, steady-state polarisation and electrochemical impedance spectroscopy are presented as powerful methods to investigate on the electrochemical behaviour of electrode materials.

In the **Chapter 4** the behaviour of Co_3O_4 electrodes, obtained by a sol-gel method, is investigated in alkaline solution during oxidative runs at different anodic potentials up to the value of oxygen evolution reaction. In particular, chemical structure, catalyst morphology, reaction mechanism and kinetic parameters for *OER* at this electrode are evaluated.

In the **Chapter 5** the behaviour of SnO_2 and SnO_2-RuO_2 electrodes, mechanically processed for different times, is investigated in acid media during oxidative runs. Cyclic voltammetry and polarization experiments have been carried out together with electrochemical impedance spectroscopy to point out the effects of milling process on the electrode catalytic performances.

In the **Chapter 6** the results on the evolution of electronic structure and electrochemical activity of boron doped diamond samples during oxidative ageing tests are presented. The results from Raman analysis, have been conveniently combined with those from electrochemical investigation in order to explain the evolution of electrochemical activity and structural changes of *BDD* samples as the ageing time is increased.

In the **Chapter 7** the conclusions are illustrated.

1.4 Publications and presentations

The topics presented in this Thesis have been the object of scientific communications presented at national and international congresses, and gave rise to papers which appeared in the international literature.

Publications

S. PALMAS, A.M. POLCARO, **F. FERRARA**, J. RODRIGUEZ RUIZ, F. DELOGU, C. BONATTO-MINELLA, G. MULAS
"Electrochemical performances of mechanically treated SnO_2 powders for OER in acid solution" Journal of Applied Electrochemistry, in press (2007)

S. PALMAS, **F.FERRARA**, A. VACCA, M. MASCIA, A.M. POLCARO
"Behavior of cobalt oxide electrodes during oxidative processes in alkaline medium.", Electrochimica Acta 53 (2) (2007) 400

S. PALMAS, **F.FERRARA**, A. PISU, C. CANNAS
"Oxygen evolution on Ti/Co3O4-coated electrodes in alkaline solution."
Chemical Papers 61(2) (2007) 77

S. PALMAS, A.M. POLCARO, A. VACCA, M. MASCIA, **F. FERRARA**
"Characterization of boron doped diamond during oxidation processes: relationship between electronic structure and electrochemical activity."
Journal of Applied Electrochemistry 37 (2007) 63

A.M. POLCARO, P.C. RICCI, S. PALMAS, **F. FERRARA**, C. ANEDDA
"Characterization of boron doped diamond during oxidation processes: relationship between electrochemical activity and ageing time."
Thin Solid Films 515 (2006) 2073

Presentations

S. PALMAS, **F. FERRARA**, J. RODRIGUEZ RUIZ, F. DELOGU, A.M. POLCARO, C. BONATTO-MINELLA, G. MULAS
"Preparation and Characterisation of high-energy ball-milling SnO_2/BDD powder electrodes." Congresso GEI-ERA 2007, Cagliari, Luglio 2007

F. FERRARA, S. PALMAS, A.M. POLCARO, M. MASCIA, A. VACCA, J. RODRIGUEZ RUIZ
"Spettroscopia di impedenza elettrochimica per la modellazione della cinetica di evoluzione di ossigeno su elettrodi di Ti/Co3O4." Congresso GEI-ERA 2007, Cagliari, Luglio 2007

F. FERRARA
"Study of Oxygen evolution reaction at different electrode materials."
4th European Summer School on Electrochemical Engineering (ESSEE4), Palić, Serbia, Settembre 2006. ISBN 86-7132-028-6

S. PALMAS, **F. FERRARA**, A.VACCA, M. MASCIA, A.M. POLCARO
"Surface, kinetics and electrocatalytic properties of Ti/Co3O4 electrodes for OER in alkaline medium ." 5th International Conference on Electrocatalysis (ECS'06), Kotor, Montenegro, Settembre 2006

S. PALMAS, A.M. POLCARO, **F. FERRARA**, A.VACCA, M. MASCIA
"Catalytic activity and stability of boron doped diamond electrodes in oxidative processes." XX Congresso Nazionale della Società Chimica Italiana (SCI 2006), Firenze, Settembre 2006

F.FERRARA, S. PALMAS, A. PISU, C. CANNAS
"Oxygen evolution on Ti/Co_3O_4-coated electrodes in alkaline solution."
33th International Conference of Slovak Society of Chemical Engineering, Tatranskè Matliare, Repubblica Slovacca, Maggio 2006. ISBN 80-227-2409-2

F. FERRARA, S. PALMAS, A.M. POLCARO
"Performance of Co_3O_4 electrodes and their electrocatalytic activity towards oxygen evolution." 10th Mediterranean Congress of Chemical Engineering, Barcellona, Novembre 2005.

S. PALMAS, **F. FERRARA**, A. VACCA , M. MASCIA, A.M. POLCARO
"Studio del comportamento di elettrodi di diamante drogato al boro: valutazione della attività catalitica di campioni a diverso livello di drogaggio." Giornate Italiane dell' Elettrochimica (GEI 2005), Spoleto, Settembre2005.

C. CANNAS, A. MUSINU, A. PISU, D. PEDDIS, G. PICCALUGA, G. PINNA, **F. FERRARA**, S. PALMAS
"Ossidi a spinello nanostrutturati per applicazioni elettrocatalitiche ottenuti mediante un metodo sol-gel di autocombustione" Congresso Elettrochimica per il Recupero Ambientale (ERA 2005), Cagliari, Luglio 2005.

S. PALMAS, A.M. POLCARO, A. VACCA , M. MASCIA, **F. FERRARA**
"Caratteristiche superficiali ed attività catalitica di elettrodi di BDD"
Congresso Elettrochimica per il Recupero Ambientale (ERA 2005), Cagliari, Luglio 2005.

In addition to the work presented in this Thesis the author has also participated, during the course of study, in other research projects :

Publications

A. M. POLCARO, A. VACCA, M. MASCIA, **F. FERRARA**
"Product and by-product formation in electrolysis of diluted chloride solutions", Journal of Applied Electrochemistry, under revision (2007)

S. PALMAS, A. M. POLCARO, A. VACCA, M. MASCIA, **F. FERRARA**
"Influence of the operating conditions on the electrochemical disinfection process of natural waters at BDD electrodes." Journal of Applied Electrochemistry 35 (11) (2007) 1357

M. MASCIA, **F. FERRARA**, A. VACCA, G. TOLA, M. ERRICO
"Design of heat integrated distillation systems for a light ends separation plant."
Applied Thermal Engineering 27 (2007) 1205

Presentations

M. MASCIA, A.VACCA, S. PALMAS, , A.M. POLCARO, **F. FERRARA**
"Modelling of bulk and surface reactions during electrochemical oxidation of organic compounds at BDD anodes." European Congress of Chemical Engineering (ECCE-6), Copenhagen, Settembre 2007

M. MASCIA, A.VACCA, S.PALMAS, **F. FERRARA**, A. M. POLCARO
"Mathematical model of bulk and surface reactions during electrochemical oxidations at BDD anodes." Congresso GEI-ERA 2007, Cagliari, Luglio 2007

A.M. POLCARO, A.VACCA, M. MASCIA, S. PALMAS, **F. FERRARA**
"Produzione anodica di agenti disinfettanti per la depurazione di acque naturali."
XX Congresso Nazionale della Società Chimica Italiana (SCI 2006), Firenze, Settembre 2006

M. MASCIA, A.VACCA, S. PALMAS, A.M. POLCARO, **F. FERRARA**
"Mathematical model of bulk and surface reactions during electrochemical oxidations at BDD anodes." XX Congresso Nazionale della Società Chimica Italiana (SCI 2006), Firenze, Settembre 2006

A.VACCA, S. PALMAS, M. MASCIA, **F. FERRARA**, A.M. POLCARO
"Active chlorine formation in the electrochemical treatment of natural waters for disinfection." 57th International Conference of International Society of Electrochemistry (ISE 2006), Edimburgo, Agosto 2006

M. MASCIA, A.VACCA, S. PALMAS, **F. FERRARA**, A.M. POLCARO
"Mathematical model of bulk and surface reactions during electrochemical oxidation at BDD anodes." 57th International Conference of International Society of Electrochemistry (ISE 2006), Edimburgo, Agosto 2006

M. MASCIA, A.VACCA, **F. FERRARA**, A.M. POLCARO
"Effect of surface charge on the transport of cadmium in clays under electrical field." 10th Mediterranean Congress of Chemical Engineering, Barcellona, Novembre 2005

M. MASCIA, S. PALMAS, **F. FERRARA,** A.M. POLCARO
"Trasporto di ioni cadmio in argille sotto campo elettrico: effetto della carica superficiale." Congresso Elettrochimica per il Recupero Ambientale (ERA 2005), Cagliari, Luglio 2005

M.MASCIA, **F.FERRARA**, A.VACCA, G.TOLA
"Design of heat integrated distillation systems for a light ends plant."
Chemical Engineering Transactions, vol.7, pp. 151-156 (2005)

Chapter 2

General aspects of electrochemical processes

2.1 Introduction

Electrochemical reactions are heterogeneous chemical reactions which occur via the transfer of charge across an interface generally between an electronic conductor (electrode) and an ionic conductor (electrolyte). Through the electrode, the charge is usually transported by electrons while, in the electrolyte, the charge transport is provided by the movement of ions.

The minimum components required for an electrochemical cell are an anode, a cathode, the ionic contact between the electrodes (electrolyte) and the electronic contact between them (external electrical circuit).

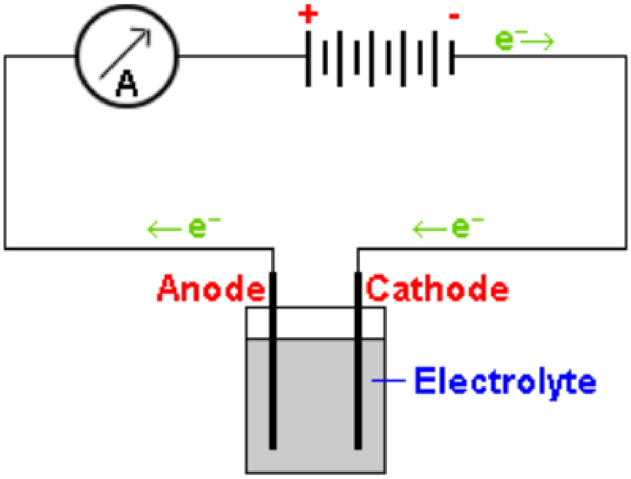

Figure 2.1. *Schematic diagram of an electrochemical cell*

The reaction taking place in an electrochemical cell is the result of two half-reactions which separately describe the charge transfer at the two electrodes. The reaction at the electrode of interest (working electrode) can only be studied by using a second electrode (counter electrode). The potential of the working electrode is measured with respect to a reference electrode. Since the potential of the reference electrode is fixed, any change in the cell is related to the phenomena at the working electrode. The reference electrode is usually placed inside a Luggin capillary, the tip of which is positioned very close to the working electrode surface, to minimize uncompensated ohmic drops. The working electrode should be much smaller than the counter electrode so that no serious polarization of the latter can occur, and therefore the characteristics of the counter electrode reaction do not contribute to the response of the cell.

Two types of processes occur at electrodes: one kind involves electron transfer across the electrode/electrolyte interface (faradaic processes). When the electrode/electrolyte interface changes because of adsorption or desorption phenomena, nonfaradaic processes are said to be involved in the electrical double layer. Both faradaic and nonfaradaic processes take place at an electrode during electrochemical reactions. Although the faradaic processes are of primary interest when studying an electrochemical reaction, the nonfaradaic processes must be considered by studying the nature of the electrode/electrolyte interface.

2.2 The electrical double layer

At any interface between two phases, and particularly between an electrode and an electrolyte solution, there exists a segregation of positive and negative charge in a direction normal to the phase boundary. These charges may be associated in the form of dipolar molecules or polarized atoms, or they may be free as holes, electrons or ions. The charge segregation may occur through the preferential adsorption of either positive or negative ions at the interface, through the transfer of charge across the interface, or through the deformation of polarisable molecules by the asymmetrical force field at the interface. The theory of the electrical double layer is concerned with the charge distribution and electrical potentials that arise as a consequence of this charge separation [1].

The study of the electrical double layer is intimately concerned with the concept of the ideally polarizable electrode, which may be defined as an electrode at which no charge transfer can occur across the electrode/solution interface, even if an external potential difference is imposed. Since, at ideally polarizable electrode, charge does not cross the interface during potential changes, the interface behaves like a capacitor. For a given applied potential, charge is stored in equal measure on the electrode and in the solution. In the case of a metallic electrode, the excess or deficiency of electrons is limited to a very thin surface layer, while the charge in solution is distributed in the proximity of the electrode surface. This charge distribution at the interface is called electrical double layer with which a double-layer capacitance (C_{dl}) is associated.

The double-layer region can be described by a model which assumes a solution side distribution of charge over several layers. The region next to the electrode is made up of solvent molecules and sometimes, specifically adsorbed species. This region is called Helmholtz layer and the plane passing through the electrical centres of these specifically adsorbed ions is called the inner Helmholtz plane.

Solvated ions present in the solution can approach the electrode surface only to a distance from the inner Helmholtz layer that corresponds to the diameter of the solvent molecules. The electrical centres of the nearest solvated ions form the outer Helmholtz plane. These ions, which interact with the electrode through long-range electrostatic forces, are called nonspecifically adsorbed species. Because of the electrostatic nature of these interactions, ions are distributed in a region called the diffuse layer which extends from the outer Helmholtz plane to the bulk of the solution. The thickness of the diffuse layer depends on the total ionic concentration in the solution. Sometimes the double layer can be neglected while studying electrode reaction kinetics. Nevertheless, the study of the electrical double layer is an important area of electrochemistry because the charge distribution in a given system can affect the electron transfer and the course of the electrochemical reaction.

2.3 Faradaic processes

A general electrode reaction such as:

$O + ne^- \leftrightarrow R$ (2.1)

can be written as a sequence of basic steps occurring in the electrochemical cell:

1. mass transfer from the bulk to the electrode surface and vice versa
2. electron transfer at the electrode surface
3. homogeneous or heterogeneous chemical reactions
4. surface phenomena such as adsorption, crystallisation, etc.

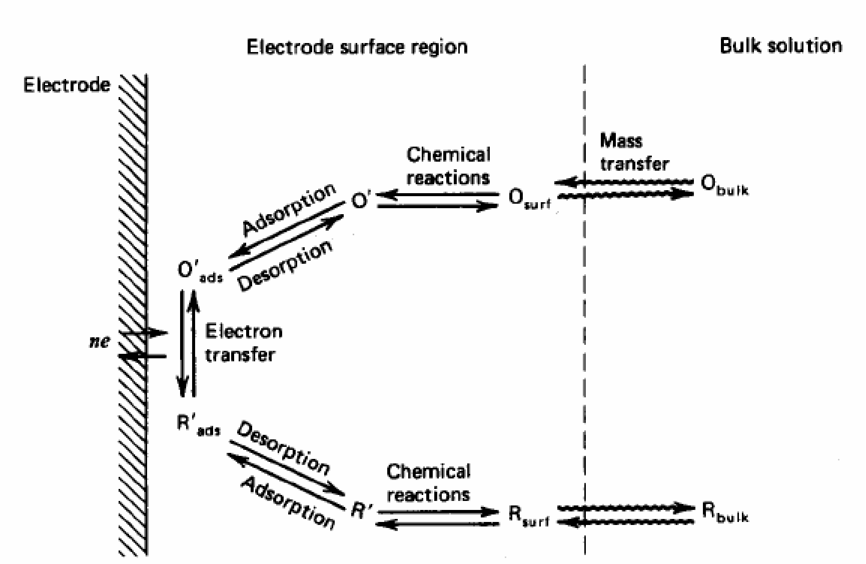

Figure 2.2. *Pathway of a general electrode reaction*

The simplest reaction only involves mass transfer and electron transfer steps, however, chemical reactions and adsorption/desorption processes are taking place in some reactions.

The electrode's response to current flow corresponds to an overpotential that is the sum of different terms associated with the reaction steps occurring with a finite rate in the electrochemical cell.

Accordingly, a reaction can be represented by a series of resistances (or impedances): a fast reaction step is represented by a small resistance, while a slow step is described by a high one. Except for very low current or potential perturbations, these resistances are functions of the applied potential.

The kinetics of a system is strongly influenced by the applied potential. This is true for all faradaic processes. Faradaic processes involve electron transfer occurring across the electrode/electrolyte interface and they lead to reduction or oxidation of species present at the interface. Electron transfer may occur via overlapping of orbitals (in the case of adsorption), via bridging ligands or via electron tunneling; in any case, a molecule undergoing the electron transfer process must be in near proximity of the electrode surface. Species present in bulk solution may be reduced or oxidized only if they are brought to the electrode surface via a mass transport process.

The kinetics of a reaction is also influenced by the nature and structure of the reacting species, the solvent, the electrode material and adsorbed layers on the electrode. Based on the nature of the interactions between reactants and electrode surface, electrochemical faradaic processes can be classified [2] as outer-sphere, inner-sphere, mediated electrode and mediated solution reactions. The attention is here focused on the inner-sphere and the outer-sphere electron transfer reactions [3].

The term outer-sphere is used to describe a reaction, in which the activated complex maintains the coordination sphere originally present in the reactant species. With the term inner-sphere, a reaction is described in which the reactants share a ligand in the activated complex. In other words, an outer-sphere reaction occurs with weak interaction between the electrode and the reactant, which maintains a distance of at least one solvent layer from the electrode surface. Among the outer-sphere systems, $Fe(CN)_6^{3-}/Fe(CN)_6^{4-}$ and $IrCl_6^{2-}/IrCl_6^{3-}$ reactions are the most frequently used.

In the case of an inner-sphere reaction, both the reactant and the product species as well as the activated complex are involved in very strong interactions with the electrode surface (specific adsorption). Obviously, the kinetics of outer-sphere reactions is less dependent on the electrode material than that of inner-sphere electron transfer reactions. Nevertheless, the electrode material could influence the kinetics even in the case of outer-sphere charge transfer, by affecting the electrical double layer and the Helmholtz layer structure. A distribution of electronic states on the electrode surface can influence as well the electron transfer kinetics in outer-sphere reactions. Anyway, outer-sphere reactions can be treated in a more general way than inner-sphere reactions, and the theory is much more developed.

2.3.1 The Butler-Volmer equation [1]

As reported above, the potential of an electrode strongly affects the kinetics of all faradaic processes occurring on its surface. So, the rate of the electron transfer reaction at the electrode surface can be varied by changing the applied voltage. The phenomenological model of Butler-Volmer is able to relate the reaction rate (current density) with the applied electrode potential.

A one-electron process can be considered as the simplest electrode process:

$$O + e^- \underset{k_b}{\overset{k_f}{\longleftrightarrow}} R \tag{2.2}$$

where k_f and k_b represent the heterogeneous rate constants of the reduction and oxidation reaction, respectively. When the rates are equal, the system is at equilibrium.

For positive potential values, the energy of the reactant electron is lower, the energy curve drops with respect to the energy of O. The reduction barrier rises and the net effect is the conversion of O to R.

In this condition, the component I_a, of the total current is defined as:

$$I_a = FAk_b C_R(0,t) \tag{2.3}$$

where F is the Faraday constant, A is the electrode surface area and $C_R(0,t)$ is the concentration of the reduced form at the electrode surface at time t. For potentials more negative than the equilibrium value, the situation is inverted, and a net cathodic flow of current is obtained.

The component I_c, of the total current is defined as:

$$I_c = -FAk_f C_o(0,t) \tag{2.4}$$

where $C_o(0,t)$ is the concentration of the oxidized form at the electrode surface at time t.

At any potential the measured current is given by:

$$I = I_a + I_c \tag{2.5}$$

where I_c is negative.

If E^0 is defined as the potential where reduction and oxidation rate constants have the same value, which corresponds to the standard rate constant, k^0 ($k_f = k_b = k^0$), the reaction rate constants can be expressed in terms of k^0:

$$k_f = k^0 \exp\left[-\alpha_c \frac{F}{RT}\left(E - E^0\right)\right] \tag{2.6}$$

$$k_b = k^0 \exp\left[\alpha_a \frac{F}{RT}\left(E - E^0\right)\right] \tag{2.7}$$

where α_c and α_a are constants (between 0 and 1 and generally approximately 0.5) known as the transfer coefficients for the anodic and cathodic reactions respectively.

So, the influence of the potential on the rate of an electrode reaction can be determined quantitatively by the following kinetic equation:

$$I = FAk^0\left\{C_R(0,t)\exp\left[-\alpha_a \frac{F}{RT}\left(E - E^0\right)\right] - C_o(0,t)\exp\left[-\alpha_c \frac{F}{RT}\left(E - E^0\right)\right]\right\} \tag{2.8}$$

A system with a large k^0 will reach equilibrium on a short time scale, while small k^0 are typical of very slow reactions. The largest values of k^0 have been measured in the range of 1 to 10 cm s^{-1} and are associated with outer-sphere transfer processes. Even if k^0 of a reaction is quite small, the k_f and k_b value can be made quite large by using a sufficiently high potential relative to the E^0 value.

At equilibrium ($E = E_{eq}$) the net current is zero, the bulk concentrations are found also at the surface: $C^* = C(0,t)$, thus from the Equation (2.8) it is possible to obtain the Nernst equation:

$$E_{eq} = E^0 + \frac{RT}{F}\ln\frac{C_0^*}{C_R^*} \tag{2.9}$$

At equilibrium, the oxidation and the reduction reactions take place with the same rate. In this condition, the anodic current (equal in absolute value to the cathodic one), and can be expressed in terms of exchange current density i_0 as:

$$i_0 = Fk^0 C \tag{2.10}$$

where $C_0^* = C_R^* = C$

By dividing Equation (2.8) by Equation (2.10) and defining the overpotential as the deviation of the potential from the equilibrium value, $\eta = E - E_{eq}$, the following equation can be obtained:

$$i = i_0 \left[\frac{C_R(0,t)}{C_R^*} \exp^{\alpha_a \frac{F}{RT}\eta} - \frac{C_0(0,t)}{C_o^*} \exp^{-\alpha_c \frac{F}{RT}\eta} \right] \tag{2.11}$$

If the solution is well stirred or the current is so low that the surface concentration does not differ from the bulk value, the last equation, becomes:

$$i = i_0 \left[\exp^{\alpha_a \frac{F}{RT}\eta} - \exp^{-\alpha_c \frac{F}{RT}\eta} \right] \tag{2.12}$$

which is known as the Butler-Volmer equation.

This must be regarded as the foundamental equation of electrode kinetics, and it shows the way in which current density varies with exchange current density, overpotential and the transfer coefficients. So, without concentration and therefore mass transport effects to complicate the electrolysis, it is possible to establish the effects of voltage on the current flowing. In this situation the overpotential reflects the activation energy required to force the current to flow.

Depending on the overpotential value, two cases can be distinguished:

a) High overpotentials

For large values of the overvoltage, the equation can be simplified as:

$$\log i = \log i_0 + \frac{\alpha_a F}{2.3RT}\eta \qquad \text{(high positive overpotentials)} \tag{2.13}$$

$$\log(-i) = \log i_0 - \frac{\alpha_c F}{2.3RT}\eta \qquad \text{(high negative overpotentials)} \tag{2.14}$$

The plot of *log i vs* η, known as Tafel plot, is a useful device for evaluating the kinetic parameters. Tafel plots are represented by two branches, one with a positive (anodic) and one with a negative (cathodic) slope. Both linear segments extrapolate to a common intercept which corresponds to *log* i_0. The plot deviates from linear behaviour as η approaches zero, because the back reaction can no longer be neglected. From this kind of representation, values of exchange current density and transfer coefficient are easily accessible.

When i_o is 'large' then a small change in η results in a large current change. Essentially there is little or no activation barrier to either of the electrolysis reactions. For this case the electrode reaction is said to be reversible since both k_f and k_b are large. At the other extreme when i_o is very 'small' then a large value of η is needed to alter the current. This reflects the fact that there is now a high barrier to activation and so the rates of the reduction and oxidation processes become slow. Electrode reactions of this type are termed irreversible. In this condition, good Tafel relationships can be obtained. Intermediate behavior is generally referred to as quasi-reversible. Not surprisingly the different rates of electrode kinetics give rise to substantially different behavior in voltammetric and impedance analysis.

b) Low overpotentials

For small values of the overpotential, the two exponential term of Equation (2.12) may expanded as series, and ignoring quadratic and higher order terms leads to the simple equation:

$$i = i_0 \frac{F}{RT}\eta \tag{2.15}$$

which shows that the net current is linearly related to the overpotential within a narrow potential range near E_{eq}. The ratio η /i has the units of a resistance, and is often called the charge transfer resistance, R_{ct}.

2.4 References

[1] Southampton Electrochemistry Group, Instrumental methods in Electrochemistry, J. Wiley and Sons, Inc., New York, 1985

[2] F. Beck and H. Schulz, Electrochim. Acta 29 (1984) 1569

[3] A. J. Bard and L. R. Faulkner, Electrochemical methods-Foundamentals and applications, J. Wiley and Sons, Inc., New York, 2001

Chapter 3

Electrochemical techniques

3.1 Introduction

In order to investigate the values of the various parameters controlling the electrochemical reaction it is often necessary to perturb the system in some way. There are a wide range of electrochemical techniques which have been developed to study electrochemical reactions, but by taking a rather broader view of the nature of an electrochemical experiment we can classify all possible experiments into one of three general classes:

Non-Perturbed Measurements - This group incorporates all measurements that are made without any external perturbation of the system. It includes potential-time and current-time monitoring and electrochemical noise measurements. These techniques are very attractive because any information they are able to provide relates to the actual system being studied, with little possibility of artefacts due to the measurement technique.

Linear Perturbed Measurements - This group includes all techniques that are designed and analyzed on the assumption that the electrochemical system can be treated as a combination of linear circuit elements (e.g. resistors, capacitors etc.). This is almost invariably an approximation to reality, but by restricting ourselves to small changes of potential (of the order of 10 mV or less), we generally obtain a reasonable approximation to linear behaviour. It can be shown that all linear techniques sample the same basic characteristics of the electrochemical system, although some methods provide a more thorough sampling than others. Examples of linear techniques include linear polarization resistance measurement, electrochemical impedance spectroscopy and some small amplitude transient techniques.

Non-Linear Perturbed Measurements - These techniques differ from the linear techniques in that the electrochemical system is not assumed to respond in a linear fashion. Usually this implies that larger amplitude perturbations are used, although this is not necessarily the case. Typical examples of non-linear techniques include the measurement of polarization curves, larger amplitude transient methods and harmonic analysis techniques.

The attention is here focused to the methods of cyclic voltammetry, steady-state polarisation and impedance spectroscopy, as simple and powerful techniques for studying the kinetic parameters in electrochemical systems.

3.2 Cyclic voltammetry

Cyclic voltammetry is often the first experiment performed in an electrochemical study. The powerful of cyclic voltammetry results from its ability to rapidly provide considerable information on the thermodynamics of redox processes and the kinetics of heterogeneous electron-transfer reactions, and on coupled chemical reactions or adsorption processes.

In a cyclic voltammetry experiment, during the potential sweep, the potentiostat measures the current resulting from the applied potential (Figure 3.1).

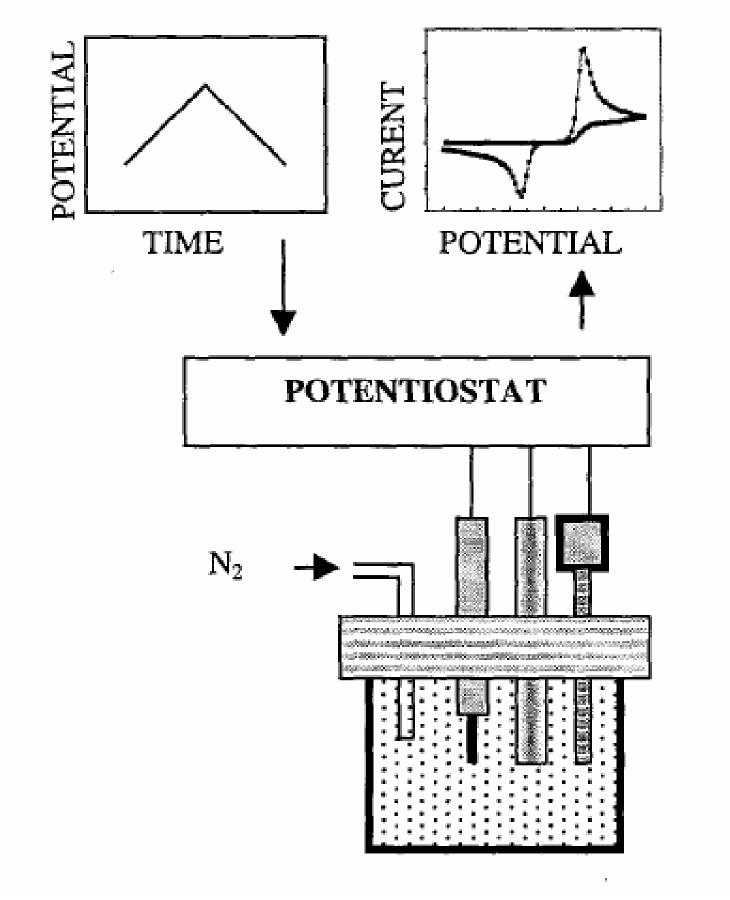

Figure 3.1. *Cyclic voltammetry measuring system*

The potential sweep rate *(ν)* used in conventional experiments ranges from a few mV s^{-1} up to a few hundred V s^{-1}. The resulting plot of current *vs* potential is termed a cyclic voltammogram. The current response over a range of potentials is measured, starting at an initial value and varying the potential in a linear manner up to a pre-defined limiting value. At this potential (switching potential), the direction of the potential scan is reversed, and the same potential window is scanned in the opposite direction (Figure 3.2). It follows that the potential limits and the potential sweep rate are the basic adjustable parameters.

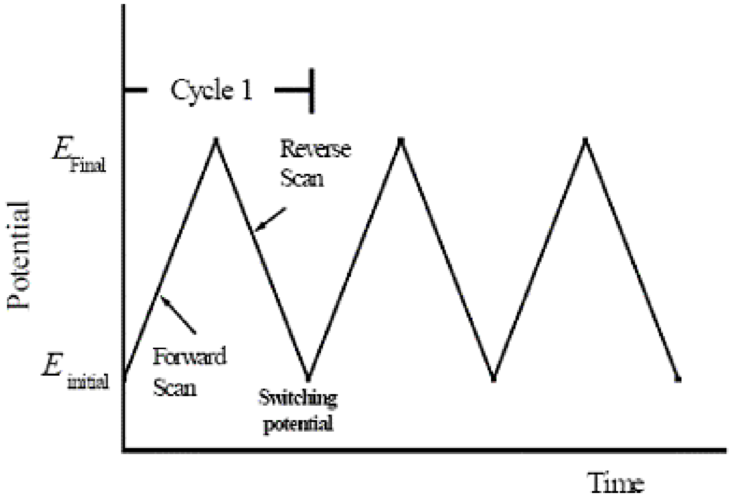

Figure 3.2. *Potential-time signal in cyclic voltammetry experiments*

The cyclic voltammogram is a complicated, time-dependent function of a large number of physical and chemical parameters. Commonly, in a cyclic voltammogram, there are several peaks and by observing how these appear and disappear as the potential limits and sweep rate are varied, and also by noting the differences between the first and subsequent cycles, it is possible to determine how the processes represented by the peaks are related. At the same time, from the sweep rate dependence of the peak amplitudes the role of adsorption, diffusion and coupled homogeneous chemical reactions may be identified. Also the difference between the first and subsequent cyclic voltammograms frequently provides useful mechanistic information.

The cyclic voltammogram is characterized by several important parameters. In particular, four of these observable parameters, the two peak currents (I_p) and two peak potentials (E_p), provide the basis for the diagnostics in order to analyze the cyclic voltammetric response. Also the half-wave potential ($E_{1/2}$ when $I=I_{1/2}$) and a potential at the half of the peak ($E_{p/2}$ when $I=I_{p/2}$) are useful parameters. The way of reading the current density of a peak is shown in Figure 3.

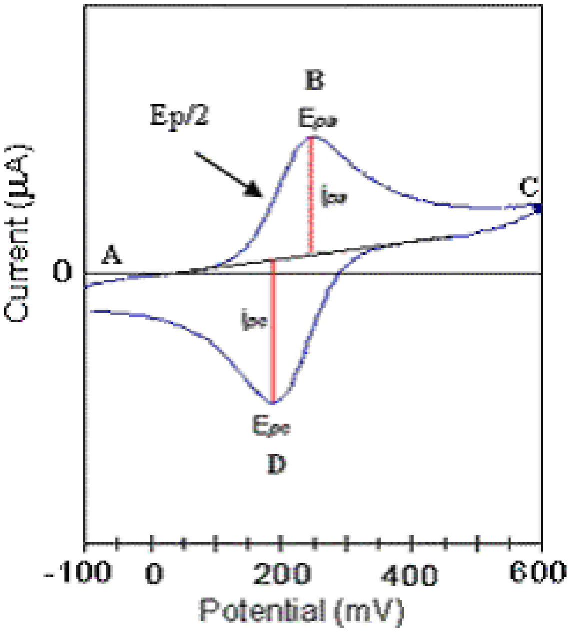

Figure 3.3 . *Typical cyclic voltammogram showing the important peak parameters*

The shape of a cyclic voltammogram is representative of behaviour of the studied system. As reported in the previous section, generally two limiting cases of studied systems do exist: reversible electrode process and irreversible electrode process, which will be illustrated in the following paragraphs.

3.2.1 Reversible electrode systems

For a reversible electrode reaction, the ratio between the surface concentration of electroactive species is given by the Nernst equation:

$$E = E^0 + \frac{RT}{F}\ln\frac{C_{ot}}{C_{Rt}} \tag{3.1}$$

The dependence of electrode potential on time could be expressed as:

$$E(t) = E_1 - \nu \cdot t \qquad \text{(for } 0 < t < \lambda) \tag{3.2}$$

$$E(t) = E_1 - 2\nu \cdot \lambda + \nu \cdot t \qquad \text{(for } t > \lambda) \tag{3.3}$$

where E_1 is the initial potential, ν is the potential sweep rate and λ the time at which the sweep is reversed.

By substitution the Equation (3.2) in the Equation (3.1) a dependence of ratio of surface concentration of oxidized and reduced species on time and on potential scan rate could be expressed as:

$$\frac{C_{ot}}{C_{Rt}} = \exp\left[\frac{nF}{RT}\left(E_1 - \nu \cdot t - E^0\right)\right] \tag{3.4}$$

These equations represent the base for a mathematical description of a general shape of cyclic voltammogram. The solution is quite difficult because of the time dependent potential term, but it can be shown that for planar diffusion the value of current in the peak maximum could be calculated as [1, 2] :

$$I_P = 0.4463nF\left(\frac{nF}{RT}\right)^{0.5} AC_0^* D^{0.5}\nu^{0.5} \tag{3.5}$$

this expression is called the Randles-Sevcik equation and at 25 °C for A in cm^2, D in $\text{cm}^2\ \text{s}^{-1}$, C_0* in mol cm^{-3}, ν in V s^{-1}, and I_p in A, can be written as:

$$I_P = 2.69 \times 10^5 AC_0^* D^{0.5}\nu^{0.5} \qquad \text{(for } n = 1) \tag{3.6}$$

Thus we see that the peak current density is proportional to the concentration of electroactive species *(C_0*)* and to the square roots of the sweep rate *(ν)* and the diffusion coefficient *(D)*.

Figure 3.3 shows a typical cyclic voltammogram obtained for a reversible system.

The peak potential, E_p, can be expressed as:

$$E_p = E_{1/2} - 1.109\frac{RT}{nF} \tag{3.7}$$

Because the peak sometimes is broad so that the peak potential may be difficult to be determined, it will be convenient to report the half-peak potential $E_{p/2}$, which corresponds to the potential at a current equal to $I_{p/2}$. $E_{1/2}$ is located midway between E_p and $E_{p/2}$, so that a convenient diagnostic for a Nernstian wave is given by:

$$| E_p - E_{p/2} | = 2.2\frac{RT}{nF} \tag{3.8}$$

It could be noted the peak potential and other potential characteristics are sweep-rate independent and the peak current density is directly proportional to $\nu^{1/2}$, when the reaction is reversible. The latter property indicates a diffusion-controlled process. On these basis, a test of the reversibility of the system is to check whether a plot of I_p as function of $\nu^{1/2}$ is both linear and passes through the origin (Figure 3.4).

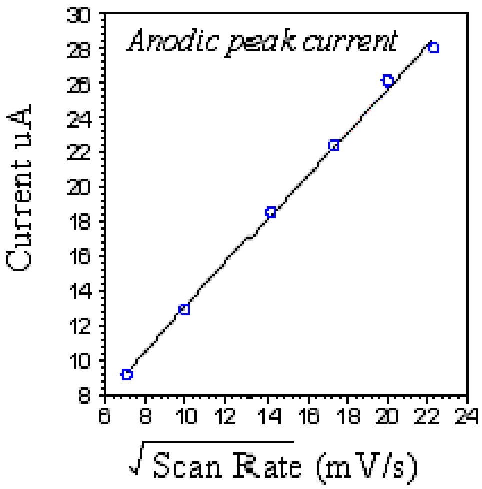

Figure 3.4. *Test of the reversibility of the system*

If this is found to be true then there are further diagnostic tests to be applied, all of which should be satisfied by a reversible system. The following experimental parameter values can be useful to characterize the cyclic voltammogram of a reversible process:

1. the peak potential separation $\Delta E_p =(E_{pc} - E_{pa}) = 59/n$ mV at all scan rates at 25 ^{o}C.
2. the peak current ratio = I_{pa}/I_{pc} = 1 at all scan rates
3. E_{p} is independent of ν
4. the peak current function $I_p/\nu^{1/2}$ is independent of ν (see equation for peak current).

It must be emphasised that a reversible cyclic voltammogram can only be observed if both electroactive species are stable and the kinetics of the electron transfer process are fast, so that all potentials and the potential scan rates the electron transfer process on the surface is in equilibrium, so that the surface concentrations follow the Nernst equation.

3.2.2.Irreversible electrode systems

In the case of the reversible system discussed above, the electron transfer rates at all potentials are significantly greater than the rate of mass transport, and therefore Nernstian equilibrium is always maintained at the electrode surface. The boundary condition on the surface of an electrode in case of fully irreversible electrode reaction is given by kinetics of electrode reaction instead of Nernst equilibrium:

$$\frac{I}{nFA} = D_o\left[\frac{\mathrm{dC}_{\mathrm{o(x,t)}}}{\mathrm{dx}}\right]_{\mathrm{x=0}} = k_{(t)}\mathrm{C}_{\mathrm{o(0,t)}} \tag{3.9}$$

The following equation gives then the value of its kinetic constant:

$$k_{(t)} = \mathrm{k}^0\exp\left\{(-\alpha)\frac{nF}{RT}\left[E_t - E^0\right]\right\} \tag{3.10}$$

By soluting these equations the peak maximum could be calculated as:

$$I_P = 0.4958nF\left(\frac{\alpha nF}{RT}\right)^{0.5} AC_0^*D_0^{\ 0.5}\nu^{0.5} \tag{3.11}$$

The potential of a current peak and the distance between this potential and the half-peak potential are given by:

$$E_P = E^0 - \frac{RT}{\alpha nF}\left[0.780 + \ln\left(\frac{\mathrm{D}_0^{0.5}}{\mathrm{k}^0}\right) + \ln\left(\frac{\alpha nF\nu}{RT}\right)^{0.5}\right] \tag{3.12}$$

$$\left|E_p - E_{p/2}\right| = \frac{1.857RT}{\alpha nF} \tag{3.13}$$

Probably the most marked feature of a cyclic voltammogram of a totally irreversible system is the total absence of a reverse peak. However, such a feature on its own does not necessarily imply an irreversible electron transfer process, but could be due to a fast following chemical reaction. Other tests must therefore be made. On the basis of the previous equations it could be assumed the peak current density is directly proportional to the square root of potential sweep rate also in the case of irreversible electrode reaction. The fact the peak potential is a function of potential sweep rate, specifically it is directly proportional to its square root, represents, however, a significant difference from reversible process.

3.2.3 Quasi-reversible systems

Systems being in the range limited by these two extreme cases could be often met in the praxis. Slow electron transfer kinetics is a common cause of irreversible behaviour. Reversibility requires that the electron transfer kinetics is fast enough to maintain the surface concentrations of electroactive species at the values required by the Nernst equation. Hence, reversibility depends on the relative values of the standard heterogeneous electron transfer rate constant (k^0) and the scan rate ν. If the ratio of k^0/ν is sufficiently small that Nernstian concentrations cannot be maintained, then the process is said to be quasi-reversible. A quasi-reversible process is characterized by $\Delta E_p > 59/n$ mV, with the value increasing with increasing ν.

For the one-step, one-electron case the peak current is given by:

$$I_P = I_p(\mathrm{rev})\mathrm{K}(\Lambda, \alpha) \tag{3.14}$$

where I_p(rev) is the reversible peak value (Equation 3.5). The shape of the peak and the various peak parameters are a function of α and of a parameter Λ defined as:

$$\Lambda = \frac{k^0}{\left(D_o^{1-\alpha} D_R^{\alpha} \frac{RT}{F} \nu \right)^{0.5}} \tag{3.15}$$

Since reversibility depends on the value of k^0/ν, it may be possible to change a process from quasi-reversible to reversible by decreasing ν. In addition, ΔE_p depends on the value of k^0/ν, and k^0 can therefore be calculated from the variation of ΔE_p with ν. Unfortunately, increases in ΔE_p with increasing ν can also be due to uncompensated solution resistance.

Also chemical reactions of electroactive species can cause irreversible behaviour. The effect of a chemical reaction depends on the value of the ratio between the rate of the chemical reaction and the scan rate. If this value is large, then the chemical reaction has a significant effect, whereas any effect is much less if this ratio is small. Therefore, it may be possible to eliminate the effect of the chemical reaction by increasing ν.

Although cyclic voltammetry is very widely used for the initial characterization of an electrochemical system and for qualitative investigation of chemical reactions that accompany electron transfer, there are a number of disadvantages inherent in this technique:

1. The effects of slow heterogeneous electron transfer and chemical reactions cannot be separated. If both of these effects are present, then the rate constants for these processes can only be calculated using simulation methods.
2. There is a background charging current throughout the experiment of magnitude νC_{dl} (where C_{dl} is the capacitance of the interface at the working electrode). This restricts the detection limit to about 10^{-5} M. In addition, the ratio of the peak faradaic current to the charging current decreases with increasing ν (since I_p is proportional to $\nu^{1/2}$), and this places an upper limit on the value of ν that can be used.

In spite of these limitations, cyclic voltammetry is very well suited for a wide range of applications. Indeed, in some areas of research, cyclic voltammetry is one of the standard techniques used for characterization. Moreover, cyclic voltammetries can give useful information about electrochemical porosity and morphology factor.

3.2.4 Electrochemical porosity and morphology factor

The broadness of the peak in the cyclic voltammetry, could be connected with the heterogeneity of the size distribution of the active surface sites [3] or with the high degree of porosity or/and roughness, which affects the energy of the active sites thus leading to broadening of the peak [4]. The position of the peak is indicative of the site's chemical nature, while the area under the peak is proportional to the numbers of sites oxidized or reduced [3].

Integration of the voltammetric curve provides the surface charge transferred during potential scan. Then, this charge is proportional the surface concentration of the active sites participating in the surface redox reaction [5]. The voltammetric charge includes the charge under the pairs of peaks, this charge might depend on the nature of the surface sites.

The resolution of broad, not well defined peaks is however very difficult. In this case the voltammetric charge over the whole potential range (q^*) can be taken as relative measure of the electrochemically active surface area. The values of q^* obtained cannot be easily converted into an absolute value since the precise nature of surface redox transitions is unknown, but q^* has proved to be very useful when different electrodes or different preparation procedures are being compared [3,6,7]. To estimate the actual surface area of the oxide films taking place in the surface redox reactions, the surface charge q^* can be calculated by integrating the voltammetric curves as suggested by Trasatti and coworkers [6,7]. The common observation with oxide electrodes is that q^* decreases as the potential scan rate ν increases. It has been shown, that q^* can be extrapolated to $v = 0$, thus providing the total surface charge q_t^*, as well as to $v = \infty$, thus giving the outer surface charge q_o^* [7]. The difference $q_t^* - q_o^* = q_i^*$ provides the inner surface charge, i.e. the charge associated with the less accessible surface regions (pores, cracks, grain boundaries, etc.), where protons diffuse with difficulty [8].

According to Trasatti and coworkers [6,7], if the total charge q^*_t is related to the whole active surface, the ratio q_i^*/q^*_t can be taken as representing the "electrochemical porosity" of the oxide layer, but this is difficult to asses from a quantitative point of view. For determining the porosity and/or the roughness factors Da Silva et al. [8] proposed another technique based on the dependence of the capacitive current i_c on the scan rate v, observed in short capacitive potential region of about 100 mV (Figure 3.5).

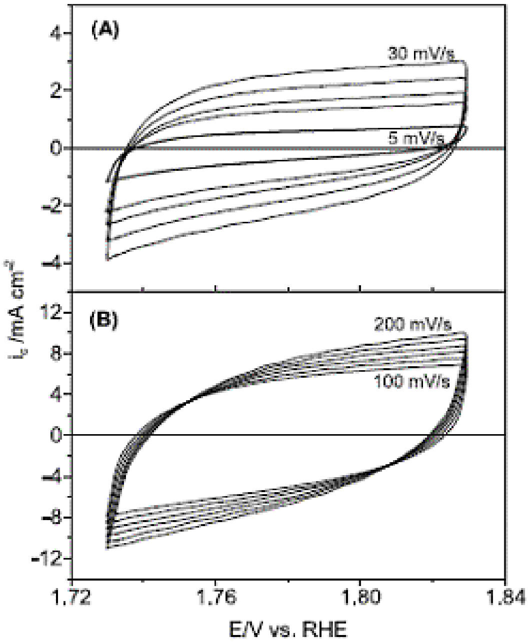

Figure 3.5. *Example of cyclic voltammograms covering a capacitive potential interval as a function of the potential sweep rate: (A) low v-range; (B) high v-range.*

In analogy with Trasatti and coworkers [6], the authors have correlated the two linear segments, observed in the low and high v domains of the i_c versus v plot (Figure 3.6), with the morphology of highly porous or rugged films. They have attributed the change in the slope observed in the high *v* domain to the exclusion of surface areas located in the more difficult-to-access regions.

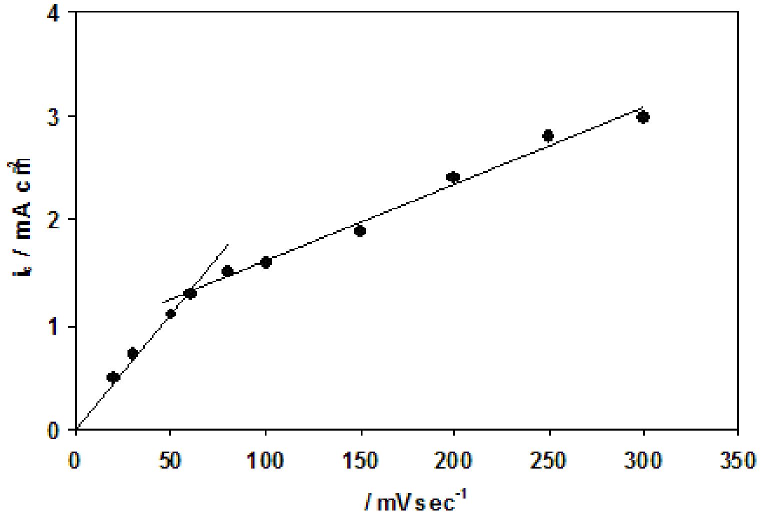

Figure 3.6. *Dependence of the capacitive voltammetric current (i_c) on the scan rate (v).*

Thus the slopes of the two linear parts of the i_c versus *v* plot give the total C_{dt}, and the external C_{de} differential capacity while the difference between them $C_{dt}-C_{de}$ gives the capacity C_{di} for the "internal" film regions and the ratio C_{di}/C_{dt} is the morphology factor φ. Both the electrochemical porosity and the morphology factor describe the ratio between the more-difficult-to-access and total surface areas and can take values between 0 and 1. Their physical meaning however is not exactly the same since the electrochemical porosity could include also solid state surface redox transitions *(SSSRT)* which possible occur at the electrode material, while the morphology factor should be free of the *SSSRT* or of the minor importance [8].

3.3 Steady-state polarisation

This technique involves applying a potential difference between the working and the reference electrodes and recording a current response when a steady state is reached. Current-potential curves provide information about kinetic parameters of the redox reaction investigated.

The theory for this type of analysis is reported in the previous chapter (2.3.1 The Butler–Volmer equation). Briefly, with large potential perturbations, since the mass-transfer controlled region is not involved, the kinetics of sluggish reactions can be investigated. In this potential region the back reaction (corresponding to one of the two branches in Figure 3.7) can be neglected.

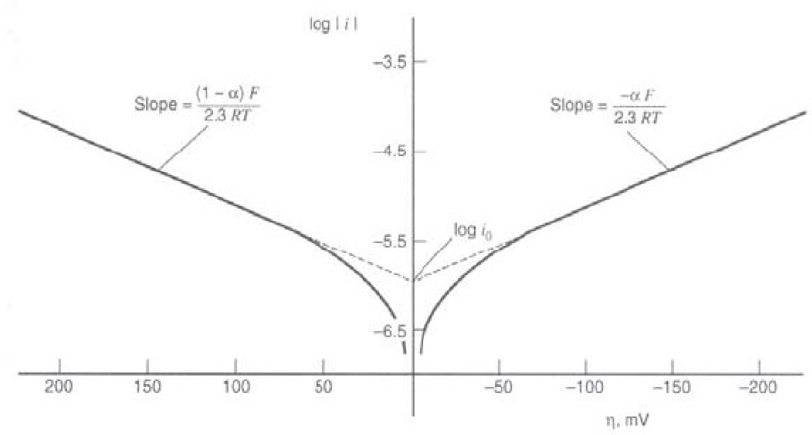

Figure 3.7. *Tafel plots for anodic and cathodic branches of the current-overpotential curve*

In this case the current-potential relations, for anodic process, can be written as:

$$\log|i| = \log i_0 + \frac{\alpha_A nF}{2.3RT}\eta \qquad (3.16)$$

$$\eta = -\frac{2.3RT}{\alpha_A nF}\log i_0 + \frac{2.3RT}{\alpha_A nF}\log|i| \qquad (3.17)$$

$$\eta = a + b\log i \qquad (3.18)$$

The plot of *log i vs η*, known as Tafel plot, is a useful device for evaluating the kinetic parameters. Tafel slope *(b)* and exchange current density *(i_0)* are two primary factors that describe the rate of charge transfer reaction. Exchange current density is a measure of the electrocatalytic properties, whereas Tafel slope is related to the reaction mechanism. A high exchange current density and a low Tafel slope value indicate a good electrocatalyst. Change of Tafel slope value is a clear indication of changes in electrocatalytic effects.

Frequently, the experimental Tafel curves show, at high overpotentials, a deviation from linearity, requiring correction for ohmic drop *(IR)* in order to permit an appropriate interpretation. The influence of ohmic drop on the polarisation curve can be written as:

$$E - IR = a + b\log I \tag{3.19}$$

where R is the total ohmic resistance, E is the electrode potential, a is a constant and b is the Tafel slope. R-value can be obtained when a perfect linearization of equation is verified. The experimental data to be used in the linearization procedure are the ones localised in the high overpotential domain where the influence of ohmic drop is more pronounced. The criterion used to determine the best linearization of the curve is based on the correlation coefficient of the high current data.

The nonlinearity of the Tafel lines can be due to uncompensated ohmic drop eventually in combination with a higher Tafel slope. Tafel slope can be obtained from the Tafel lines using two procedure [9]:

1. A straight line is drawn graphically from the linear part of the experimental curve in the low current range and extended to high currents. Here, deviation from the experimental point are determined (ΔE_{IR}) and plotted as function of current (I). If a straight line is obtained (Ohmic law), this indicates that deviation from linearity are only due to uncompensated ohmic drops, therefore, only one Tafel line is operating. The slope of the ΔE_{IR} *vs* I straight line gives the uncompensated resistance between the electrode surface and the orifice of the Luggin capillary, as well as the resistance of the oxide over-layer. If the ΔE_{IR} *vs* i data give a curve, it means that two different Tafel lines are probably operating, or that the drawn Tafel line is inaccurate.
2. A Tafel line in the presence of uncompensated ohmic drops, can be written as:

$$E = a + b\log I + RI \tag{3.20}$$

Derivation with respect to *I* gives:

$$\frac{dE}{dI} = \frac{b}{I} + R \tag{3.21}$$

Thus, a plot *ΔE/ΔI* (where *ΔE* and *ΔI* are the difference of two consecutive experimental points of potentiostatic curves) *vs 1/I* (where *I* is the mean value between two consecutive values) give a straight line whose slope is *b* and whose intercept is *R*. If more than one Tafel line exist, such a kind of plot will give a broken straight line whose slopes give the different Tafel slopes. The intercept *R* is that of the straight line at the highest currents.

The type of analysis describe above can only apply at high overpotentials. In order to use data obtained at potentials close to the equilibrium value where both forward and back reactions are significant it is necessary to employ the complete Butler-Volmer equation. However, as reported in the previous section, in this case kinetic informations about k^0 and the charge transfer resistance are directly available from some experiments.

Experimentally, steady state data can be recorded either:

1. using a point by point method where the potential is changed manually at intervals and the current read after a defined period;
2. using a very slow potential scan, 1-10 mV s^{-1}, and displaying the current directly.

The technique requires only very simple instrumentation, but, because of its long timescale, it suffer more than other experiments with problems from traces impurities and slow changes in the electrode surface.

3.4 Electrochemical impedance spectroscopy

Beginning in the 1970s, research electrochemists and materials scientists began to discover the power of Electrochemical Impedance Spectroscopy *(EIS)* as a tool for studying difficult and complicated systems. *EIS* is an electrochemical technique with applications in corrosion, battery development, fuel cell development, semiconductor development, sensor development, and physical electrochemistry. The reason for this popularity is the high information content of *EIS*: with a single experimental procedure encompassing a sufficiently broad range of frequencies, the influence of the governing physical and chemical phenomena may be isolated and distinguished at a given applied potential or current. In recent years, *EIS* has found widespread applications in the field of in situ characterization of materials and is being used increasingly as a tool to investigate nanosystems. This technique is capable of high precision, and it is frequently used to evaluate heterogeneous charge transfer parameters and to study the double-layer structure. *EIS* can provides a more thorough understanding of an electrochemical system than any other electrochemical technique and, in particular, it offers three advantages over dc techniques:

1) *EIS* techniques use very small excitation amplitudes which cause only minimal perturbation of the electrochemical system, reducing errors caused by measurement technique.
2) Because electrochemical impedance experiments provide data on both electrode capacitance and charge transfer kinetics, *EIS* techniques can provide valuable mechanistic information.
3) Because the method does not involve a potential scan, you can make measurements in low conductivity solutions where dc techniques.

The cell used for making impedance measurements is a typical electrochemical cell. The instrumentation (Figure 3.8) required includes a waveform generator to produce the sine waves and a potentiostat to control the potential: it must control both the dc potential as well as the added ac excitation voltage. The instrumentation must also contain a means of accurately measuring the ac components of both the voltage and the current and the phase relationship between them. This data are used to calculate the impedance of the system. Because of the complexity of optimizing and coordinating these ac measurements, a computer is generally used to run the experiment and to display the results in real time.

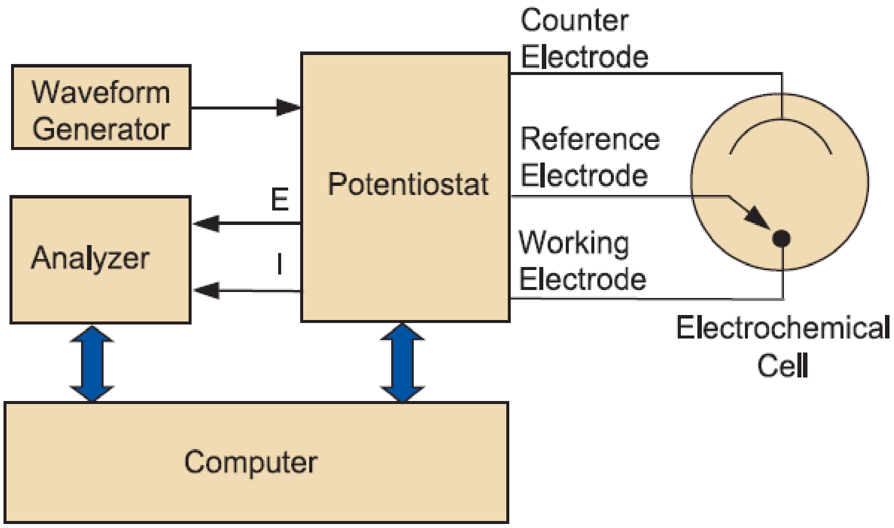

Figure 3.8. *A block diagram of the instrumentation used to make the EIS measurement.*

The data collected by the computer program should include the frequency of the ac waveform and either the magnitude and phase of the impedance at each frequency, or the real and imaginary components of the impedance, or perhaps both. Most programs allow the display of either these equivalent display formats: the Bode plot or the Nyquist plot. A small amplitude ac signal is applied to the sample by the potentiostat and the current response is analyzed to extract the phase and amplitude relationship between the current and the voltage signals.

When a three-electrode potentiostat is used, the impedance between the reference and working electrodes can be measured because the potentiostat controls and measures the voltage difference only between these two electrodes. The impedance at the counter electrode and the resistance through the bulk of the solution is not sensed.

In spite of the relative facility with which impedance data can be measured, in order to make reliable measurements some considerations must be made.

The number of cycles used to collect the data determines the precision of the measurement. At low frequencies, the trade-off between the length of the experiment and precision is a serious consideration. Although sampling many cycles would improve the precision of the measurement, to do so would lengthen the experiment and increase the chances that the sample changes during the experiment. The impedance is usually measured as a function of frequency over many decades, 10^{-4} to 10^{6} Hz. For this reason the measurement points are chosen logarithmically to get an even spread of points across the whole frequency range. This gives the high frequency data an equal weight with low frequency data. Making *EIS* measurements at very high or at very low impedances, or at very high frequencies, is a difficult task. At any of these extremes you may be able to make the measurement, but it may not be a meaningful or useful one. Many potentiostat manufacturers will specify the impedance and frequency limits for making reliable and accurate measurements that reflect the sample you are trying to study.

As reported above, electrochemical impedance is usually measured by applying an ac potential to an electrochemical cell and measuring the current through the cell. Suppose that we apply a sinusoidal potential excitation, the response to this potential is an ac current signal, containing the excitation frequency and it's harmonics. This current signal can be analyzed as a sum of sinusoidal functions (a Fourier series). *EIS* is normally conducted by applying a small ac signal (usually < 10 mV): this is done so that the cell's response is pseudo-linear. In a linear (or pseudo-linear) system, the current response to a sinusoidal potential will be a sinusoid at the same frequency but shifted in phase.

So, if the excitation signal, expressed as a function of time, has the form:

$$E(t) = E_0 \cos(\omega t) \tag{3.23}$$

in a linear system, the response signal, is shifted in phase and has a different amplitude:

$$I(t) = I_0 \cos(\omega t - \phi) \tag{3.24}$$

The impedance of the system *(Z)* can be calculate as:

$$Z = \frac{E(t)}{I(t)} = \frac{E_0 \cos(\omega t)}{I_0 \cos(\omega t - \phi)} = Z_0 \frac{\cos(\omega t)}{\cos(\omega t - \phi)} \qquad (3.25)$$

Using Euler's relationship, the impedance can be then represented as a complex number:

$$Z = \frac{E}{I} = Z_0 \exp(j\phi) = Z_0(\cos\phi + j\sin\phi) \qquad (3.26)$$

The expression for Z is composed of a real and an imaginary part. If the real part is plotted on the x-axis and the imaginary part on the y-axis of a chart, we get a Nyquist plot (Figure 3.9). Notice that in this plot the y-axis is negative and that each point on the Nyquist plot is the impedance at one frequency.

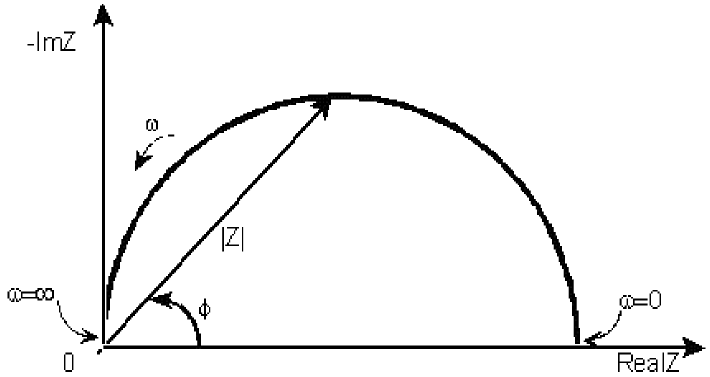

Figure 3. 9. *Nyquist plot.*

Figure 3.9 has been annotated to show that low frequency data are on the right side of the plot and higher frequencies are on the left. On the Nyquist plot the impedance can be represented as a vector of length |Z|. The angle between this vector and the x-axis is ϕ. Nyquist plots have one major shortcoming. When you look at any data point on the plot, you cannot tell what frequency was used to record that point. Another popular presentation method is the Bode plot (Figure 3.10). The impedance is plotted *vs* log frequency on the x-axis and both the absolute value of the impedance (|Z| = Z_0) and phase-shift on the y-axis. Unlike the Nyquist plot, the Bode plot explicitly shows frequency information.

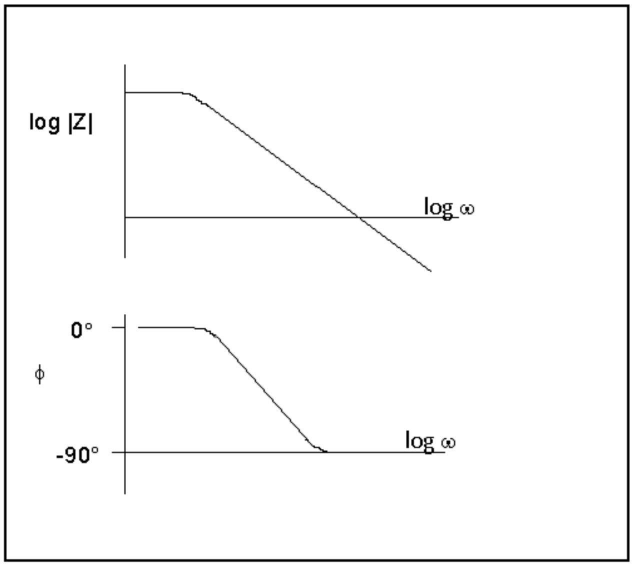

Figure 3.10. *Bode plots*

An electrochemical cell behaves as an impedance to a sinusoidal excitation. It should then be possible to represent its behaviour by an equivalent circuit of resistors and capacitors that pass current with the same amplitude and phase angle as the real cell does under a given excitation. So, *EIS* data are commonly analyzed by fitting them to an equivalent electrical circuit model. Most of the circuit elements in the model are common electrical elements such as resistors, capacitors, and inductors. To be useful, the elements in the model should have a basis in the physical electrochemistry of the system.

Some knowledge of the impedance of the standard circuit components is therefore quite useful. Table 3.1 lists the common circuit elements: the equations for both the admittance and the impedance are given for each element.

Equivalent element	Admittance	Impedance
R	$1/R$	R
C	$j\omega C$	$1/j\omega C$
L	$1/j\omega L$	$j\omega L$
Q (CPE)	$Y_0(j\omega)^n$	$1/Y_0(j\omega)^n$

Table 3.1. *Common electrical elements*

Notice that the impedance of a resistor is independent of frequency and it has only a real component. Because there is no imaginary impedance, the current through a resistor is always in phase with the voltage. The impedance of an inductor increases as frequency increases. Inductors have only an imaginary impedance component. As a result, an inductor's current is phase shifted 90 degrees with respect to the voltage. The impedance versus frequency behaviour of a capacitor is opposite to that of an inductor. A capacitor's impedance decreases as the frequency is raised. Capacitors also have only an imaginary impedance component. The current through a capacitor is phase shifted -90 degrees with respect to the voltage. Very few electrochemical cells can be modelled using a single equivalent circuit element. Instead, *EIS* models usually consist of a number of elements in a network. Both serial and parallel combinations of elements occur.

Among the common circuit elements, the Constant Phase Element (*CPE*) is extensively used in data fitting even if its physical meaning is controversial. The *CPE* is a non-intuitive circuit element that was “discovered” while looking at the response of real-world systems. The Nyquist plot of ideal systems would be a semicircle with the center on the x-axis, however, the observed plot was frequently depressed semicircle. These behaviour can be explained by a number of phenomena, depending on the nature of the investigated system. However, the common thread among these explanations is that some property of the system is not homogeneous or that there is some dispersion of the value of some physical property of the system.

As reported in Table 3.1, *CPE's* impedance is given by:

$$Z_{CPE} = \frac{1}{Y_o\,(j\omega)^n} \tag{3.27}$$

where Y_0 has the numerical value of the admittance ($1/|Z|$) at $\omega=1$ rad/s and its units are $S{\cdot}s^n$. A consequence of this simple equation is that the phase angle of the *CPE* impedance is independent of the frequency: this is the reason of *CPE’s* name. The parameter n represents the deviation from the ideal behaviour, being $n = 1$ for perfect capacitors. When n is close to 1, the *CPE* resembles a capacitor, but the phase angle is not 90°.

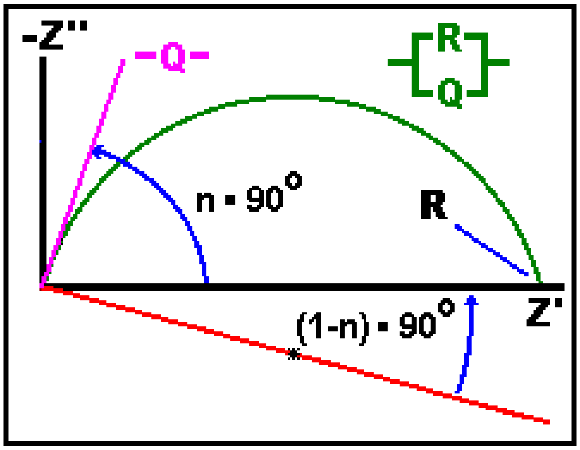

Figure 3. 11. *Nyquist Plot of a CPE*

The Nyquist Plot of a *CPE* is shown in Figure 3.11: for a *CPE* (symbolized here by Q), it is just a straight line which makes an angle of (*n*)*90°* with the x-axis as shown in pink in the Figure. The plot for a resistor (symbolized by *R*) in parallel with a *CPE* is shown in green. In this case the center of the semicircle is depressed by an angle of *(1-n) 90°.*

Several theories have been proposed to suggest the correct use of a *CPE,* but none has been universally accepted. Macdonald [10] points out that even though a particular theory may not give exactly *CPE* behaviour, very often *CPE* behaviour will fit experimental data so well that the deviations are totally masked by experimental noise and uncertainties. This is increasingly true as the complexity of a circuit model grows. In short, a *CPE* can provide a useful modeling element, even if the true nature of the system is unknown.

One physical explanation for *CPE* behaviour can be electrode roughness. For a rough, fractal, surface, the fractal dimension (*D*) of the surface is between 2 and 3: this means that the surface fills between 2 dimensions (i.e., it's absolutely flat) and 3 dimensions (i.e., the surface fills three dimensions, branching every-which-way through space, and resembling a porous cube). It has been shown [11] that for these electrodes, the interfacial impedance (double layer capacitance) is modified by an exponent, $n = 1/(D-1)$. For a smooth surface $D = 2$ and $n=1$, and the impedance is unchanged. For a highly contorted surface *D=3* and *n=0.5*. For a great many real metal or solid electrodes, the measured impedance in the double-layer region follows a power law, such as that for the *CPE*, with a value of *n* between *0.9* and *1.0*. The phase angle of this "capacitance" is not *90°* , but is given by *(n)90°*. When this "capacitance" is in parallel with a charge-transfer resistance, the Nyquist plot is the arc of a circle, but with the center of the circle below the x-axis: It is the "depressed semi-circle" shown in the Figure 3.4 on the previous page.

Another explanation is inhomogeneous reaction rates on a surface. This might be seen at polycrystalline metal surfaces or carbon electrodes with a distribution of active sites (with varying activation energies) on the surface. The literature shows that for a glassy carbon electrode, the *CPE* exponent correlates with the fraction of exposed edge plane orientation, not with the fractal dimension of the surface [12].

A third possible explanation may be varying thickness or composition of a coating. For example, if the bulk conductivity of a coating changes with distance through the coating, then the resultant impedance spectrum can closely approximate that of a *CPE* [13].

Many other physical phenomena must be at the origin of the *CPE* behaviour, but it is well possible that not all non-idealities correspond to *CPE* behaviours, although *CPEs* are extensively used as a 'fundamental' circuit element today.

3.4.1 Common Equivalent Circuit Models

The equivalent circuit model which fits the *EIS* data would suggest some chemical model, process, or mechanism which can be proposed and tested. However, the relative facility with which impedance data can be acquired and analyzed makes it all together too easy to just take some data, fit them to a simple equivalent circuit model, and then keep adding components to the circuit until you have a perfect fit. But, in many cases, it isn’t an easy task to establish when you should keep one model, rather than add one more circuit elements. So, taking account for the physical process it is always advisable, even if this means to not obtain a perfect fit.

The Randles cell is one of the simplest and most common cell models. The circuit components of a Randles cell can be easily equated to physical phenomena. It includes a solution resistance (R_s), a double layer capacitor (C_{dl}) and a charge transfer or polarization resistance (R_{ct} or R_p). The equivalent circuit for the Randles cell is shown in Figure 3.5.

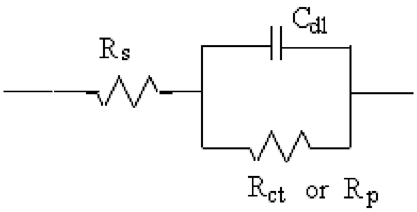

Figure 3.12. *Randles cell equivalent circuit*

The parallel elements were introduced because the total current through the working interface is the sum of a faradaic process and of double-layer charging. So, the double layer capacity is in parallel with the impedance due to the charge transfer reaction. Figure 3.13 is the Nyquist plot for a typical Randles cell.

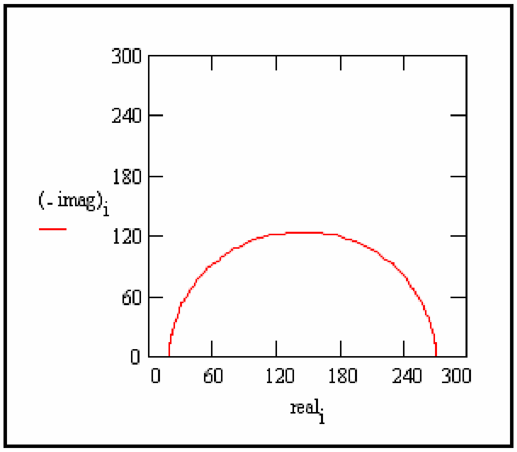

Figure 3.13. *Randles cell Nyquist plot*

The Nyquist plot for a Randles cell is always a semicircle. The solution resistance can found by reading the real axis value at the high frequency intercept. This is the intercept near the origin of the plot. The real axis value at the other (low frequency) intercept is the sum of the polarization resistance and the solution resistance. The diameter of the semicircle is therefore equal to the polarization resistance.

Figure 3.14 is the Bode plot for the same cell.

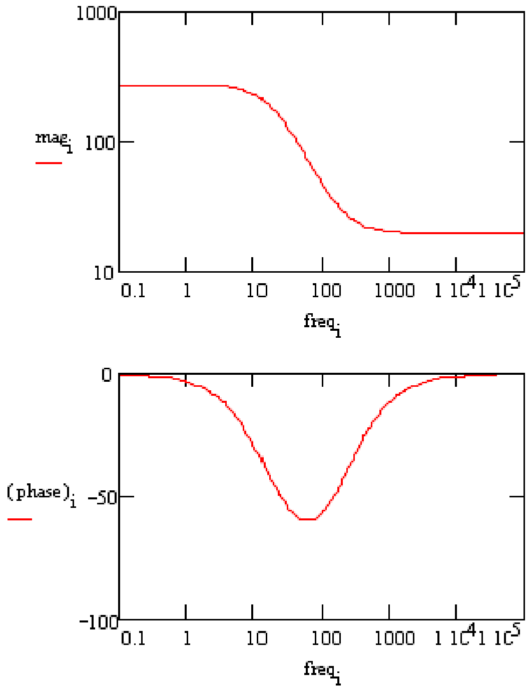

Figure 3.14. *Randles cell Bode plots*

The solution resistance and the sum of the solution resistance and the polarization resistance can be read from the magnitude plot. In particular, at high frequency, the solution resistance dominates the impedance and $log(R_S)$ can be read from the high frequency horizontal plateau. At the lowest frequency, charge transfer resistance also contributes to impedance, and $log(R_S+R_{ct})$ can be read from low frequency horizontal plateau. At the intermediate frequency, curve should be a straight line with a slope of –1. Extrapolating this line to the $log|Z|$ axis at $log\omega = 0$ yields the values of C_{dl} from relationship $|Z| = 1/\, C_{dl}$.

The phase angle does not reach 90° as it would for a pure capacitive impedance. If the values for R_s and R_p were more widely separated the phase would approach 90°. In addition to being a useful model in its own right, the Randles cell model is often the starting point for other more complex models like that in (Figure 3.15). Also in this case, the double-layer capacitance is regarded as a pure capacitance C_{dl} while the faradaic process is represented by an impedance, Z_F. The faradaic impedance of a system under mixed kinetic and diffusion control can be separated into a pure resistance due to charge transfer, R_{ct}, and a general impedance called Warburg impedance (Z_W) which is related to the mass transfer resistance (Figure 3.15).

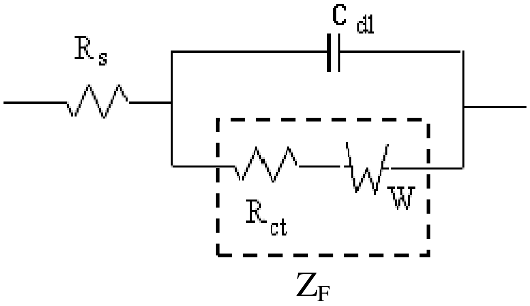

Figure 3.15. *Equivalent circuit with mixed kinetic and charge transfer control*

Diffusion can create the Warburg impedance: this impedance depends on the frequency of the potential perturbation. At high frequencies the Z_W is small since diffusing reactants don't have to move very far. At low frequencies the reactants have to diffuse farther, thereby increasing the Z_W. The equations for the "infinite" Warburg impedance and admittance are reported in Table 3.2.

Equivalent element	Admittance	Impedance
W (infinite Warburg)	$Y_0\sqrt{(j\omega)}$	$1/Y_0\sqrt{(j\omega)}$
O (finite Warburg)	$1/Y_0\sqrt{(j\omega)}Coth(B\sqrt{(j\omega)})$	$Tanh(B\sqrt{(j\omega)})/Y_0\sqrt{(j\omega)}$

Table 3.2. *Warburg elements*

On a Nyquist plot the infinite Warburg impedance appears as a diagonal line with a slope of 0.5 (Figure 3.16).

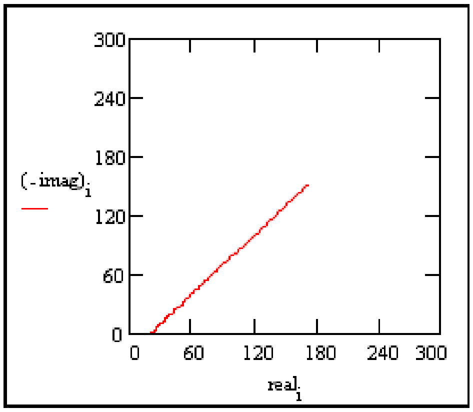

Figure 3.16. *Nyquist plot of a Warburg impedance*

On a Bode plot, the Warburg impedance exhibits a phase shift of 45° (Figure 3.17).

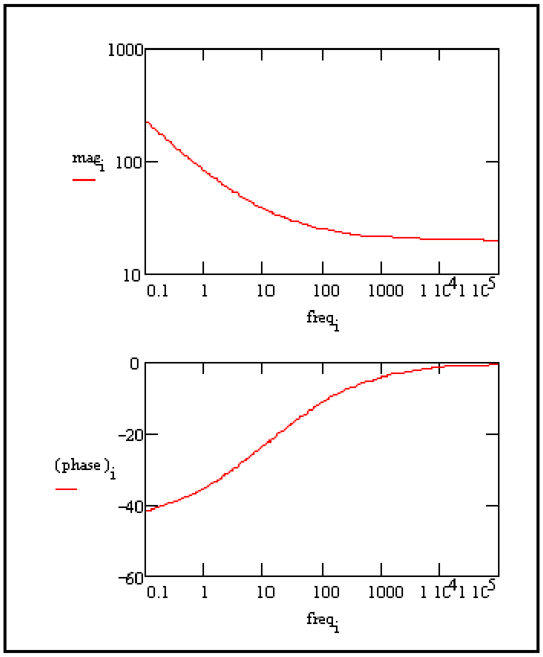

Figure 3.17. *Bode plot of a Warburg impedance*

This form of the Warburg impedance is only valid if the diffusion layer has an infinite thickness. Quite often this is not the case. If the diffusion layer is bounded, the impedance at lower frequencies no longer obeys the equation above. This more general equation is also reported in Table 3.2 and it is called the "finite" Warburg.

In contrast to R_S and C_{dl} which are nearly ideal circuit elements, the faradaic impedance usually changes with the frequency. Also in this case, important chemical information can be obtained from the Nyquist plot. A Nyquist plot for an electrochemical system with the regions of mass-transfer and kinetic control at low and high frequencies, respectively, is shown in Figure 3.18.

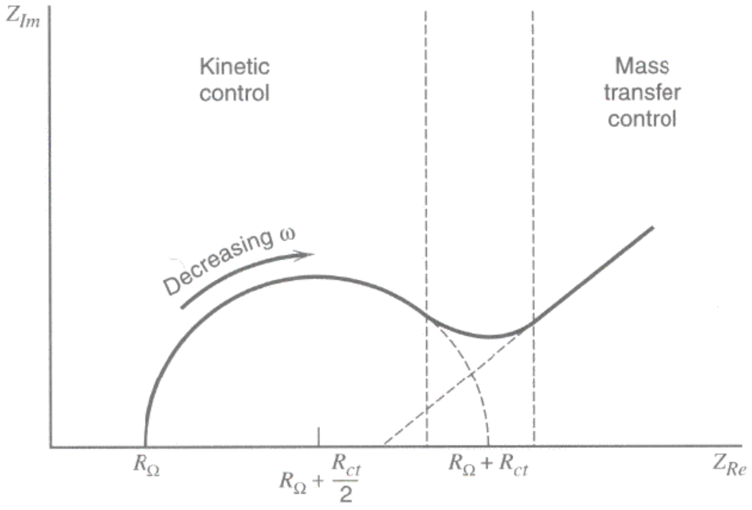

Figure 3.18. *Nyquist plot for mixed control circuit*

This representation corresponds to the Randles equivalent circuit in which the faradaic impedance, is separated into the charge-transfer term and the Warburg term. In the low frequency region, the Nyquist plot should become linear and have unit slope. In this region the frequency dependence only comes from Warburg impedance terms. At very high frequencies, the Warburg impedance becomes unimportant in relation to R_{ct}. The imaginary component of Z becomes a pure capacitance C_{dl} that constitutes zero impedance at high frequencies. All of the current is charging current, the only impedance being due to the charge-transfer resistance, R_{ct}. At lower frequencies the capacitance makes an impedance contribution that becomes very important at very low frequencies; hence none of the current will go through C_{dl} and the imaginary impedance falls off again.

The impedance plot for a real system combines the two limiting cases explained previously. The features will depend more particularly on the charge transfer resistance and its relation to the Warburg impedance. If the system is kinetically sluggish, it will have a large R_{ct} but only a limited region where mass transfer is an important factor. In other cases, R_{ct} can be extremely small relative to the solution resistance and to the Warburg element over a wide range of frequencies. The kinetics of the system is so fast that mass transfer only is seen and the circular region is not well defined.

The models discussed earlier are physical models. The choice of which physical model applies to a given cell is made from knowledge of the cell's physical characteristics. Models can also be partially or completely empirical. The circuit components in this type of model are not assigned to physical processes in the cell. The model is chosen to given the best possible match between the model's impedance and the measured impedance.

Physical models are generally preferable to empirical models. However, it is only in the simplest cases that individual circuit elements can be identified with processes occurring in the electrochemical cell. Commercial program or self-made fitting programs have normally been used to make a quantitative fitting by adopting the proper electrical circuit. But, for a given impedance spectra, there may be several electrical circuits which can all provide a good fitting making it difficult to select the proper equivalent electrical circuit model for the electrode system.

Parallelly, a mathematical modelling method for the *EIS* data based on the impedance theory and reaction mechanism can be developed, but it is not easy to simulate the experimental impedance quantitatively by using this approach. Moreover, the traditional method employed for the simulation of *EIS* by a mathematical modelling requires guess values for all the kinetics parameters which increase the difficulty of obtaining precise results. The combined use of equivalent electrical circuit approach (reported above) and the mathematical modelling of the faradaic impedance can be capable of solving problems such as the uncertainty of the physical significant of the electrical parameters and the difficulty of quantitative fitting of the latter method [14]. The goal of this analysis is to accurately simulate the impedance spectra with a set of kinetics parameters extracted by the combined use of equivalent electrical circuit method and the mathematical modelling. This analysis starts with the definition of a reaction model and then considers the theoretical derivation of the Faradaic impedance and establishes a relationship between the electrical parameters of equivalent electrical circuit and the electrochemical parameters of the Faradaic impedance. The impedance data obtained at different potentials are then fitted for a general equivalent electrical circuit. From the definition of the electrochemical parameters, the kinetics parameters are subsequently derived and a quantitative simulation is realized with these extracted parameters.

3.4.2 EIS and Mott-Schottky analysis [15]

Finally, we want to underline that the semiconductive properties of the oxide films can be useful characterized using *EIS* and Mott-Schottky analysis. To this aim, some knowledge of the electrochemistry of semiconductors can be very useful. The properties of semiconductor electrodes, and their differences from those of metallic electrodes, can be understood by examining the electronic structures of these materials [16].

The electronic structure of these solids is typically discussed in terms of energy bands, which are made up of the atomic orbitals of the individual atoms. As a result of the large number of orbitals, the difference in energy between adjacent molecular orbitals within a given energy band is so small that the band can be effectively considered a continuum of energy levels. The highest and lowest energy levels of a band are referred to as the band edges. The energy bands of interest are the highest occupied (valence band) and the lowest unoccupied (conduction). The difference in energy between the upper edge of the valence band and the lower edge of the conduction band is the band gap which determines the properties of the material. For metals, the conduction and valence bands overlap, so the conduction band can be readily occupied while, for insulators, the band gap is sufficiently large that electrons cannot be promoted from the valence band to the conduction band. However, for semiconductors, the band gap is not as large, and electrons can be moved into the conduction band.

The promotion of electrons leaves a positively charged vacancy in the valence band, which is referred to as a hole. These holes can be moved through space by the transfer of an electron to the vacancy; therefore, holes are considered to be mobile. Electrons can be excited to the conduction band either thermally or photochemically. However, there is another method for generating charge carriers (i.e., electrons or holes) within a semiconductor, referred to as doping. Doping involves the addition of a different element into the semiconductor. Undoped semiconductors are referred to as intrinsic semiconductors. Doped semiconductors in which the majority charge carriers are electrons are referred to as n-type semiconductors, whereas those in which holes are the majority charge carriers are referred to as p-type semiconductors.

Another important concept in discussion of solid state materials is the Fermi level which is defined as the energy level at which the probability of occupation by an electron is ½. For an n-type semiconductor, the Fermi level lies just below the conduction band, whereas for a p-type semiconductor it lies just above the valence band. At an (idealized) interface between a semiconductor electrode and an electrolyte solution, so that the two phases are in equilibrium, their electrochemical potential must be the same. The electrochemical potential of the solution is determined by the redox potential of the electrolyte solution, and the redox potential of the semiconductor is determined by the Fermi level. If the redox potential of the solution and the Fermi level do not lie at the same energy, a movement of charge between the semiconductor and the solution is required in order to equilibrate the two phases. The excess charge that is now located on the semiconductor does not lie at the surface, as it would for a metallic electrode, but extends into the electrode for a significant distance (100-10.000 Å). This region is referred to as the space charge region, and has an associated electrical field. Hence, there are two double layers to consider: the interfacial electrode/electrolyte double layer, and the space charge double layer.

For an n-type semiconductor electrode at open circuit, the Fermi level is typically higher than the redox potential of the electrolyte, and hence electrons will be transferred from the electrode into the solution. Therefore, there is a positive charge associated with the space charge region, and this is reflected in an upward bending of the band edges. Since the majority charge carrier of the semiconductor has been removed from this region, this region is also referred to as a depletion layer. For a p-type semiconductor, the Fermi level is generally lower than the redox potential, and hence electrons must transfer from the solution to the electrode to attain equilibrium. This generates a negative charge in the space charge region, which causes a downward bending in the band edges. Since the holes in the space charge region are removed by this process, this region is again a depletion layer. As for metallic electrodes, changing the potential applied to the electrode shifts the Fermi level. The band edges in the interior of the semiconductor (i.e., away from the depletion region) also vary with the applied potential in the same way as the Fermi level. However, the energies of the band edges at the interface are not affected by changes in the applied potential: the change in the energies of the band edges reflects in a change of the magnitude and direction of band bending.

There are three different situations to be considered:

a) at a certain potential, the Fermi energy lies at the same energy as the solution redox potential (Figure 3.19b and 3.20b). There is no net transfer of charge, and hence there is no band bending. This potential is therefore referred to as the flatband potential, E_{fb}.

b) depletion region arises at potentials positive of the flatband potential for an n-type semiconductor and at potentials negative of the flatband potential for a p-type semiconductor (Figure 3.19a and 3.20c).

c) at potentials negative of the flatband potential for an n-type semiconductor, there is now an excess of the majority charge carrier (electrons) in this space charge region, which is referred to as an accumulation region (Figure 3.19c). An accumulation region arises in a p-type semiconductor at potentials more positive than the flatband potential (Figure 3.20a).

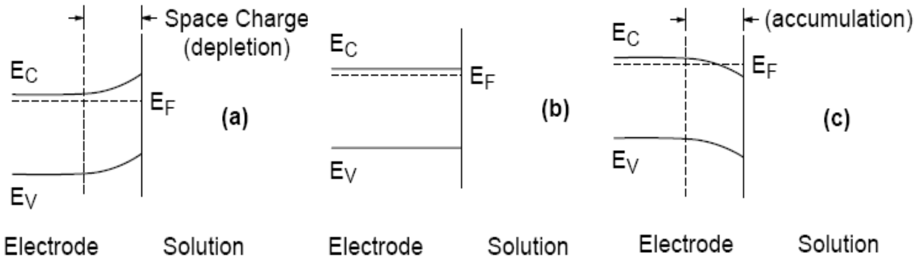

Figure 3.19. *Effect of varying the applied potential (E) on the band edges in an n-type semiconductor. a) E > E_{fb}, b) E = E_{fb}, c) E < E_{fb} [15]*

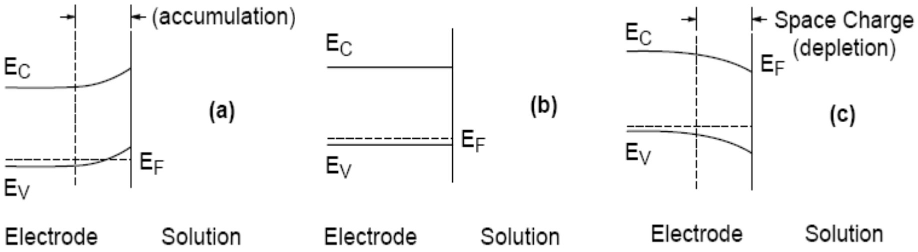

Figure 3.20. *Effect of varying the applied potential (E) on the band edges in a p-type semiconductor. a) E > E_{fb}, b) E = E_{fb}, c) E < E_{fb} [15]*

The charge transfer ability of a semiconductor electrode depends on whether there is an accumulation layer or a depletion layer. If there is an accumulation layer, the behavior of a semiconductor electrode is similar to that of a metallic electrode, since there is an excess of the majority of charge carrier available for charge transfer. In contrast, if there is a depletion layer, then there are few charge carriers available for charge transfer, and electron transfer reactions occur slowly, if at all.

There are a number of experiments used to measure the various parameters discussed above. As reported above, acquisition of Mott-Schottky plots (inverse square of space charge layer capacitance, C_{sc}^{-2}, versus semiconductor electrode potential E) is an usual way for semiconductor materials electrochemical characterisation [17-19]. This method involves measuring the apparent capacitance as a function of potential under depletion condition and is based on the Mott-Schottky relationship:

$$\frac{1}{C_{SC}^{2}} = \frac{2}{e\varepsilon\varepsilon_0 N}\left(E - E_{fb} - \frac{kT}{e}\right) \tag{3.28}$$

where C_{sc} = capacitance of the space charge layer; ε = dielectric constant of diamond; ε_0 = permittivity of free space; E applied bias potential; E_{fb}= flat band potential; N= donor density (electron donor concentration for an n-type semiconductor or hole acceptor concentration for a p-type semiconductor); k = Boltzman constant, and T = absolute temperature.

Mott-Schottky plot gives doping density by the slope of the straight line and flatband potential by the intercept. The capacitance values are calculated from impedance measurements.

The model required for the calculation is based on two assumptions:

1. there are two capacitances to be considered, that of the space charge region and that of the double layer. Since these capacitances are in series, the total capacitance is the sum of their reciprocals. As the space charge capacitance is much smaller than double layer capacitance (2-3 orders of magnitude), the contribution of the double layer capacitance to the total capacitance is negligible. Therefore, the capacitance value calculated from this model is assumed to be the value of the space charge capacitance.
2. the equivalent circuit used in this model is a series combination of a resistor and a capacitance (the space charge capacitance). The capacitance is calculated from the imaginary component of the impedance (Z") using the relationship:

$$Z^{"} = \frac{1}{2\pi \cdot f \cdot C} \tag{3.29}$$

The model is adequate provided the frequency is high enough (on the order of kHz). A given frequency can be selected, and the imaginary component of the impedance can be calculated at this frequency for each potential. Alternatively, a series combination of a resistor and a capacitor can be used as an equivalent circuit to fit the experimental data. This process will automatically generate the capacitance values at the different frequencies. However, in order for the results from this latter approach to be accurated, the equivalent circuit used must be valid over the entire frequency range.

Electrochemical determination of these parameters is simple when energy band edges are pinned at the surface and ac response of space charge layer capacitance can be separated in frequency range from other interfacial structures and processes, which is an usual case for stationary ideally polarisable semiconductor-electrolyte interface. Complications come with surface states and Faradaic processes that require frequency response analysis by impedance spectroscopy for extraction of space charge layer capacitance from the total ac response [19-24]. Common impedance spectroscopy is a stationary technique and this makes the problem, since complex semiconductor/electrolyte interfaces are often non-stationary, especially in microheterogeneous systems where the advantages of electrochemical characterisation could be exceptionally important. New opportunities for non-stationary interface frequency response analysis emerge from potentiodynamic electrochemical impedance spectroscopy (*PDEIS*) [25, 26].

3.5 References

[1] J.B.E. Randles, Trans.Faraday Soc. 44 (1948) 327

[2] R.S.Nicholson, I. Shain, Anal. Chem. 36 (1964) 706

[3] S. Trasatti In: J. Lipkowski and P.N. Ross (Eds), The Electrochemistry of Novel Materials, VCH, Weinheim, 1994

[4] M. Santana, L. De Faria, J. Boodts, Electrochim. Acta 49 (2004) 1925

[5] R. Boggio, A. Carugati, G. Lodi, S. Trasatti, J. Appl. Electrochem. 15 (1987) 828

[6] R. Boggio, A. Carugati, S. Trasatti, J. Appl. Electrochem. 17 (1987) 828

[7] G. Spinolo, S. Ardizzone, S. Trasatti, J. Electroanal. Chem. 423 (1997) 49

[8] L.M. Da Silva, L.A. De Faria, J.F.C. Boodts, Electrochim. Acta 47 (2001) 395

[9] N. Krstajic, S. Trasatti, J. Electrochem. Soc. 142 (1995) 2675

[10] J.R. Macdonald, Impedance Spectroscopy, J. Wiley and Sons Inc., New York, 1987

[11] W.H. Mulder, J.H. Sluyters, T. Pajkossy, I. Nyikos, J. Electroanal. Chem. 285 (1990) 103

[12] C.H. Kim, S.I. Pyun, J.H. Kim, Electrochim. Acta 48 (2003) 3455

[13] C.A. Schiller, W. Strunz, Electrochim. Acta 46 (2001) 3619

[14] J.M. Hu, J.Q. Zhang, C.N. Cao, I. M. Hsing, Electrochim. Acta 49 (2004) 5227

[15] Adrian W. Bott, Electrochemistry of semiconductors, Ph.D. Bioanalytical Systems, Inc. 2701 Kent Avenue West Lafayette, IN 47906-1382

[16] A.J. Bard, L.R. Faulkner, “Electrochemical Methods,” Chap.14, Wiley, 1980

[17] V.A. Myamlin, Y.V. Pleskov, Electrochemistry of Semiconductors, Plenum Press, New York, 1967

[18] S.R. Morrison, Electrochemistry at semiconductor and oxidized metal electrodes, Plenum Press, New York, 1980

[19] A.J. Nozik, R. Memming, J. Phys. Chem. 100 (1996)13061

[20] D.J. Blackwood, Electrochim. Acta 46 (200) 563

[21] J. Marsh and D. Gorse, Electrochim. Acta 43 (1998) 659

[22] W. Simons, L. Pauwels, A. Hubin, Electrochim. Acta 47 (2002) 2169

[23] A. Meier, D.C. Selmarten, K. Siemoneit, B.B. Smith, A.J. Nozik, J. Phys. Chem. B 103 (1999) 2122

[24] W. Gomes, D. Vanmaekelbergh, Electrochim. Acta 41 (1996) 967

[25] G.A. Ragoisha, A.S. Bondarenko, Electrochim. Acta 50 (2005) 1553

[26] G.A. Ragoisha, A.S. Bondarenko, Solid State Phenomena 90-91 (2003) 103

Chapter 4

Active electrodes in alkaline media: Cobalt oxide electrodes

4.1 Introduction

Electrochemically produced hydrogen through alkaline water electrolysis is expensive at the present because the evolution of oxygen at the anode involves a high overpotential in aqueous solutions. The electrocatalysis of oxygen evolution reaction on conductive metallic oxide electrodes has been a topic of great interest in electrochemistry for long time, since these surface catalysts make possible to improve significantly the energy balance of the cell. It is known that oxygen overpotentials are efficiently decreased by the application of mixed oxides containing cobalt in different valence states [1]. The literature reports several studies on spinel-type Co_3O_4 electrodes showing good efficiency and long-term performance in alkaline solutions [2-10]. In spite of the large number of publications devoted to these electrodes, the mechanism of oxygen evolution on these anodes is still a matter of discussion.

Electrocatalytic activity of such oxides is generally related to electronic and geometric factors. The first is related to the chemical composition of the oxide layer and physical-chemical properties of the oxide (e.g. electronic structure, crystallinity); the last factor is directly linked to the morphology of the film. Nevertheless, these properties are seriously influenced by the preparation and deposition techniques used during the electrode manufacture. Therefore, also the precursor nature, calcinations temperature, as well as the thickness and conductivity of the metal oxide deposit are of growing scientific interest [11-13].

Different methods have been developed for cobalt oxide preparation, such as thermal decomposition of salt solution precursors [14-21], spray pyrolysis [22, 23] chemical spraying method [6, 22, 24], freeze drying method [25], plasma sputtering [26, 27], the sol-gel technique [28-31] and electrochemical techniques [32-38]. Most of these methods require relatively high temperatures: low temperature techniques are attractive, because they are compatible with a wide range of substrate materials and they favour the production of high effective surface areas.

In particular, the sol-gel method is able to produce a stable pure oxide phase at relatively low temperature (< 300 °C) and higher real surface area than that obtained by other simple metal oxide synthesis. It requires inexpensive equipment and allows the coating of rather large surfaces in a controlled and homogeneous manner [29, 39-42]. Several excellent reviews on the sol-gel method can be found in literature [43-46]. Following this route, from hydro-alcoholic solutions of metal alkoxides or other complexes, solid gels are formed, by hydrolysis and condensation polymerization reactions at low temperature; the gels, subjected to controlled thermal treatments, produce the oxides of the starting metals, which, given their morphological and structural characteristics and their extreme purity, show to be especially promising for many applications, including those in the field of catalysis. In this method, the morphology of the product is determined by the tridimensional mesostructure of a surfactant which acts as a nucleant and is removed after the synthesis of the inorganic material. The correct design of the synthesis formulation and of the characteristics of the surfactant used lead to liquid-crystalline phases of different structure, hence to materials with pores of chosen size depending on the final application of the material. Some disadvantages are still connected to the classic sol-gel technologies, related to economic factors (high cost of the alkoxides) and to technical-scientific details (long gelling times, imperfect control of particle size) [47, 48].

Therefore, variants or alternate routes to the classic method have been proposed: a very promising technique is based on a sol gel method in combination with an auto-combustion step [49, 50]. In this method, gel precursors are prepared starting from aqueous solutions of metal nitrates and an organic complexant, citric acid being the most frequently used. The gels, when moderately heated (200-250°C) on a plate, react with a selfpropagating process, which rapidly converts them into the final product.

For this reason, in our research work, examines the behaviour of Co_3O_4 powder electrodes obtained by a sol-gel autocombustion route. The properties of the sol-gel Co_3O_4 sample were firstly compared with those of commercial nanosized Co_3O_4 powder samples. Then, the attention has been paid on the sol-gel Co_3O_4 sample, which is the most promising, to obtain specific information about mechanism and kinetics of the oxygen evolution reaction at this electrode material. In particular, the relationships between Faradaic admittance equation, equivalent circuit and kinetic parameters are derived and applied to reaction models involving one adsorbed intermediates.

4.2 Experimental conditions

Materials - Co_3O_4 powder was synthesized by a sol-gel autocombustion method [50]. $Co(NO_3)_2 \cdot 6H_2O$ (Aldrich, 98%) and Citric Acid (Aldrich, 99.5%) respectively were used as sources of metal ions and chelating-fuel agent. Aqueous solutions of them (1:1 molar ratio) were used in which ammonia (NH_4OH 30%) was added in order to adjust the pH value to about 7. The whole process was carried out under constant stirring. The solution was heated at 90°C until a gel was formed. The gel was put in a pre-heated oven at 300°C, at which a self-propagating combustion reaction occurs, leading to the formation of nanosized Co_3O_4 powder. The properties of the sol-gel Co_3O_4 sample (*SG*) were compared with those of commercial nanosized Co_3O_4 (Fluka) using either untreated (*C*) or thermally treated at 900◦C (*CT*) powder samples.

Electrodes - The electrodes were assembled by mixing the cobalt oxide powder with a Teflon-water dispersion; the mixture was painted on titanium supports ($1cm^2$) and then dried at 90°C for about three hours. Before deposition of the oxide, the titanium supports were degreased with isopropanol and etched for 5 minutes with boiling 10% oxalic acid. The cobalt oxide load was about 3 – 4 mg/cm^2.

Physicochemical characterisation - In order to characterize the powders, structural information was obtained employing X-ray diffractometer Seifert RX 7 using CuKα radiation. The powder surface area was measured by nitrogen physisorption (BET method) using a Sorptomatic 1990 System (Fison Instruments). Before the analysis, the samples were evacuated at 180°C for 18 h using the heating rate of 1°C min^{-1}.

Electrochemical measurements - The experiments were performed in a batch three electrode cell (Figure 4.1) in which Ti/Co_3O_4 worked as anode, while a large platinum sheet was the counter electrode. The reference was a saturated calomel electrode (*SCE*), connected to the cell by a Luggin capillary to minimize uncompensated ohmic drops: all the potential values in this paper are referred to *SCE*.

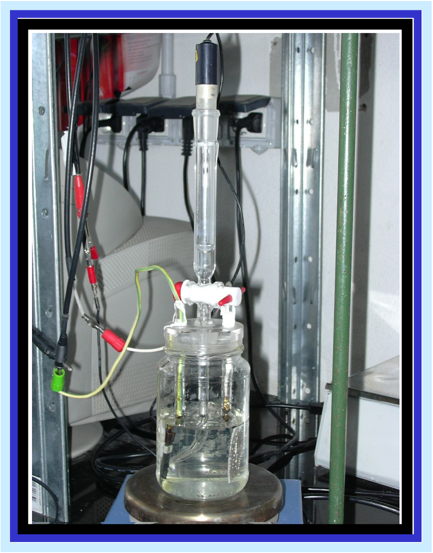

Figure 4.1. *Batch three electrode cell*

The electrochemical runs were carried out in 1.75 M NaOH. A potentiostat (Model 7050 AMEL) and a frequency response analyser (FRA, Model 7200 AMEL) were used to perform voltammetric and polarization analyses as well as spectroscopic analyses.

Electrochemical impedance spectroscopy measurements were performed at different bias potentials (from open circuit up to oxygen evolution potential), to which a sinusoidal signal with an excitation amplitude of 10 mV was superimposed. The impedance spectra were recorded in a range of frequency from 100 kHz to 0.1 Hz. The frequency was swept logarithmically from the high frequency and the electrochemical was plotted by 16 points per decade of the frequency. Zassist software was used to drive the experimental runs. The resulting curves were fitted to suitable equivalent circuits by using the ZsimpWin software. The fitting was made based on the complex nonlinear least squares (*CNLS*) method.

4.3 Results and discussion

4.3.1 Physicochemical analysis

The XRD pattern of the synthesized Co_3O_4 powder along with those of the reference samples are shown in Figure 4.2.

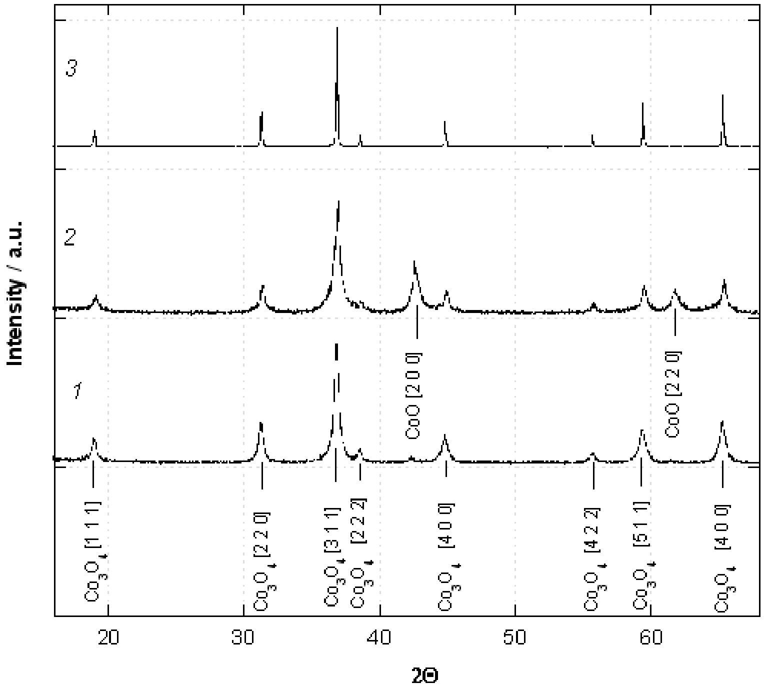

Figure 4.2. *XRD of the SG (1), C(2), and CT (3) samples.*

The average crystallite size of the samples, estimated from the X-ray peak broadening of the (311) diffraction peak using Scherrer's equation with Warren's correction [51] is summarized in Table 4.1 together with the surface area of the samples obtained by BET method.

Sample	**Co_3O_4 XRD Average Particle Size (nm)**	**SA_{BET} (m^2/g)**
SG	20	40
C	11	-
CT	94	1

Table 4.1. *Average crystallite size and surface area of SG, C, CT samples.*

The *XRD* pattern of the untreated commercial powder confirms its nanosized structure and reveals the coexistence of a large amount of an undesired phase of CoO, which demonstrated to be non catalytic for *OER*. The thermal treatment at 900°C for one hour of the commercial product induces the complete transformation of CoO into Co_3O_4, but an increasing in the particle size of the active phase is also measured at the end of the treatment. The sol-gel autocombustion method allows to obtain a nanosized spinel Co_3O_4 (PDF_431003) in which the undesired phase is practically absent. As can be observed in Figure 4.2, a faint peak at about $2\theta = 42°$ corresponding to the main reflection of CoO phase, is just visible.

4.3.2 Electrochemical analysis

4.3.2.1 Open circuit potential

The electrode potential is an intensive quantity which does not depend on the morphology but only on the surface proportion of active species. The open circuit potential *(OCV)* is the potential of the working electrode relative to the reference electrode when no potential or current is being applied to the cell. The *OCV* changes as a function of time contains abundant information of the interfacial structure and electron transfer kinetics on an electrode surface. Positive values of the open circuit potentials ranging from 0.07 to 0.17 V vs SCE were measured using C samples while in the case of SG samples the *OCV* values varied from -0.26 to -0.3 V. As suggested by Svegl et al. [11], this behaviour could be correlated to the Co(III)/Co(II) ratio in the films structure. The most positive value of *OCV* was measured when the electrode was prepared using commercial Co_3O_4 sample due to the higher percentage of CoO.

4.3.2.2 Cyclic voltammetric studies

When the anodic process of OER at this material is concerned, possible transformations of the solid phase should be considered, since different varieties of Co oxide species and their relevant allotropic phases can be involved in the electrochemical processes [52]. The spinel structure of Co_3O_4 (Figure 4.3) can be written as $Co^{2+}(Co_2^{3+})O_4$ in which trivalent ions are in the octahedral sites while the bivalent ions Co(II) are tetrahedrally coordinated with oxygen ions.

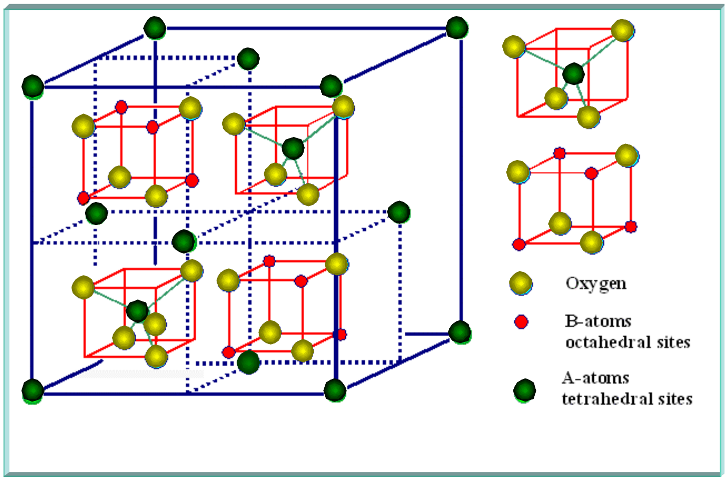

Figure 4.3. *Spinel structure of* Co_3O_4.

During an oxidative run the Co(II) species can be converted to Co(III) containing species such as Co_3O_4, Co_2O_3, $CoHO_2$, and different crystallographic forms of CoOOH [52].

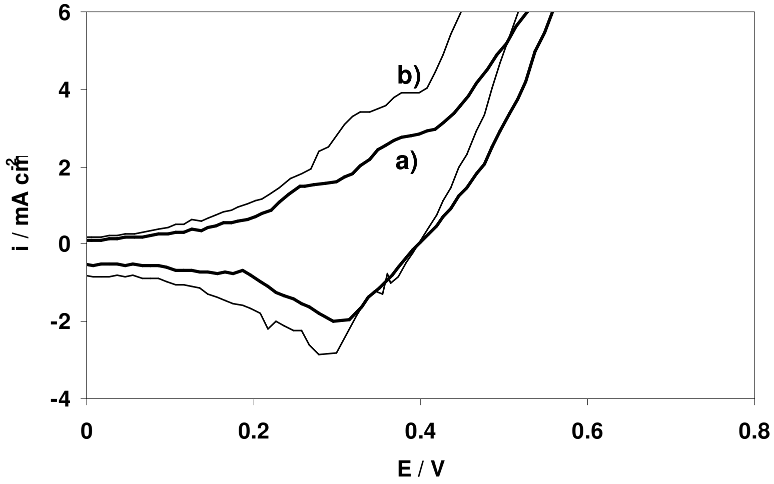

Figure 4.4. *Cyclic voltammograms at sol-gel Co_3O_4 electrode in 1.75 M NaOH at 20 (a) and 100 (b) mV s^{-1}.*

An example of the voltammograms obtained in 1.75 M NaOH, by cycling the potential between open circuit potential and a potential in the oxygen evolution region ($E \geq +0.45$ V), is displayed in Figure 4.4 which illustrates the trends obtained at 100 and 20 mV/s.

As it can be seen, not well defined peaks are obtained at all the potential scan rates (ν): the observed broadness of the peaks could be connected with roughness and porosity of the structure. As suggested by Filoche *et al.* [53], materials with a high degree of porosity/roughness present a wide potential distribution throughout the surface which affects the energy of the active site. Two wave-shaped peaks can be observed at lower scan rate in the forward scan at about 0.26 and 0.38 V respectively. According to the literature, the peak observed at 0.26 V may be attributed to the oxidation of Co(II) which is present in the lattice structure, to Co(III) containing species [13, 52]:

$$\mathrm{Co(II)_s + OH^-} \xrightarrow{-e^-} \mathrm{Co(II)(OH)_{ad}} \xrightarrow{-e^-} \mathrm{Co(III)(OH)_{ad}} \qquad (4.1)$$

The peak observed just before the rising current due to oxygen evolution may be attributed to the redox couple Co(III)/Co(IV) [29, 31, 54] which leads to the formation of the specific catalytic phase for OER [24]:

$$\mathrm{Co(III)_s} + \mathrm{OH^-} \xrightarrow{-e^-} \mathrm{Co(III)(OH)_{ad}} \xrightarrow{-e^-} \mathrm{Co(IV)(OH)_{ad}} \qquad (4.2)$$

Thus, different sites containing Co(III) and Co(IV) can be originated during the oxidative process which can in turn constitute active sites for adsorption of OH^- during *OER* from alkaline solution. Only one broad peak, attributable to the reduction of Co(IV) to Co(III) species, is observed in the reverse scan at a potential value near to that of the related oxidation peak: the system shows a quasi-reversible behaviour, the slight difference between anodic and cathodic peaks may be due to uncompensated ohmic drops or to the formation of a TiO_2 interlayer [55].

By analyzing voltammograms further information regarding the morphology and composition of the oxide layer could be obtained. As reported above, the peak position gives information about the chemical nature of active sites, while the peak area is proportional to the number of sites oxidized and reduced [56]. Since the peak resolution is often difficult, the voltammetric charge over the whole potential range *(q^*)* can be taken only as a relative measure of the electrochemically active surface area [3, 57]. This cannot be easily converted into an absolute value because of the possible influence of the *SSSRT*. However, the value of q^* is very useful, often essential, when different electrodes or different preparation procedures are being compared [55]. Integration of the voltammetric curves in the potential range between *OCV* and 0.6 V *vs SCE* provided the anodic charge *(q^*)* transferred during the potential scan. The values of 28 mC cm^{-2}, 20 mC cm^{-2}, and 11 mC cm^{-2} were obtained for *SG, CT*, and *C* samples, respectively. Moreover, according to the behaviour generally observed when using the oxide electrodes [29], decreasing values of q^* were measured as the potential scan rate was increased. The values observed for *SG* samples ranging from 65.9 mC cm^{-2} at 20 mV s^{-1} to 28 mC cm^{-2} at 100 mV s^{-1}, are in agreement with those generally reported in the literature for this kind of electrodes [29].

4.3.2.3 Steady-state polarisation analysis

In potentiostatic experiments the steady-state current density is a measure on the amount of active sites on the geometric surface area. The quasi-steady state current-potential data obtained in the *OER* region using the three metal oxide electrodes were recorded at a scan rate of 1 mV s^{-1} in 1.75 M-NaOH solution.

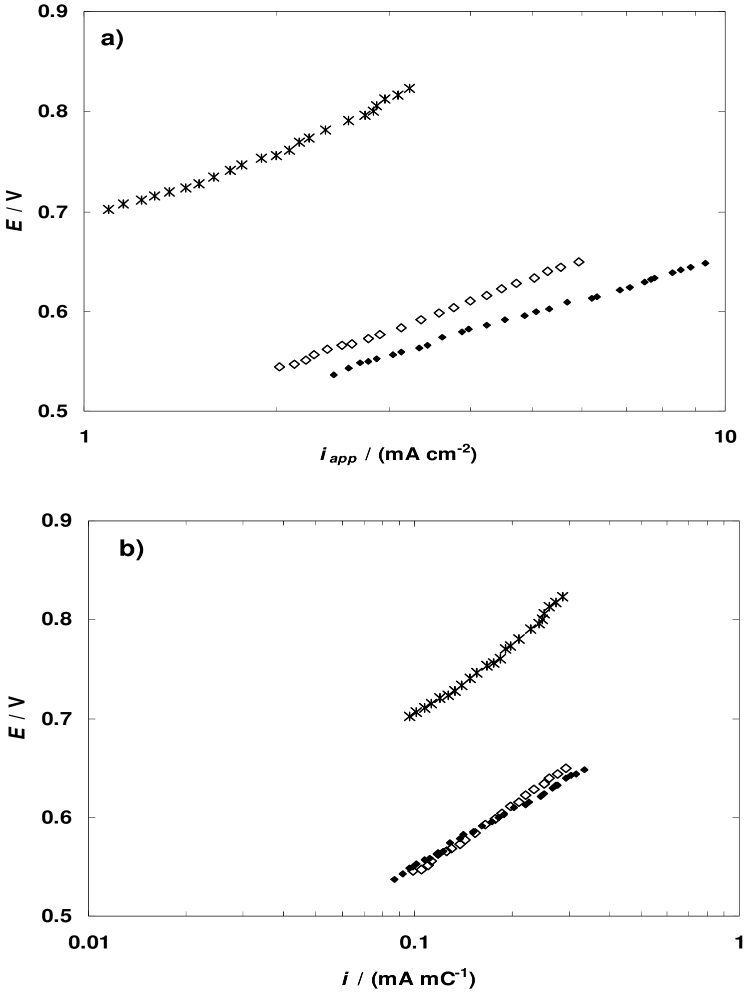

Figure 4.5. *Tafel plots at samples SG (♦),CT (◊) and C (*) measured in 1.75 M NaOH at 25°C. Current densities expressed with respect to the geometrical area (a) and normalised with respect to the voltammetric anodic charge (b).*

The values of apparent current density, expressed with respect to the electrode geometrical surface area, are shown in Fig. 4.5a while in Fig. 4.5b the current values were normalized with respect to the anodic charge derived from the cyclic voltammetry experiments. The overlapped normalized curves of *SG* and *CT* samples reveal that the different electrocatalytic activity of these samples observed in Fig. 5a was caused by the different sample morphology (different surface area of *SG* and *CT* samples). On the other hand, chemical nature of the active sites and the reaction mechanism seems to be the same for both *SG* and *CT* samples. The data, corrected for ohmic drops were used to calculate the Tafel slopes of similar electrodes. As a matter of comparison, Table 4.2 also reports values of Tafel coefficient and the corresponding preparation and experimental conditions derived from literature.

Ref	**Samples**	**Substr.**	**Preparation method**	**Electrol.**	**b / (mV dec^{-1}) low η - high η**
this work	SG	Ti	Sol-gel	NaOH 1.75M at 25°C	184
this work	CT	Ti	-	NaOH 1.75M at 25°C	229
this work	C	Ti	-	NaOH 1.75M at 25°C	256
Bocca et al.[58]	Co_3O_4	Ni	thermal decomposition	KOH 1M at 60°C	145
Bocca et al.[58]	teflon bonded Co_3O_4	Ni	thermal decomposition	KOH 1M at 60°C	189
Svelg et al.[11]	Co_3O_4	Pt and ITO/glass	Sol-gel	KOH 1 M at 23°C	55/60 -90/110
Rasiyah et al. [25]	teflon bonded Co_3O_4	-	freeze-drying	KOH medium at 25°C	60 - 120
Singh et al. [6]	Co_3O_4	Ni	sequential solution coating	KOH 1M at 25°C	53/55 – 130/183

Table 4.2. *Tafel slopes of thin Co_3O_4 films electrodes towards oxygen evolution.*

The polarization curves for most of the electrodes displayed two Tafel regions: one at low overpotentials and the other at high overpotentials. Rasiyah and Tseung [25] ascribed this behaviour to the transition to a higher valence state of cobalt ions in the lattice. In the case of electrodes showing only one Tafel slope it was supposed that even at low overpotential a high surface coverage by hydroxyl ions was achieved [58].

After this preliminary comparison, the results demonstrated that the lower catalytic activity of commercial samples may be connected to presence of CoO in their structure. A thermal treatment of the sample at 900°C induced the complete transformation of CoO into Co_3O_4, so that a appreciable increase of the activity is observed at thermal treated samples. However an increasing in the particle size of the active phase is also measured at the end of the treatment. If the behaviour of sol-gel samples is considered, a further increase in the activity is observed which, as revealed by the normalised Tafel curves, can be mainly correlated to a morphologic effects.

4.3.2.4 Morphology factor of the sol-gel Co_3O_4 electrodes

One of the most relevant issues in preparing powder electrodes is to guarantee that the favourable characteristics of the powder, such as high specific surface area and high porosity, are maintained also in the assembled electrodes. Thus, specific runs were performed, in order to verify the morphology of the assembled samples.

A review of the different methods proposed to determine the real surface area of solid electrodes was published by Trasatti and Petrii [59]. Moreover, Trasatti et al. [29, 60, 61] suggested that, in case of solid oxide electrodes, the determination of the porosity based on the dependence of the voltammetric charge (q^*) on the potential scan rate can be affected by spurious factors. Actually, it must be stressed that reliable q^* values are obtained only at intermediate ν values [62].

As ν is increased, q^* can be affected by the following factors:

a) uncompensated ohmic drops in the active layer as well as in the oxide/support interface,
b) distortion due to some irreversibility of the *SSSRT*,
c) "freezing" of the pores due to inhomogeneous potential distribution in the layer,
d) difficult response of hardly accessible surface regions.

At very low ν values chemical self-discharge might compete with electrochemical transformation and this may also affect the actual values of q^* [62]. Da Silva et al. [63] proposed another technique based on the dependence of the capacitive current (i_c) on the potential scan rate, measured from the voltammetric response in a short capacitive potential region of about 100 mV. Also in this case, the authors suggest particular attention in selecting the suitable value of potential at which i_c must be measured: especially at high ν values distortion of cyclic voltammetries near the switching potential could affect the validity of this procedure.

In the present work, cyclic voltammetries were performed at different potential scan rates ($20 \leq \nu \leq 300$ mV s^{-1}), in a small potential range (0.04 – 0.14 V), where the charge transfer reactions were practically absent at sol-gel Co_3O_4 samples. As suggested by the procedure [63], the value of i_c was measured at 0.12V, within the last 20% of the capacitive potential interval, where the almost constant current, registered even at high ν values, can be interpreted as a limited influence of the resistive components. The results are shown in Figure 4.6 in which i_c is depicted as a function of ν.

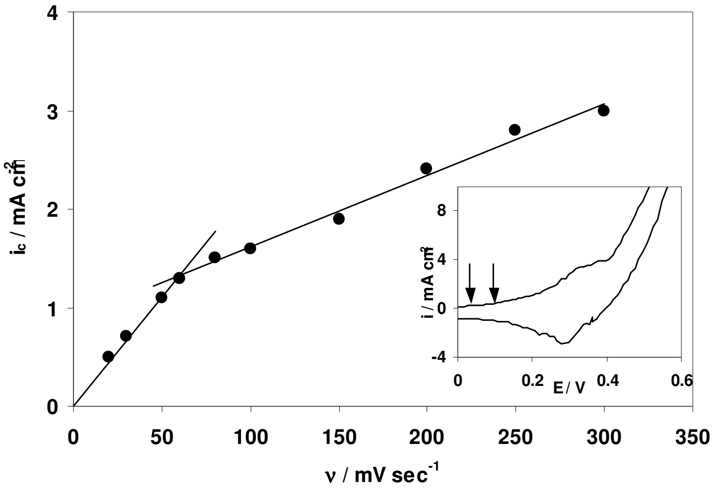

Figure 4.6. Dependence of the capacitive voltammetric current (i_c) on the scan rate (ν) at sol-gel Co_3O_4 electrode. Inset: cyclic voltammetry at sol-gel Co_3O_4 electrode; arrows show the potential interval used to record the voltammetric dependence on ν.

The differential capacity of oxide coating can be derived from the slope of the linear regression of the data. Actually, two different slopes were obtained form data in Fig. 4.6 which are related to the total (C_d) and the outer (C_{de}) differential capacities [63]. The change of the slope in the high potential scan rates can be attributed to the exclusion of surface areas located in the more difficult-to-access coating regions.

On these bases the morphology factor φ was evaluated by:

$$\varphi = \frac{C_{di}}{C_d} \tag{4.3}$$

where the inner differential capacity (C_{di}) was calculated as difference between the total and the outer capacities.

The values of C_d (22 mF cm^{-2}) and φ (0.67) calculated by this procedure, were in agreement with the results obtained by Da Silva et al. [63] which reported $C_d = 29$ mF cm^{-2} and $\varphi = 0.62$ for Ti/Co_3O_4 electrode prepared by thermal decomposition.

4.3.2.5 EIS analysis at sol-gel Co_3O_4 electrodes

Electrochemical impedance spectroscopy experiments were performed within a range of six decades of frequency from 100 kHz to 0.1Hz. The electrode/electrolyte interface and the corresponding surface processes were modelled by applying an equivalent electrical circuit approach. Although *EIS* technique is a useful tool to investigate the behaviour of the electrode surface, in the complex system considered in this work, in which different redox transitions of the material are possible, the identification of all the processes is difficult. In fact, it must be considered that in order to have well separated responses of distinct processes, a minimum ratio between the related time constants is required. In this context, attention was firstly paid on the results obtained at potentials lower than the oxygen evolution potential to investigate the capacitive response of the electrode material: *EIS* measurements were performed from 100 kHz to 1 Hz. The analysis was then addressed in the range of oxygen evolution potential, in order to obtain kinetic data of *OER*; measurements were in this case extended in a wider frequency range, down to 0.1 Hz, to better focus on the response of the electrode/solution interface.

EIS results at lower potential range – Figure 4.7 shows the trend of Nyquist and Bode diagrams obtained at different bias potentials in the range of frequency from 100 kHz to 1Hz. Some useful information can be derived from a qualitative analysis of the data in the figure: at least until oxygen evolution is not well developed, the data indicate the presence of two time constants. They are clearly indicated in Figure 4.7b which shows the Bode diagrams obtained at 0 V: two frequency-dependent linear zones can be individuated in the modulus Bode diagrams with different slopes, as well as strong changes in the corresponding phase Bode diagram which result in the presence of two capacitive/resistive elements in the corresponding equivalent circuit.

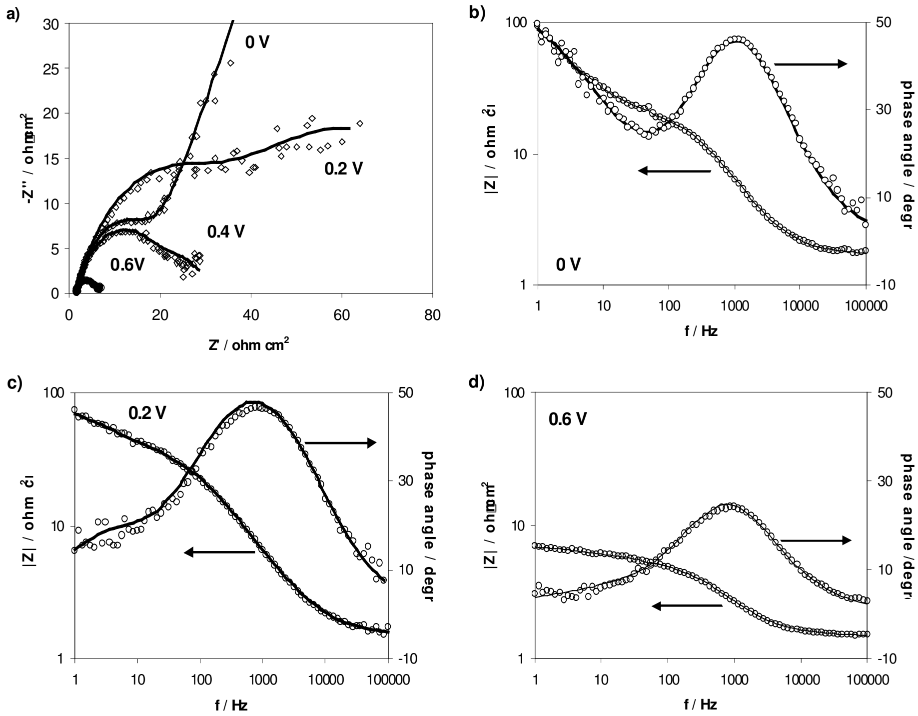

Figure 4.7. Experimental (o) and simulated (full lines) Nyquist plot (a), Bode modulus and phase angle plots at 0 V (b) 0.2 V (c) 0.6 V (d) of sol-gel Co_3O_4 electrode. Range of investigated frequency 100 kHz -1Hz.

As it can be seen in Fig. 4.7a, when the potential increases the loops in the Nyquist diagram, tend to interfere each other being they completely overlapped when potential reaches 0.6 V. Just one frequency-dependent segment is obtained in the absolute impedance at this potential, then a resistive behaviour is shown, in the lower-frequency region, with a trend almost independent of the frequency, and the phase angle value approaching zero degree (Fig. 4.7d).

Based on the experimental evidences, the data are interpreted by an electrical equivalent circuit composed of two capacitive/resistive elements in series (Fig. 4.8).

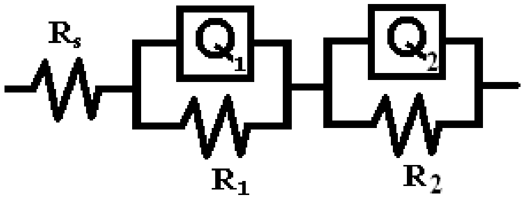

Figure 4.8. *Equivalent electrical circuit used to fit the experimental data of impedance spectra at lower potential range.*

Moreover, the fitting procedure showed that a better agreement between the experimental (o) and simulated (full lines) data was obtained if constant phase elements (*CPE*) were used instead of pure capacitors (*C*). Two parameters determine the impedance of the *CPE*:

$$Z_{CPE} = \frac{1}{Q(j\omega)^n} \tag{4.4}$$

Q which represents the frequency-independent parameter and *n* which represents the deviation from the ideal behaviour, being $n = 1$ for perfect capacitors.

The fitting parameters of the circuital elements are resumed in Table 4.3 in which R_s represents the ohmic drops, while R_1, Q_1 and R_2, Q_2 can be assumed as resistances and pseudocapacitances associated with the two *SSSRT* (Eq.s 4.1 and 4.2) individuated in the voltammetric analysis.

E V *vs* SCE	**R_s** Ω cm^2	**R_1** Ω cm^2	**Q_1** mS cm^{-2}s^n	**n_1**	**τ_1** s	**R_2** Ω cm^2	**Q_2** mS cm^{-2}s^n	**n_2**	**τ_2** s
0	1.7	18.87	0.12	0.82	6.1×10^{-4}	700	3.6	0.65	4.2
0.2	1.5	38.51	0.26	0.74	1.9×10^{-3}	57.3	4.9	0.62	1.3×10^{-1}
0.4	1.6	19.10	0.22	0.75	6.9×10^{-4}	13.91	23	0.45	8.2×10^{-2}
0.6	1.5	11.66	0.21	0.76	3.6×10^{-4}	3.64	0.78	0.76	4.6×10^{-4}

Table 4.3. *Values of the fitting parameters evaluated from the equivalent circuit at different potentials.* τ_1 *and* τ_2 *represent the calculated time constants.*

In order to confirm this assumption the trend of Q_1 and Q_2 versus potential can be considered. In fact, as reported by some authors [64, 65], when *SSSRT* are involved in the oxidative process, a maximum in the capacitance *vs* potential trend is generally observed at potential value which coincides with that of the peak related to the surface transition in the cyclic voltammetry. Other authors [66] report that when adsorption phenomena are involved, the additional charge on the surface results in a capacitance peak at a particular potential: this potential coincides with that of the peak in the cyclic voltammetry if adsorption of the species involved in the electrochemical process follows a Langmuir trend.

By comparing Fig. 4.4 with data in Table 4.3, it can be observed that the reciprocal position of the peaks in the voltammetry is compatible with the Q_1/E and Q_2/E trends, and that the maximum in the Q_1/E is more cathodic than that of Q_2/E trend. The circuital elements R_1, Q_1 can be therefore assumed to represent the response of the transition Co(II)/Co(III) (Eq. 4.1). The formation of high conductivity CoOOH phase [67, 68] in this step, could be the reason for the decreasing R_1 values which are obtained at potentials more anodic that 0.2 V in the *EIS* measurements (Table 4.3). On the same bases, the circuital elements R_2, Q_2 were associated to the transition Co(III)/Co(IV) (Equation 4.2).

The values of the time constants, τ_1 and τ_2, calculated from the relevant parameters ($\tau^n = QR$), at the different potential values are also reported in Table 4.3. As it can be observed τ_1 is always lower than τ_2 indicating that the transition Co(III)/Co(IV) can be assumed as controlling step in the whole oxidative process [54, 69]. Taking into account the results from the voltammetric analysis in which the charge transfer resulted a quasi – reversible step, the slowness of this transition can be attributed to the slow diffusion of OH^- in the pore solution. Also the values of n_2 quite far from unity could indicate the effect of a diffusive process in the porous structure.

EIS results at higher potential range – Figure 4.9 shows an example of the Nyquist diagrams obtained in the range of oxygen evolution potentials.

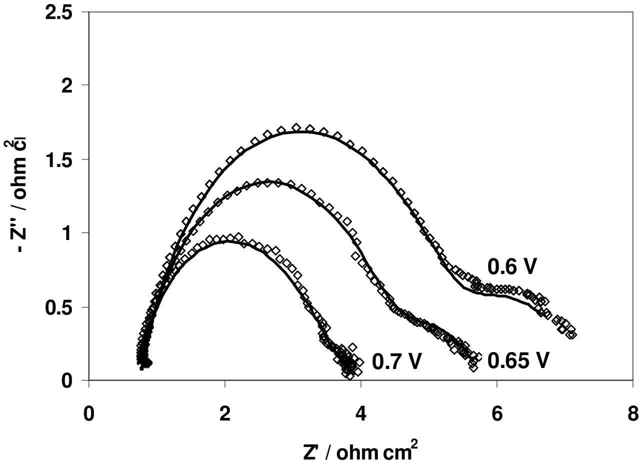

Figure 4.9. *Experimental (o) and simulated (full lines) Nyquist diagrams of sol-gel Co_3O_4 electrode at different potentials. Range of investigated frequency 100 kHz - 0.1Hz.*

The high frequency loop related to the response of the electrode material is still well evident at all the investigated potentials. The loop related to the response of the electrode/solution interface is also displayed being the frequency range extended down to 0.1 Hz. In this diagram the low-frequency cut off on the real axis, can be originated by the resistance to oxygen evolution which, in agreement with a charge transfer controlled process, depends on the potential: it exponentially decreases as the potential becomes more anodic.

The equivalent circuit of Figure 4.10 was used to interpret the *EIS* data, and the related parameters are reported in Table 4.4.

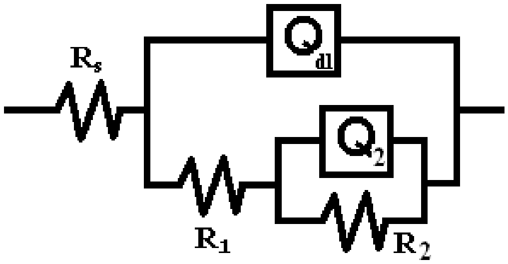

Figure 4.10. *Equivalent electrical circuit used to fit the experimental data of impedance spectra at higher potential range.*

From the distribution of the two time constants it may be concluded that the inner subcircuit with the higher time constant represents the slower process individuated in the previous section as limiting step of the electrode material response. The outer subcircuit is related to the fast charge/discharge process at the electrode/electrolyte interface, Q_{dl} being the double layer capacitance and R_1 the *OER* charge transfer resistance.

η V *vs* SCE	**R_1** Ω cm^2	**Q_{dl}** mS cm^{-2}s^n	**n_1**	**τ_1** s x10^4	**R_2** Ω cm^2	**Q_2** mS cm^{-2}s^n	**n_2**	**τ_2** s x10^2
0.2	4.63	0.29	0.80	2.31	1.82	90	0.61	5.15
0.22	3.62	0.29	0.79	1.87	1.77	130	0.52	3.83
0.25	2.95	0.32	0.80	1.65	1.41	100	0.48	2.7
0.27	2.72	0.24	0.80	1.01	0.77	120	0.68	3.03
0.3	2.17	0.19	0.85	1.04	1.77	80	0.39	0.67

Table 4.4. *Values of the fitting parameters evaluated from the equivalent circuit at different overpotentials. τ_1 and τ_2 represent the calculated time constants.*

The exponentially decreasing trend of R_1 with overpotential (η) was used to calculate the apparent current density (i) at the different overpotentials [70]:

$$R_1 = \frac{d\eta}{di} = \frac{RT}{nFi} \tag{4.5}$$

where R, T, n and F have the usual electrochemical meaning.

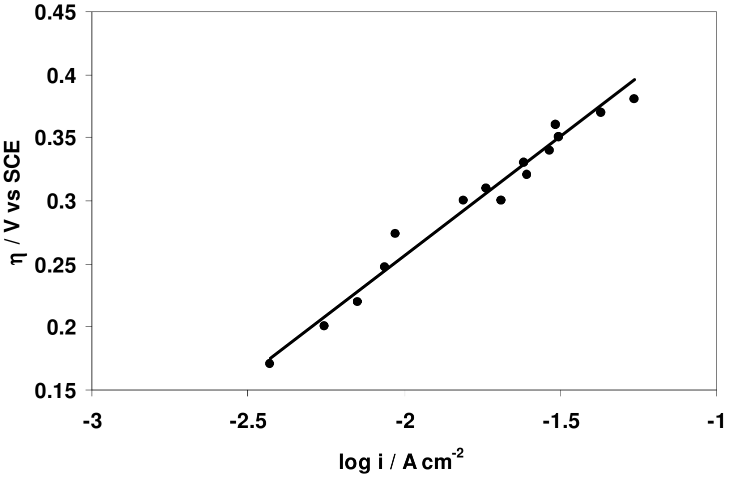

Figure 4.11. *Apparent current density (i) – overpotential (η) trend at Co_3O_4 electrode calculated from EIS data.*

The linear trend of the data (η *vs* log i) is illustrated in Fig. 4.11 from which the Tafel parameters were evaluated. In particular, a value of $b = 2.303\ RT/\alpha Fn = 189$ mV/dec can be calculated in the whole range of overpotential which agrees with the value calculated from the polarization experiments (Table 4.2).

The Tafel slopes reported in literature [6, 58] are often higher than 120 mV/dec, which is the b value theoretically calculated for one electron redox process, when the electron transfer coefficient α is equal to 0.5. This result was discussed and interpreted considering that the value of $\alpha = 0.5$ is only observed for an electron transfer process at a flat electrode surface in the absence of adsorption effects [71 - 73]. A recent paper appeared in the literature where these effects were lumped in a new parameter (α_{app}) [74]: values of α_{app} very different from 0.5 are reported depending on the electrode composition, the overpotential range and the nature of the electrolyte.

In the present case, a value of α_{app} = 0.3 is calculated from the experimental *b* value, which may be justified by the surface modifications due to the SSSRT which can affect the value of the Tafel slope, especially at the lower overpotential [74]. When the same analysis is limited to consider only the data obtained at higher overpotential a new value of the Tafel slope can be determined (*b* = 115 mV/dec) confirming that, as it was expected, in the higher range of overpotential the influence of these spurious effects is limited. The related value of i_o = 3x10^{-5} A/cm^2 is evaluated in the same range of potential.

4.3.2.6 Modeling of *OER* at sol-gel Co_3O_4 electrodes.

As reported above, different parallel series steps can be involved during *OER* and transitions between different oxidation states of the oxides can be involved which should complicate the mechanism. Cyclic voltammetry and quasi-stationary current-potential curves are generally used to characterize the electrochemical performance of oxide electrodes. However, further information derived from *EIS* can result very useful to complete and confirm the analysis of the system. In particular, *EIS* technique is a good tool to obtain specific information about mechanism and kinetics of the electrode reactions.

As reported in chapter 3, *EIS* is conducted by applying a small ac signal to perturb the electrode system while assuring the linearity between the output and the input signals. This pseudo-linearity makes it possible to treat the electrode system as a linear electrical circuit. For this reason the analysis of *EIS* data by equivalent electrical circuit method has been considered the major technique. However sophisticated approaches are required to interpret the data and extract meaningful results.

Alternatively, the impedance data for a given system can be interpreted by a mathematical model, based on a plausible microkinetic description of chemical reactions and diffusion steps involved in the process. In this approach, the kinetics of the individual reaction steps is expressed in the form of rate equations, and the theoretical impedance is derived.

The combined use of equivalent electrical circuit method and the mathematical modeling of the faradaic impedance can be capable of solving problems such as the uncertainty of the physical significant of the electrical parameters and the difficulty of quantitative fitting of the latter method [75].

The goal of this analysis is to accurately simulate the impedance spectra with a set of kinetics parameters extracted by the combined use of equivalent electrical circuit method and the mathematical modeling.

The procedure involves the following steps (Figure 4.12):

1. theoretical derivation of the Faradaic impedance which allows to define electrochemical parameters as function of the kinetic parameters $A\ (K_i,\ E)$ and $B\ (K_i,\ E)$
2. definition of a reaction model of oxygen evolution reaction at Ti/Co_3O_4 electrodes
3. derivation of a relationship between the electrochemical parameters and the electrical elements of equivalent electrical circuit $A\ (R,\ C\ )$ and $B\ (R,\ C)$
4. fitting of the experimental *EIS* data to obtain the equivalent electrical elements
5. extraction of the kinetic parameters from the comparison between results from steps 2 and 3
6. validation of the method by a comparison between the simulated results and the experimental data.

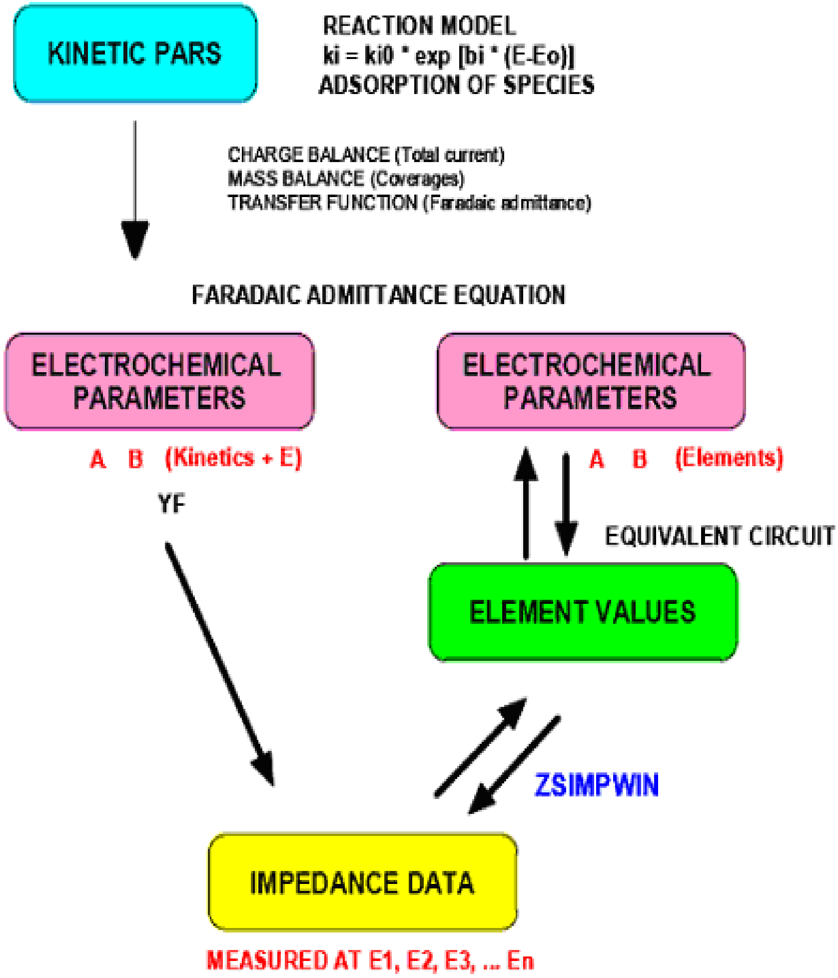

Figure 4.12. *Determination of kinetic parameters utilizing Faradaic admittance equation and corresponding equivalent circuit.*

Step 1 - Theoretical derivation of the Faradaic impedance – In order to obtain quantitative information about mechanism and kinetics of the oxygen evolution reaction, the analysis is made in a narrow potential range (0.7 to 0.78 V) in the *OER* region. As previously indicated, for these types of electrodes, it is probable that Co(IV) metal ions, are involved as intermediate states in the OER, together with OH species at the reaction interphase. So, by considering that the surface oxidation, previous to the *OER*, gives rise to Co(IV) surface states, the *OER* can proceed through the following simplified reaction scheme [13]:

$$\mathrm{Co(IV)_s + OH^- \leftrightarrow Co(IV)(OH)_{ad} + e^-} \tag{4.6}$$

$$\mathrm{Co(IV)(OH)_{ad} + OH^- \rightarrow Co(IV)_s + ½\, O_2 + H_2O + e^-} \tag{4.7}$$

On these bases, only one intermediate species is involved in the process, so that the faradaic current density i_F can be expressed as a function of the surface coverage of the intermediate ϑ, other than of the electrode potential E [76, 77]:

$$i_F = f\,(E,\ \vartheta) \tag{4.8}$$

where ϑ is the fractional surface coverage of the adsorbed species defined as:

$$\vartheta = \Gamma / \Gamma_{max} \tag{4.9}$$

being Γ the surface concentration of adsorbate intermediate and Γ_{max} the related saturation value, which can be considered constant in the narrow range of investigated potential.

If an adequately small perturbation signal is applied to the electrode system, the deviation of i_F from the steady state can be approximated by the first order of the Taylor's series expansion:

$$\Delta i_F = \left(\frac{\partial I_F}{\partial E}\right)_{SS} \Delta E + \left(\frac{\partial I_F}{\partial \vartheta}\right)_{SS} \Delta \vartheta \tag{4.10}$$

where Δ is a very small a.c. signal and the subscript "ss" stands for steady-state conditions.

The ratio $\Delta i_F/\Delta E$ represents the Faradaic admittance (the inverse of the Faradaic impedance):

$$Y_F = \frac{1}{Z_F} = \frac{\Delta i_F}{\Delta E} = \left(\frac{\partial i_F}{\partial E}\right)_{SS} + \left(\frac{\partial i_F}{\partial \vartheta}\right)_{SS} \frac{\Delta \vartheta}{\Delta E} \tag{4.11}$$

To obtain the expression for $\Delta\vartheta/\Delta E$ we consider the change rate of production of adsorbed species, which is also a function of E and ϑ:

$$\dot{\vartheta} = \frac{d\vartheta}{dt} \tag{4.12}$$

Under the conditions of an impedance experiment, ϑ is the sum of a d.c. part ϑ_{dc} and an a.c. part $\Delta\vartheta = |\Delta\vartheta| \exp(j\omega t + \phi)$, whose amplitude is $|\Delta\vartheta|$ and whose phase (relative to the a.c. potential) is ϕ.

A.c. and d.c. parts of Eq. 4.12 may be separated, and by taking the linear approximation of Taylor's series expansion around the steady state, we can get:

$$\frac{d\vartheta_{dc}}{dt} + \frac{d(\Delta\vartheta)}{dt} = \frac{d\vartheta_{dc}}{dt} + j\omega\Delta\vartheta \tag{4.13}$$

Now, because the system is in steady-state without the a.c. perturbation, the d.c. terms must equal:

$$\frac{d(\Delta\vartheta)}{dt} = j\omega\Delta\vartheta \tag{4.14}$$

so, at steady-state, we can write:

$$\dot{\vartheta} = j\omega\Delta\vartheta = \left(\frac{\partial\dot{\vartheta}}{\partial E}\right)_{SS} \Delta E + \left(\frac{\partial\dot{\vartheta}}{\partial\vartheta}\right)_{SS} \Delta\vartheta \tag{4.15}$$

and the following expression for $\Delta\vartheta/\Delta E$ can be derived:

$$\frac{\Delta\vartheta}{\Delta E} = \frac{\left(\dfrac{\partial\dot{\vartheta}}{\partial E}\right)_{SS}}{j\omega - \left(\dfrac{\partial\dot{\vartheta}}{\partial\vartheta}\right)_{SS}} \tag{4.16}$$

So, we can get:

$$Y_F = \frac{1}{Z_F} = \frac{\Delta i_F}{\Delta E} = \left(\frac{\partial i_F}{\partial E}\right)_{SS} + \frac{\left(\frac{\partial i_F}{\partial \vartheta}\right)_{SS}\left(\frac{\partial \dot{\vartheta}}{\partial E}\right)_{SS}}{j\omega - \left(\frac{\partial \dot{\vartheta}}{\partial \vartheta}\right)_{SS}} \tag{4.17}$$

where the following parameters can be defined:

$$\frac{1}{R_{ct}} = \left(\frac{\partial i_F}{\partial E}\right)_{SS} \tag{4.18}$$

$$A = \left(\frac{\partial i_F}{\partial \vartheta}\right)_{SS}\left(\frac{\partial \dot{\vartheta}}{\partial E}\right)_{SS} \tag{4.19}$$

$$B = -\left(\frac{\partial \dot{\vartheta}}{\partial \vartheta}\right)_{SS} \tag{4.20}$$

R_{ct} is the chare transfer resistance, and A and B are defined as electrochemical parameters. On these bases the Faradaic admittance can be written as:

$$Y_F = \frac{1}{Z_F} = \frac{1}{R_{ct}} + \frac{A}{j\omega + B} \tag{4.21}$$

Step 2 - Reaction model of *OER* at sol- gel Co_3O_4 electrodes - The reaction model must be considered to calculate i_F and $\dot{\vartheta}$, which are needed to determine the electrochemical parameters in Eq.s 4.18 – 4.20. To this aim, assuming that the adsorption/desorption of the intermediate species Co(IV)(OH)$_{ad}$ follows a Langmuir-type isotherm, the rate of the Reactions 4.6 and 4.7 can be as:

$$v_1 = k_1[OH^-](1 - \vartheta) - k_{-1}\vartheta \tag{4.22}$$

$$v_2 = k_2\vartheta[OH^-] \tag{4.23}$$

where $k_{\pm i}$ are the rate constants of direct and forward reactions, which are exponentially dependent on p he electrode potential E:

$$k_i = k^o_i \exp(b_i E) \tag{4.24}$$

where k^o_i is the rate constant at $E = 0$ V and b_i is the Tafel constant (V^{-1}).

By considering the net rate of production of electrons r_e:

$$r_e = v_1 + v_2 = i_F / F \tag{4.25}$$

the faradaic current density i_F can be written as:

$$i_F = F(k_1[OH^-](1 - \vartheta) - k_{-1}\vartheta + k_2\vartheta[OH^-]) \tag{4.26}$$

while a mass balance of the intermediate species Co(IV)(OH)$_{ad}$ allows to express $\dot{\vartheta}$:

$$\Gamma_{\max}\dot{\vartheta} = v_1 - v_2 = k_1\left[OH^-\right](1-\vartheta) - k_{-1}\vartheta - k_2\vartheta\left[OH^-\right] \tag{4.27}$$

In order to derive the value of the parameter Γ_{max} the voltammetric results obtained were used. Actually, in accordance with Nikolov et al. [69], the voltammetric charge q_a, involved in the anodic peaks recorded previous to the oxygen evolution potential, can be used to evaluate Γ_{max} as:

$$\Gamma_{max} = q_a/F \tag{4.28}$$

where F is the Faraday constant.

So, the electrochemical parameters can expressed as functions of the kinetic parameters using Eq.s. (4.22) and (4.23).

$$R_{ct} = \frac{1}{F\vartheta_{ss}\left(\left(k_3[OH^-] + k_{-2}\right)b_2 - k_{-2}b_{-2} + k_3[OH^-]b_3\right)} \tag{4.29}$$

$$A = \frac{F\vartheta_{ss}}{\Gamma_{\max}}\left(-k_1[OH^-] - k_{-1} + k_2[OH^-]\right)\left[\left(k_2[OH^-] + k_{-1}\right)b_1 - k_{-1}b_{-1} - k_2[OH^-]b_2\right] \tag{4.30}$$

$$B = \frac{1}{\Gamma_{\max}}\left(k_2[OH^-] + k_{-2} + k_3\left[OH^-\right]\right) \tag{4.31}$$

where ϑ_{ss} represents the fractional surface coverage evaluated (from Eq. 4.27) at steady-state conditions:

$$\theta_{ss} = \frac{k_2[OH^-]}{k_2[OH^-] + k_{-2} + k_3[OH^-]} \tag{4.32}$$

Step 3 - Derivation of a relationship between the electrochemical parameters and the electrical elements of equivalent electrical circuit - The electrochemical parameters *A* and *B* can be expressed as functions of the equivalent electrical elements. To this aim, Wu et al. [78] have published general equivalent circuits for the faradaic electrode process involving n state variables. According to their work, mathematical expression of the faradaic impedance can be written as:

$$Z_F = R_{ct} + \sum_{i=1}^{n} \frac{R_i}{1 + j\omega R_i C_i} \qquad (4.33)$$

The relationship between electrical elements in the equivalent circuit and the electrochemical parameters in the faradaic admittance expression can be established by comparing the Equation 4.33 with the derived faradaic admittance expression (Eq. 4.21). Accordingly, the electrochemical parameters can expressed as functions of the electrical elements:

$$A = -\frac{1}{{R_{ct}}^2 C_1} \qquad (4.34)$$

$$B = \frac{1}{C_1}\left(\frac{1}{R_1} + \frac{1}{R_{ct}}\right) \qquad (4.35)$$

An equivalent circuit corresponding to the faradaic admittance equation serves as an essential tool to determine the electrochemical parameters (*A* and *B*) from the impedance data. As it is well established, a general equivalent circuit for the Faradaic electrode process involving one state variable can be represented as in Figure 4.13.

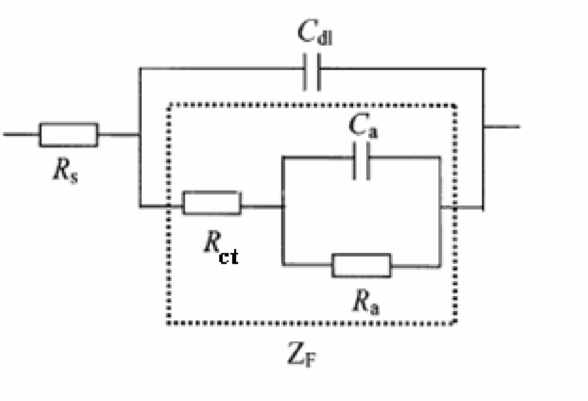

Figure 4.13. *Equivalent electrical circuit used to fit the experimental data of impedance spectra during OER*

Thus, assuming that the diffusion effect can be neglected, the total impedance of the electrode process can be expressed by the following equation:

$$Z_{tot} = R_s + \frac{1}{Y_F + j\omega C_{dl}} \tag{4.36}$$

where C_{dl} is the double-layer capacitance, and R_s the uncompensated ohmic drops.

Step 4 - Fitting of the experimental *EIS* data to obtain the equivalent electrical elements - As reported above, in order to obtain information about the mechanism of *OER*, impedance measurements were specifically performed within the potential range $0.7 < E < 0.78$ *V*. In this potential range the electric circuit in Figure 4.13 was able to interpret well the experimental data: as an example, Figure 4.14 shows some examples of the experimental data and the patterns simulated with this model circuit.

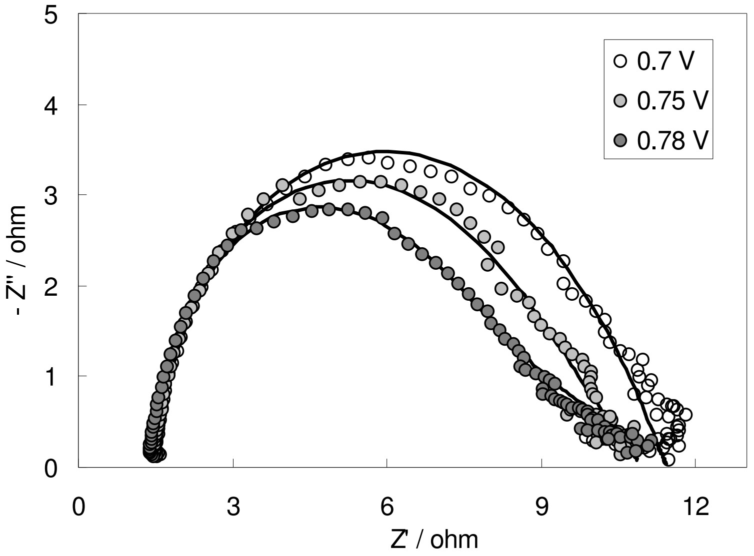

Figure 4.14. *Experimental (circles) and calculated (full lines) impedance plot simulated by the equivalent circuit shown in Figure 4.13 of sol-gel* Co_3O_4 *electrode at different potential. Range of investigated frequency 100 kHz - 0.1Hz.*

The values of circuital parameters calculated by fitting the experimental data obtained at different potentials are listed in Table 4.5.

E V *vs* SCE	**R_Ω** Ω cm^2	**R_{ct}** Ω cm^2	**Q_{dl}** mS cm^{-2}s^n	**n**	**R_1** Ω cm^2	**C_1** S cm^{-2}s^n
0.7	0.43	1.25	6.50	0.27	9.89	1.68E-05
0.71	0.68	1.02	3.60	0.33	9.54	1.72E-05
0.72	0.68	1.04	2.70	0.35	9.38	1.74E-05
0.73	0.65	1.06	2.90	0.34	9.70	1.69E-05
0.74	0.82	0.88	2.40	0.38	9.58	1.65E-05
0.75	0.88	0.82	1.64	0.42	9.27	1.64E-05
0.76	0.88	0.84	2.50	0.38	9.98	1.57E-05
0.77	1.60	0.6	8.50	0.50	9.5	1.54E-05
0.78	1.22	0.47	5.40	0.57	9.82	1.30E-05

Table 4.5. *Values of the fitting parameters evaluated from the equivalent circuit shown in Figure 4.13 at different potentials in the OER region. Chi-square values (χ^2) $\leq 10^{-4}$ were obtained in all cases.*

Steps 5 and 6 - Extraction of the kinetic parameters from the electrochemical parameters and validation of the method - On the bases of Eq.s 4.34-4.35 the electrochemical parameters *A* and *B* can be evaluated at various potentials using data in Table 4.5. Finally, the system of Eq.s 4.29-4.31 along with Eq. 4.32 can be solved to evaluate ϑ and k_i values. Taking into account the dependence of k_i vs *E* (Eq. 4.24), the corresponding kinetic parameters ($k°_1$, $k°_{-1}$, $k°_2$, b_1, b_{-1}, b_2) for the Reactions 4.6 and 4.7 were obtained from slope and intercept of the plots *ln* k_i vs *E,* an example of which is shown in Figure 4.15 for data related to k_1.

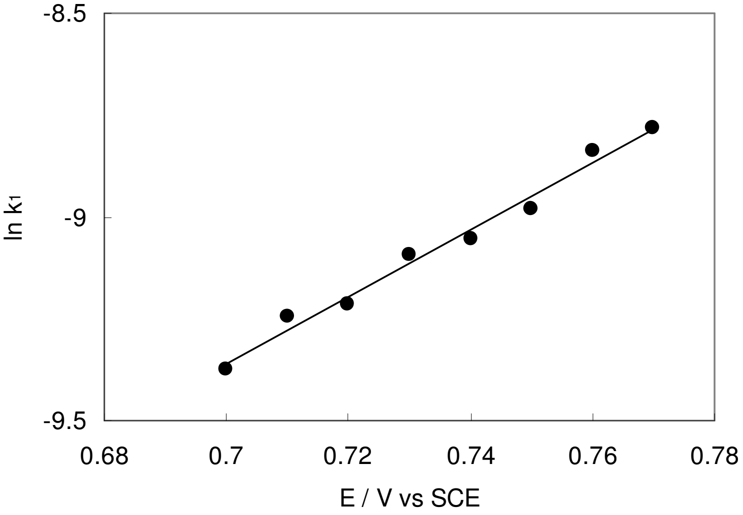

Figure 4.15. *Dependence of the calculated values of ln k_1 on the electrode potential E.*

The complete set of the extracted kinetic parameters is summarized in Table 4.6.

$k°_1$ / cm s^{-1}	3 x 10^{-7}
$k°_{-1}$ / moli cm^{-2} s^{-1}	2 x 10^{-6}
$k°_2$ / cm s^{-1}	2 x 10^{-5}
b_1 / mV dec^{-1}	277.0
b_{-1} / mV dec^{-1}	-213.0
b_2 / mV dec^{-1}	125.0

Table 4.6. *Calculated values of the kinetic parameters of OER at sol- gel Co_3O_4 electrodes. Kinetic constants are expressed per unit area.*

In the investigated potential range a value of ϑ, always much lower than 1 is calculated from the model (Eq.4.32) (Figure 4.16).

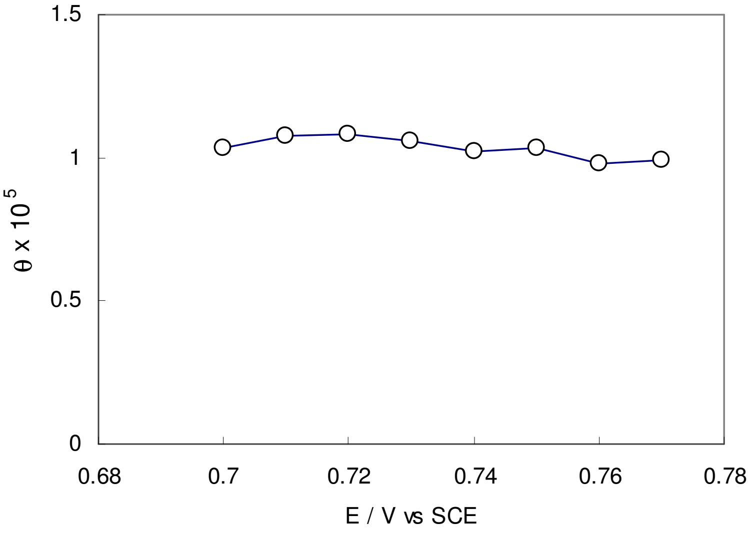

Figure 4.16. *Potential dependence of calculated values of the fractional coverage of the adsorbed species ϑ.*

In these conditions the following expression can be written for the faradaic current density at the steady state:

$$i_{F\,SS} = \frac{2Fk_1^0 k_2^0 \left[OH^-\right]^2}{k_{-1}^0} \exp\left[(b_1 + b_2 - b_{-1})E_{SS}\right] \qquad (4.37)$$

from which a corresponding Tafel slope of 189 mV dec^{-1} can be derived which agrees with the value calculated from the polarization experiments and the impedance analysis.

To verify the reliability of the approach, the theoretical *EIS* patterns were re-calculated from the extracted kinetic parameters and compared with the experimental data. An example of the quantitative consistency between the experimental and simulated data can be seen in Figure 4.17, which indicates that the acquisition of kinetic parameters by this approach can be considered precise and valid.

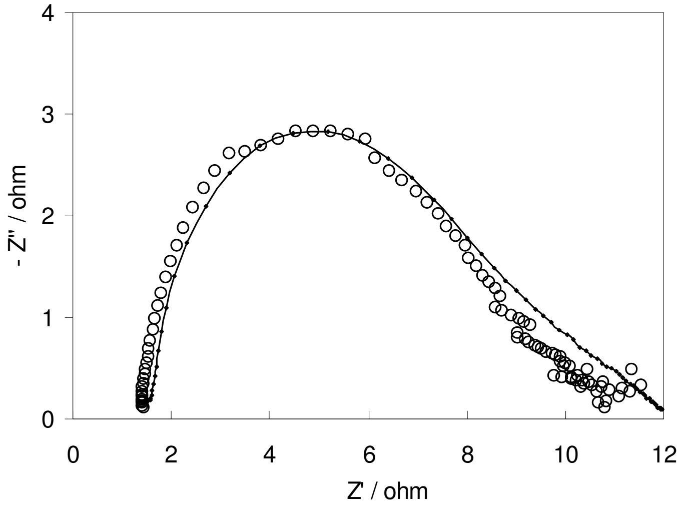

Figure 4.17. *Experimental (circles) and calculated (dotted lines) impedance plot based on the extracted kinetic parameters of sol-gel* Co_3O_4 *electrode at 0.78 V. Range of investigated frequency 100 kHz - 0.1Hz.*

4.4 Conclusions

The behaviour of the spinel-type Ti/Co_3O_4 electrodes obtained by a sol-gel route was examined in alkaline solution during oxidative process at different potentials. The results indicated that different redox transitions are possible during the oxidative process leading to Co(III) and Co(IV) containing phases which constituted specific sites for OH- adsorption. The results also confirmed that Co(IV) containing species are the catalytic sites for *OER*. Moreover, the time constants evaluated from *EIS* measurements at different potentials allowed to individuate the transformation Co(III)/Co(IV) as the slowest step in the oxidative process.

The combination of the equivalent circuit approach with the mathematical modelling of the faradaic impedance was used to derive the kinetic parameters for OER at this electrode. A quantitative fitting of the experimental data was performed and an exact physical meaning was maintained for every parameter of the model. The method gave optimum results which were in agreement with data previously obtained from polarization experiments and impedance analysis.

These electrodes can be considered as a very attractive anode material for oxygen generation in alkaline media. However, their catalytic activity and stability can be still increased. One possibility to achieve this goal would be the introduction of an other component in the layer. So, the study will be extended to mixed spinel oxide electrodes.

4.5 References

[1] H. Wendt, V. Plzak, Electrochim. Acta 28 (1988) 27

[2] L.A. De Faria, M. Prestat, J.F. Koenig, P. Chartier, S. Trasatti, Electrochim. Acta 44 (1998) 1481

[3] R. Boggio, A. Carugati, S. Trasatti, J. Appl. Electrochem. 17 (1987) 828

[4] R.N. Singh, M. Hamdani, J.F. Koenig, G. Poillerat, J.L. Gautier, P. Chartier, J. Appl. Electrochem. 20 (1990) 442

[5] R.N. Singh, J.P Pandey, N.K. Singh, B. Lal, P. Chartier, J.F. Koenig, Electrochim. Acta 45 (2000) 1911

[6] S.P. Singh, S. Samuel, S.K. Tiwari, R.N. Singh, Int. J. Hydrog. Energy 21 (1996) 171

[7] B.E. Conway, in S. Trasatti (Ed.) Electrodes of Conductive Metallic Oxides, Part B Elsevier, Amsterdam, 1981, 433

[8] E.J.M. O'Sullivan, E.J. Calvo, in R.G. Compton (Ed.) Comprehensive Chemical Kinetics 27, Elsevier, Amsterdam, 1987, 274

[9] B.E. Conway, T.C. Liu, Ber. Bunsenges. Phys. Chem. 91(1987) 461

[10] L.G. Tejuca, J.L.F. Fierro, J.M. Tascon, Advances in Catalysis 36, Academic Press, New York, 1989

[11] F. Svegl, B. Orel, I. Grabec-Svegl, V. Kaucic, Electrochim. Acta 45 (2000) 4359

[12] N.K. Singh, J.P. Singh, R.N. Singh, Int. J. Hydrogen Energy 27 (2002) 895

[13] E.B. Castro, C.A. Gervasi, Int. J. Hydrogen Energy 25 (2000) 1163

[14] C. Iwakura, A. Honji, H. Tamura, Electrochim. Acta 26 (1981) 1319

[15] R.N. Singh, J. F. Koenig, G. Poillerat, P. Chartier, J. Electroanal. Chem. 370 (1991) 241

[16] S. Trasatti, Electrochim. Acta 36 (1991) 225

[17] P. Nkeng, J.F. Koenig, J.L. Gautier, P. Chartier, G. Poillerat, J. Electroanal. Chem. 402 (1996) 81

[18] L.M. Da Silva, J.F.C. Boodts, L.A. De Faria, Electrochim. Acta 45 (2000) 2719

[19] L.M. DaSilva, J.F.C. Boodts, L.A. De Faria, Electrochim. Acta 46 (2001) 1369

[20] V.V. Shalaginov, D.M. Shub, N.V. Kozlova, V.N. Lomova, Elektrokhimiya 19 (1983) 537

[21] S. Kulandaisamy, J.P. Rethinaraj, S.C. Chockalingam, K.V. Venkateswaran, S. Visvanathan, Electrochim. Acta 45 (2000) 3047

[22] M. Hamdani, J.F. Koening, P. Chartier, J. Appl. Electrochem. 18 (1988) 568

[23] A. A. Addi, J. Douch, M. Hamdani, Bull. Electrochem. 15 (1999) 556

[24] R.N. Singh, J.F. Koenig, G. Poillerat, P. Chartier, J. Electrochem. Soc. 137 (1990) 1408

[25] P. Rasiyah, A.C.C. Tseung, J. Electrochem. Soc. 130 (1983) 365

[26] L.C. Schumacher, I. B. Holzhueter, I.R. Hill, M.J. Dignam, Electrochim. Acta 35 (1990) 975

[27] W. Estrada, M.C.A. Fantini, S.C. Castro, C.N.P. Fonseca, A. Gorenstein, J. Appl. Phys. 74 (1993) 5835

[28] I. Serebrennikova, V.I. Birss, J. Electrochem. Soc. 144 (1997) 566

[29] G. Spinolo, S. Ardizzone, S. Trasatti, J. Electroanal. Chem. 423 (1997) 49

[30] C. Pirovano, S. Trasatti, J. Electroanal. Chem. 180 (1984) 171

[31] F. Svegl, B. Orel, M.G. Hutchins, K. Kalcher, J. Electrochem. Soc. 143 (1996) 1532

[32] L. D. Burke, M. M. McCarthy, J. Electrochem. Soc. 135 (1998) 1175

[33] T. Yoshino, N. Baba, Sol. Energy Mater. Sol. Cells, 39 (1995) 391

[34] E.B. Castro, C.A. Gervasi, J. R. Vilche, J. Appl. Electrochem. 28 (1998) 835

[35] A. Dierstein, H. Natter, F. Meyer, H.O. Stephan, C. Kropf, R. Hempelmann, Scr. Mater. 44 (2001) 2209

[36] S. Cattarin, P. Guerriero, M. Musiani, Electrochim. Acta 46 (2001) 4229

[37] K. Nakaoka, M. Nakayama, K. Ogura, J. Electrochem. Soc. 149 (2002) C159

[38] I.G. Casella, J. Electroanal. Chem. 520 (2002) 119

[39] M. Ito, Y. Murakami, H. Kaji, H. Ohkawauchi, K. Yahikozawa, Y. Takasu, Electrochem. Soc. 141 (1994) 1243

[40] Y. Takasu, S. Onove, K. Kameyama, Y. Murakami, K. Yahikozawa, Electrochim. Acta 39 (1994) 91

[41] J.L. Martin, S.E. Vilades, O. Gracia-Martinez, E. Vila, R.N. Rojas, M.J. Torralvo, Mater. Res. Bull. 28 (1993) 1135

[42] M. El Baydi, G. Poillerat, J.L. Rehspringer, J.L. Gautier, J.F. Koening, P. Chartier, J. Solid State Chem. 109 (1994) 281

[43] O. Lev, Z. Wu, S. Bhatathi, V. Glezer, A. Modestov, J. Gun, L. Rabinovich, S. Sampath, Chem. Mater. 9 (1997) 2354

[44] S. Alber, J.A. Cox, Mikrochim. Acta 127 (1997) 131

[45] A. Walcarius, Electroanalysis 10 (1998) 1217

[46] J. Wang, Anal. Chim. Acta 399 (1999) 21

[47] C. Cannas, G. Concas, D. Gatteschi, A. Falqui, A. Musinu, G. Piccaluga, C. Sangregorio G. Spano, Phys. Chem. 3 (2001) 838

[48] C. Cannas, G. Concas, D. Gatteschi, A. Musinu, G. Piccaluga and C. Sangregorio, J. Mat. Chem. 12 (2002) 3141

[49] Z. Yue, L. Li, J. Zhou, H. Zhang, Z. Gui, Mater.Sci.Eng. B64 (1999) 68

[50] C. Cannas, A. Musinu, D. Peddis, G. Piccaluga, J. Nanoparticle Res. 6 (2004) 223

[51] K. Alexander, X-Ray Diffraction Procedures, J. Wiley and Sons Inc., New York, 1962

[52] I.G. Casella, M. Gatta, J. Electroanal. Chem. 534 (2002) 31

[53] M. Filoche, B. Sapoval, Electrochim. Acta 46 (2000) 213

[54] C. Bocca, A. Barbucci, M. Delucchi, G. Cerisola, Int. J. Hydrogen Energy 23 (1998) 1

[55] S. Trasatti, in: J. Lipkowski, P.N. Ross (Eds.), Electrochemistry of Novel Materials, VHC, New York, 1994, 207

[56] S.Trasatti, G. Buzzanca, J. Electroanal. Chem. 29 (1971) App. 1

[57] L.D. Burke, O.J. Murphy, J. Electroanal. Chem. 96 (1979) 19

[58] C. Bocca, G. Cerisola, E. Magnone, A. Barbucci, Int. J. Hydrogen Energy 24 (1999) 699

[59] S. Trasatti, O.A. Petrii, J. Electroanal. Chem. 327 (1992) 353

[60] C.P. De Pauli, S. Trasatti, J. Electroanal. Chem. 396 (1995) 161

[61] N. Krstajic, S. Trasatti, J. Electrochem. Soc. 142 (1995) 2675

[62] D. Baronetto, N. Krstajic, S. Trasatti, Electrochim. Acta 39 (1994) 2359

[63] L.M. Da Silva, L.A. De Faria, J.F.C. Boodts, Electrochim. Acta 47 (2001) 395

[64] T.A.F. Lassali, J.F.C. Boodts, L.O.S. Bulhoes, Electrochim. Acta 44 (1999) 4203

[65] L.A. Da Silva, V.A. Alves, M.A.P. Da Silva, S. Trasatti, J.F.C. Boodts, Electrochim. Acta 42 (1997) 271

[66] A. Lasia, in: B.E. Conway and R.E. White (Eds.), Modern Aspect of Electrochemistry, vol.35, New York , 2002, p.1

[67] F. Lichetemberg, K. Kleinsorgen, J. of Power Sources 62 (1996) 207

[68] I.G. Casella, M.R. Guascito, Electrochim. Acta 45 (1999) 1113

[69] I. Nikolov, R. Darkaoui, E. Zhecheva, R. Stoyanova, N. Dimitrov, T. Vitanov, J. Electroanal. Chem. 429 (1997) 157

[70] E. Siebert, A. Hammouche, M. Kleitz, Electrochim. Acta 40 (1995) 1741

[71] L.M. Da Silva, J.F.C. Boodts, L.A. De Faria, J. Braz. Chem. Soc. 14 (2003) 388

[72] L.M. Da Silva, L.A. De Faria, J.F.C. Boodts, Electrochim. Acta 48 (2003) 699

[73] L.M. Da Silva, D.V. Franco, L.A. De Faria, J.F.C. Boodts, Electrochim. Acta 49 (2004) 3977

[74] K.C. Fernandes, L.M. Da Silva, J.F.C. Boodts, L.A. De Faria, Electrochim. Acta 51 (2006) 2809

[75] J.M. Hu, J.Q. Zhang, C.N. Cao, I. M. Hsing, Electrochim. Acta 49 (2004) 5227

[76] C.N. Cao, Electrochim. Acta 35 (1990) 831

[77] C.N. Cao, Electrochim. Acta 35 (1990) 837

[78] X. Wu, H. Ma, S. Chen, Z. Xu, A.Sui, J. Electrochem. Soc. 146 (1998) 1847

Chapter 5

Active electrodes in acid media: Sn-Ru oxide electrodes

5.1 Introduction

Oxygen evolution in acid environment represents a very severe test for electrocatalysts. Only precious metal oxides are relatively stable, however, the application of these coatings is strongly restricted by high costs and limited electrode lifetime. Consequently composite materials, where the precious compound is dispersed in a less active but more stable matrix, are being intensively studied to offer less expensive electrodes which might show good electrocatalytic activity, stability toward anodic dissolution and electronic conductivity. For example, RuO_2-SnO_2 [1-5], IrO_2-SnO_2 [6-7], RuO_2-TiO_2-SnO_2 [8-11], IrO_2-RuO_2-SnO_2 [12] and IrO_2-TiO_2-SnO_2 [13] systems are often adopted to improve the electrode performances for oxygen evolution in acid media. In these cases the use of SnO_2 represents the search for a compromise between electrocatalytic activity, long-term electrode stability and cost. It is a relatively cheap oxide capable of stabilizing the electrode and partly producing catalytic effects. So many researchers activities are oriented toward preparing coatings containing high level of SnO_2, and in recent years, to utilize SnO_2 as the main additive to the coatings or to obtain SnO_2-based active coatings is still one of the most studied topics [14-15].

Different methods have been developed for tin oxide preparation, including sol-gel processing [16-18], spray pyrolysis [19], chemical vapour deposition [20,21], sputtering [22-24] and numerous others. Mechanical processing is an alternative method for the production of mixed oxides. As reported in literature [25, 26], the mechanical processing of powders in ball mills is a simple technique to carry out thermodynamically unfavoured reactions and destabilize equilibrium compounds. Metastable phases such as amorphous alloys and nanostructured systems can be easily produced as a consequence of the far-from-equilibrium processing conditions [26]. These determine the excitation of unusual states of reactivity *via* the application of mechanical forces and the consequent transfer of mechanical energy [26-29]. The transfer of energy to powders takes place at impact events in which a relatively small fraction of the total powder charge is trapped between colliding surfaces [30]. Repeatedly involved in collisions, powder particles undergo coldwelding, fracturing and plastic deformation processes [30, 31]. Whereas the former induce a variation of number and morphology of powder particles [31], local deformation processes result in a decrease in the average crystallite size and accumulation of lattice disorder [30]. The gradual modification of microstructure, with formation of grain boundaries and successive refinement of coherent crystalline domains down to the nanometer range can, in turn, promote phase transitions and chemical transformations as well as significant changes of physical properties [26-31]. At microscopic level, the apparent simplicity of the mechanical treatment is replaced by a remarkable complexity originating from intertwined atomistic processes still awaiting a satisfactory description and rationalization [32-39]. For example, the intimate nature of the local excited states appearing in solid phases as a result of applied mechanical forces is still debated [32-39]. A comprehensive conceptual approach to transformation kinetics is still lacking even though any progress in such a direction could open the door, not only to a deeper understanding of atomistic processes, but also to practical applications [26-31].

So, the SnO_2-based electrodes prepared in the present work have been used to obtain information on the electrochemical properties of mechanically-processed powders and, in turn, on the modification of their chemical reactivity as a consequence of the accumulation of lattice defects. The electrodes were obtained by assembling SnO_2 and SnO_2-RuO_2 mixed oxide powders, mechanically processed for different times, on boron doped diamond supports. Among the other important aspects of electrocatalysis, it is well known the importance of catalyst support for the oxygen electrodes. Typically, the support should provide good electronic conductivity, proper physical surface necessary for achieving high surface area as well as porous structure. The support commonly used for electrochemical characterization of nanoparticles are subject to corrosion (graphite and glassy carbon) or oxide formation (titanium and gold substrates). These phenomena can modify the intrinsic response of the supported particles, so that an inert substrate is needed. In the last years, particular attention has been paid to the boron doped diamond. *BDD* has been chosen in the light of its chemical inertness, very low background current and large potential difference between hydrogen and oxygen evolution and an extreme resistance to chemical and electrochemical attacks [40]. Its outstanding properties also make it an attractive substrate for electrochemical characterization of supported electrocatalytic nanoparticles [41-43], avoiding the problems encountered with other common substrates. As reported in literature, diamond substrates have thus been used as support for the deposition of various metallic particles including mercury and silver [44], lead dioxide [45], titanium dioxide [46], ruthenium oxides [47-49], iridium oxide [50], hydrous iron oxide [51], gold [52,53] platinum [54]. It has been shown, for instance, that the presence of thermally decomposed IrO_2 on a *BDD* substrate strongly affects the electrochemical response of the diamond electrode. Thus, the behaviour of the composite electrode can be totally attributed to the electrochemical properties of the particles, even at low deposited IrO_2 loading.

5.2 Experimental conditions

Materials - High purity SnO_2 commercial powders (Aldrich, 99.99%, 325 mesh) and commercial RuO_2 xH_2O (Aldrich) were used. The mechanical treatment was carried out with a commercial Spex/Mixer Mill mod. 8000. Powder amounts of 8 g were introduced into a stainless steel vial with two stainless steel balls. The vial was then fixed on the mechanical arm and the mill operated at about 14.6 Hz. The treatment was interrupted after selected time intervals to empty the vial and refill it with a further 8 g of untreated powder. The powders extracted from the vial were then compacted to prepare disk-shaped samples for X-ray diffraction (*XRD*).

Electrodes -The electrochemical response of SnO_2 powder samples processed for 3, 16 and 24 hours, hereafter referred to as *S3*, *S16* and *S24* respectively, has been compared with that of untreated powders, hereafter referred to as *NM*. Powders were assembled onto the surface of *BDD* supports to obtain thin film electrodes. More specifically, 14 mg of powders were added to 1 cm^3 of distilled water and the system was subjected to ultrasonic treatment for 30 min to suitably disaggregate powder particles and disperse them in the liquid. 0.2 cm^3 of the suspension were then used to cover a *BDD* electrode surface with geometric area of 1 cm^2. Finally, the suspension was dried for 30 min at 80 °C in an oven. Approximately 2 mg of SnO_2 were thus deposited per square centimetre. The obtained oxide films were stable up to potentials of the order of 2.3 - 2.5 V, above which O_2 bubbling resulted in film rupture and detachment.

Physicochemical characterisation - *XRD* analyses were performed on a Rigaku D/Max diffractometer equipped with a Cu radiation tube and a graphite monochromator in the diffracted beam.

Electrochemical measurements - Experimental runs were performed in a conventional three-electrode cell in which the *BDD*/SnO_2 electrode worked as anode and a large platinum sheet as counter electrode. The reference was a saturated calomel electrode (*SCE*) connected to the cell by a Luggin capillary to minimize uncompensated ohmic drops. All the potential values hereafter quoted are referred to *SCE*.

A potentiostat (Model 7050 AMEL) and a frequency response analyser (FRA, Model 7200 AMEL) were used to perform voltammetric, polarization and spectroscopic analyses. Runs were carried out in aqueous solutions of H_2SO_4 at a concentration of 0.5 M. The potential interval explored during the course of voltammetric measurements ranged between the open circuit potential, typically between 0.1 and 0.2 V, and 2.5 V. Negative potential values have been also occasionally imposed to investigate the possible occurrence of SnO_2 phase transformations. Quasi steady-state polarisation runs were also carried out in the same potential range, the potential scan rate being 1 mVs^{-1}.

Electrochemical impedance spectroscopy measurements were performed by superimposing a sinusoidal signal with excitation amplitude of 10 mV at different bias potentials in the range from 0 to 2 V. Impedance spectra were recorded in the frequency range 0.1 to 1×10^5 Hz by collecting 16 points per decade. Zassist and ZsimpWin softwares were used, respectively, to drive the experiments and fitting the resulting curves to suitable equivalent circuits.

5.3 Results and Discussion

5.3.1 Physicochemical analysis

The XRD patterns of the SnO_2 powders were accurately analyzed by applying the well known Rietveld method [55]. This allowed a numerical reconstruction of the observed experimental XRD patterns *via* a best-fitting procedure involving the parameters characteristic of the set of mathematical functions employed to reproduce the peak profiles [55]. It was thus possible to estimate the average size L of coherent diffraction domains and the concentration of structural defects, quantified by the so-called microstrain content ε [55, 56]. The experimental XRD pattern of powders milled for 3 hours is shown in Figure 5.1, together with numerically refined peak profiles.

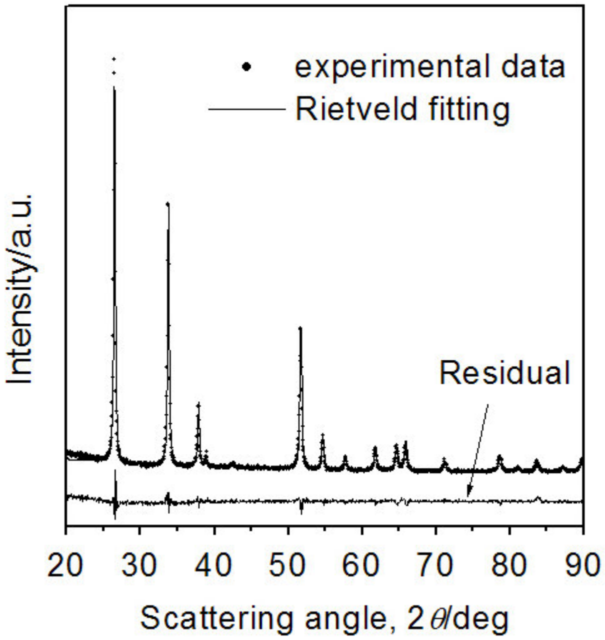

Figure 5.1. *Experimental XRD pattern of* SnO_2 *powders milled 3 hours as a function of the scattering angle* 2θ*. The best-fitted numerically reconstructed Rietveld pattern and the residual trace are also shown.*

The structural evolution of SnO_2 powders is illustrated from the average crystallite size L and microstrain ε values reported in Figure 5.2 as a function of the milling time t. It can be seen that, as expected, the gradual L decrease is paralleled by a progressive increase of ε.

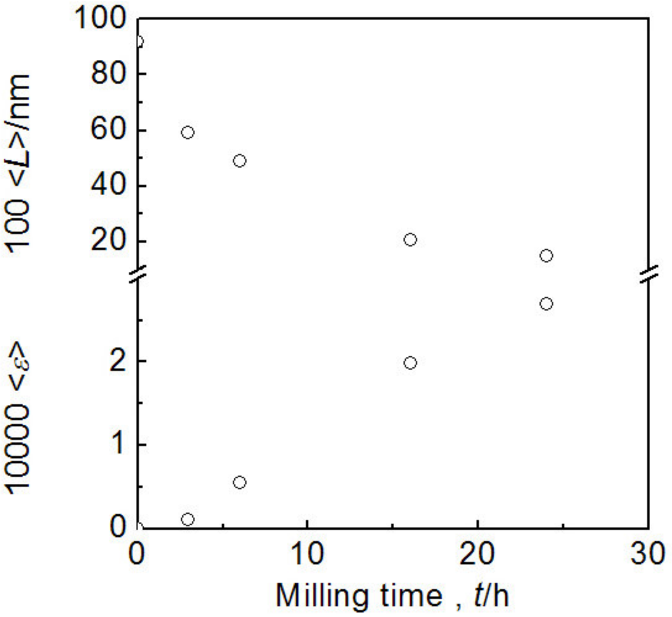

Figure 5.2. *Average crystallite size L and microstrain ε as a function of the milling time t.*

The decrease in the average size of single crystallites is therefore accompanied by the accumulation of structural disorder due to the generation of a far-from-equilibrium population of lattice defects such as vacancies, interstitials, dislocations and grain boundaries.

5.3.2 Electrochemical analysis

5.3.2.1 Cyclic voltammetric studies

A typical example of the curves obtained from cyclic voltammetry on *NM* powders in aqueous solution 0.5 M H_2SO_4 is reported in Figure 5.3. Aimed at pointing out the phase transitions possibly undergone by SnO_2 powders, a voltammetric cycle was performed with E_0= OCV, E_1= -0.8 V and E_2= 2.5 V.

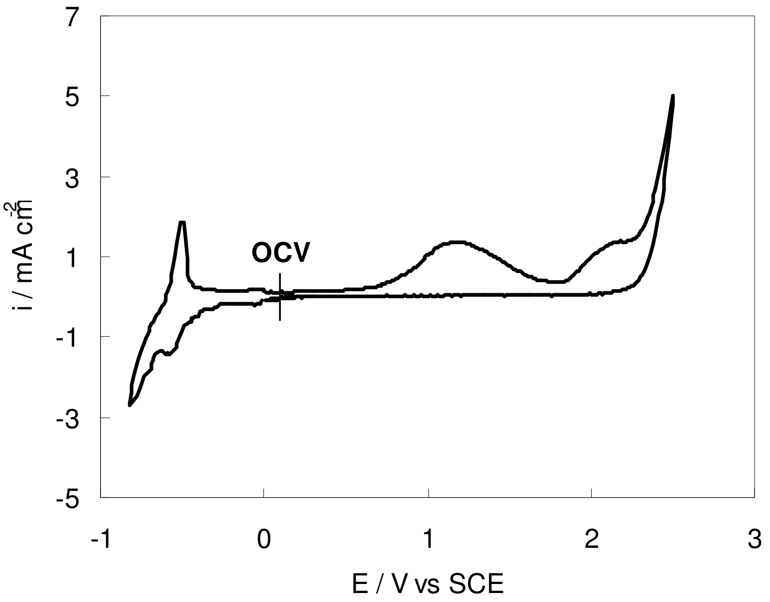

Figure 5.3. *Typical curves for cyclic voltammetry at NM powder electrode*s *performed with* E_0 *= OCV,* E_1 *= -0.8 V and* E_2 *= 2.5 V. Scan rate 100 mV* s^{-1}.

In accordance with literature [57], at a potential value of about -0.6 V the reduction of Sn(IV) to Sn(0) is observed. Oxidation to Sn (II) and Sn (IV) are then observed at about -0.4 V and 1.1 V. The O_2 evolution process is finally detected at higher anodic potentials.

As often pointed out [58-60], the mechanism of O_2 evolution at oxide electrodes is complicated and its full characterization and rationalization still challenge electrochemists. The reaction is typically a multi-stage one, the rate determining step depending on the strength of the intermediate product adsorption. In turn, this is governed by the oxide layer composition [58]. A detailed study has been carried out on PbO_2 [59] which is referred as a “non-active” oxide, as is the case of SnO_2. The reactivity of these species is mainly ascribed to the formation of a hydrated oxide layer containing sites able to bind hydroxide radicals $HO^{\bullet}$ during the course of O_2 evolution. Despite the process being a remarkably complex one, the following simplified mechanism has been proposed for the reaction taking place in acid medium [59, 60]:

$$SnO_2 + H_2O \rightarrow SnO_2(HO^\bullet) + H^+ + e^- \quad (5.1)$$

$$SnO_2(HO^\bullet) \rightarrow SnO_2 + H^+ + O + e^- \quad (5.2)$$

$$2\,O \rightarrow O_2 \quad (5.3)$$

$SnO_2(HO^\bullet)$ stands for the active site binding the $HO^\bullet$ species. According to such a mechanism, the peak detected in the voltammetric curve (Figure 5.3) before the current rise related to O_2 evolution can be ascribed to the intermediate stages of this latter process. The current density i measured at the potential E of 2 V is given in Figure 5.4 for the different powder samples as a function of the milling time t. The average specific surface area of crystallites S_p has also been reported for sake of comparison. S_p was evaluated according to the general expression:

$$S_p = \frac{f}{\rho \langle L \rangle} \quad (5.4)$$

where ρ is the SnO_2 density and f a shape factor. Under the simplifying assumption that powder particles have spherical shape, f was set equal to 6.

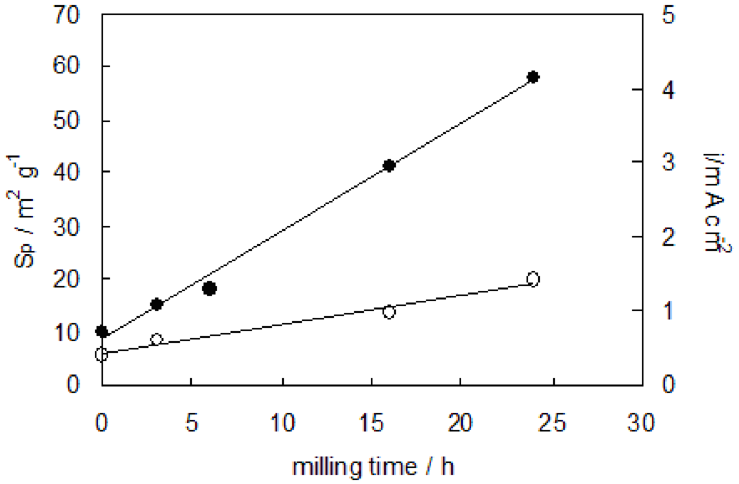

Figure 5.4. *Specific surface area of crystallites S_p (•) and electric current density j (o) measured at E= 2 V as a function of the milling time t.*

It can be seen that both quantities change linearly with t, thus suggesting a possible direct correlation. Providing S_p an indirect measure of the grain boundary extension, the observed i increase could be tentatively rationalised in terms of an increase of the active site number. In a sense, this would correspond to a connection between the current density i and the extension of grain boundaries in powder particles. It is however worth noting that mechanical processing is also able to promote the formation of sites with different chemical activity. In other words, it is expected that the chemical reactivity of surface sites pertaining to powders subjected to mechanical treatment is higher than the one of surface sites in untreated powders. Although the direct correlation between the total surface area of crystallites S_p and the current density i only suggests an increase in the total number of active surface sites, with no evidence of significantly different reactivity, this latter possibility cannot be excluded *a priori* on the basis of the aforementioned connection between grain boundary extension and electric current density. Further investigations were then carried out to specifically address this point.

5.3.2.2 Steady-state polarisation analysis

Polarization experiments were performed in the potential range between 1.5 and 2.5 V, the quasi steady-state current-potential data being recorded at a rate of 1 mV s^{-1}. As widely discussed [61], the Tafel plot provides only limited information on the reaction mechanism when electrodic reactions take place at very high potential as in the case of O_2 and O_3 evolution so that b values very different from the theoretical ones have often been obtained [62]. Nevertheless, in the present case a comparison between the behaviour of the different powder samples can still give useful information on their electrochemical catalytic activity. Following a standard procedure, data have been fitted with the equation:

$$\eta = a + b \log i \tag{5.5}$$

where η is the overpotential and a and b are the Tafel parameters. Their values are quoted in Table 5.1 together with the exchange current density i_0 calculated according to:

$$i_0 = \exp\left(-2.3\frac{a}{b}\right) \tag{5.6}$$

	b / mVdec^{-1}	***a / V***	***a* / V***	***i_o / mA cm^{-2}***	***i_o^* / mA cm^{-2}***
NM	196	1.423	1.089	5.61×10^{-8}	2.80×10^{-10}
S3	212	1.35	1.070	4.29×10^{-7}	8.97×10^{-10}
S16	228	1.314	1.064	1.76×10^{-6}	2.20×10^{-9}
S24	251	0.831	0.602	4.83×10^{-4}	3.97×10^{-7}

Table 5.1. *Values of Tafel parameters obtained at different samples. The asterisked values are derived from current density values normalised with respect to* S_p.

The i_0 value increases with milling time t, thus indicating a larger electrochemical catalytic activity for powders treated for longer times. It is, however, worth noting that i_0 is measured relative to the electrode geometrical surface area, which is only an apparent surface area. The differences in a values for powder samples processed for different milling times could be then due to the comminution process accompanying the mechanical treatment. In order to obtain a more representative quantity, data have been therefore normalised to the specific surface area of crystallites S_p obtained from *XRD* measurements. The resulting a^* and i_o^* values for the different samples, also reported in Table 5.1, are still characterized by significant differences, particularly between the *S24* sample and the remaining ones. This suggests that the mechanical processing not only determines an increase in the total surface area, and then of the number of active sites, but also modifies their nature.

5.3.2.3 Electrochemical impedance spectroscopy analysis

The results obtained from electrochemical impedance spectroscopy on the *NM* samples at different potentials are shown in Figure 5.5 as a Nyquist plot.

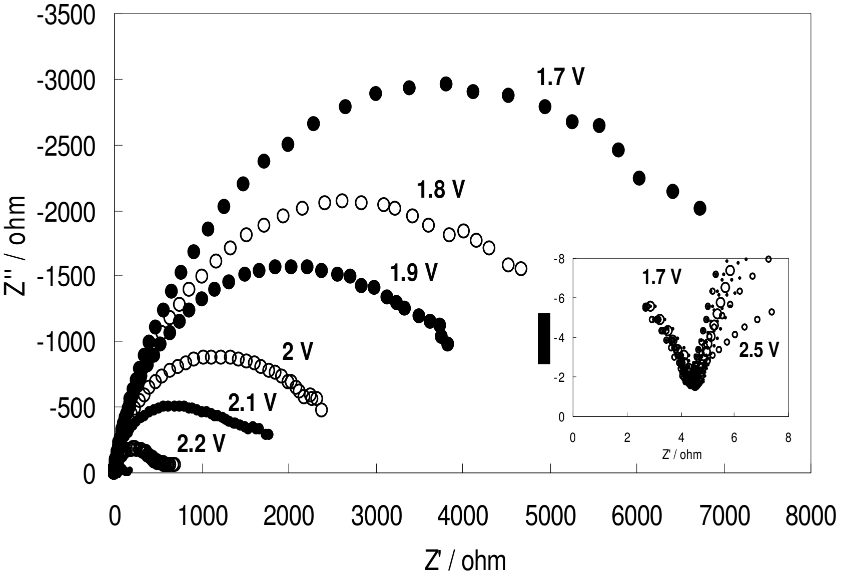

Figure 5.5. *Electrochemical impedance spectroscopy curves obtained at NM samples at the different potential values. The inset reports a close-up view of the high frequency region.*

As shown in the inset, a capacitive loop independent of potential is always observed in the high frequency region of experimental curves. Two other loops are detected in the lower frequency region, the resolution of which depends on the potential applied. Highest impedance values are observed at less positive potential and their values decrease progressively as the potential increases. Correspondingly, the capacitive loops become better defined and the polarization resistance for the *OER*, calculated by the low-frequency cut off of the curves on the real axis, decrease exponentially with applied potential according to a Buttler Volmer trend [63].

The polarization resistance R_p values can be adopted to support the experimental findings relative to the polarization curves. The polarization resistance can be expressed as:

$$R_p = \frac{\partial \eta}{\partial i} = \frac{b}{i_0}\exp\left(\frac{-2.3}{b}\eta\right) \tag{5.7}$$

It follows that:

$$\eta = b\log\left(\frac{1}{R_p}\right) - b\log\left(\frac{i_0}{b}\right) \tag{5.8}$$

Accordingly, a plot of η vs *log*(R_p^{-1}) gives the Tafel slope. The trend of η vs *log* (R_p^{-1}) (curve a) obtained for *NM* sample is given in Fig. 5.6 together with the Tafel plot (curve b).

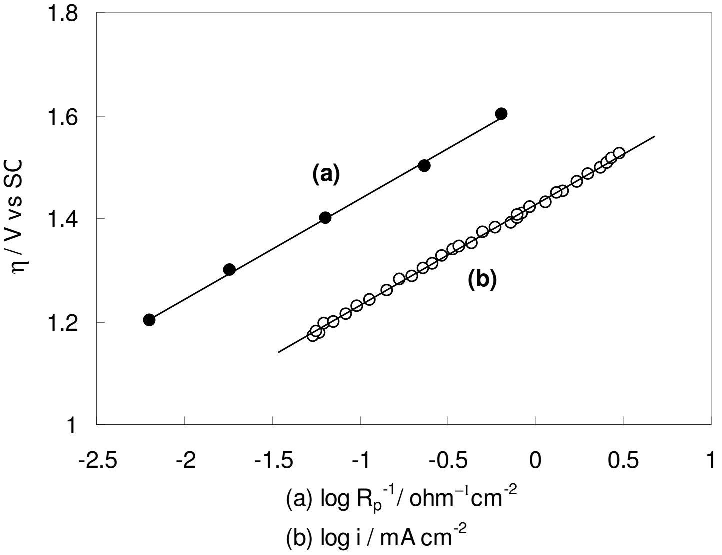

Figure 5.6. *Tafel plots for NM sample: (a) η vs log(R_p^{-1}) from impedance data, (b) η vs logi from quasi steady-state data.*

A *b* value of 195 mV dec^{-1} was calculated by fitting experimental data from impedance spectroscopy with Equation 5.8, which well agrees with the corresponding value obtained from the polarization curve (Table 5.1).

An example of the Nyquist diagrams obtained for the different electrodes at a potential of 2 V is shown in Figure 5.7.

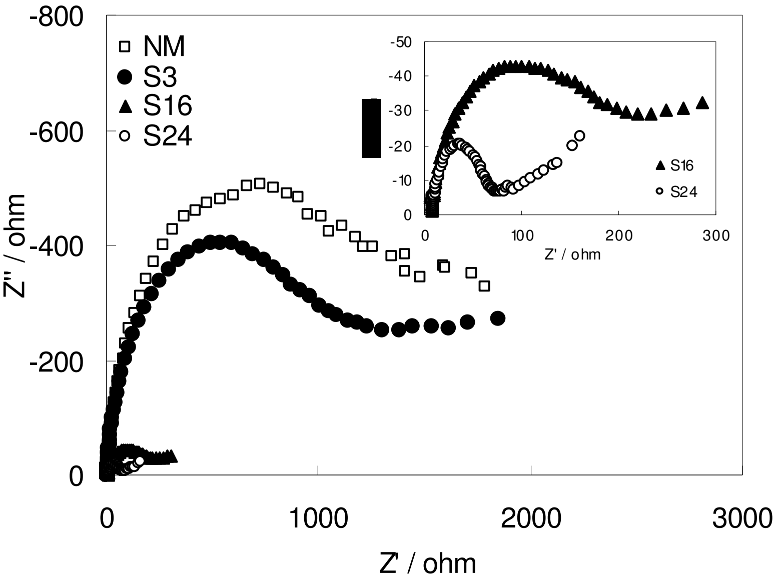

Figure 5.7. *Nyquist plots obtained at a potential of 2 V for the different samples. The inset shows a close-up view of the low impedance region. Range of investigated frequency 100kHz -1Hz.*

With the aim of carrying out a quantitative analysis of the experimental results obtained, the electrochemical response of the electrodes has been modelled according to the equivalent electrical circuit approach. To this end, in accordance with the aforementioned mechanism for O_2 evolution illustrated by Eqs. 5.1-5.3, the faradaic current i_F has been considered dependent on both the applied potential and an additional variable, θ, representing a measure of the reaction intermediate $SnO_2(HO^{\bullet})$ surface coverage. Following previous work [64] and the theoretical derivation of the Faradaic impedance reported in the previous section, the faradaic admittance, Y_F, of an electrode reaction with one state variable besides electrode potential can be written as:

$$Y_F = \frac{1}{R_{ct}} + \frac{B}{A + j\varpi} \tag{5.9}$$

where:

$$\frac{1}{R_{ct}} = \left(\frac{\partial i_F}{\partial E}\right)_{ss} \tag{5.10}$$

$$B = \left(\frac{\partial i_F}{\partial \theta}\right)_{ss} \left(\frac{\partial \dot{\theta}}{\partial E}\right)_{ss} \tag{5.11}$$

$$A = -\left(\frac{\partial \dot{\theta}}{\partial \theta}\right)_{ss} \tag{5.12}$$

Here R_{ct} is the transfer resistance of the electrode reaction and the subscript *ss* stands for steady state. As briefly mentioned above, θ is the reaction intermediate $SnO_2(HO^{\bullet})$ surface coverage, whereas $\dot{\theta}$ is its change rate $d\theta/dt$.

On the other hand, it is well established that a general equivalent circuit for the faradaic electrode process involving one state variable can be represented by the schematic quoted in Figure 5.8.

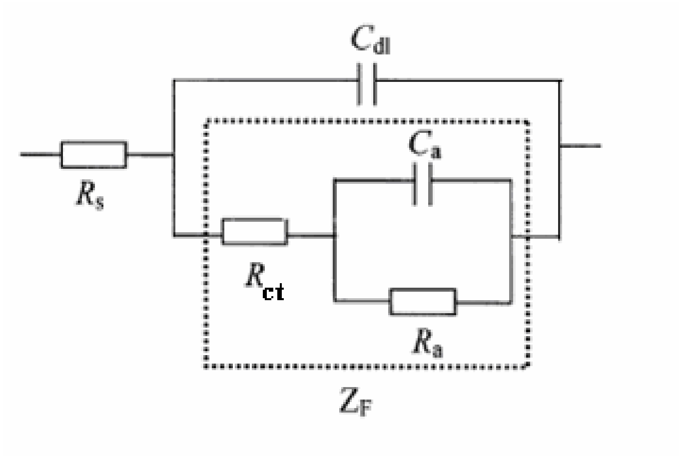

Figure 5.8. *Equivalent electric circuit for oxide electrodes during O_2 evolution reaction.*

The total impedance Z_T of the electrode process can be expressed by:

$$Z_T = R_s + \frac{1}{Y_F + j\varpi C_{dl}} \tag{5.13}$$

where C_{dl} is the double-layer capacitance, R_s the uncompensated solution resistance and Y_F the faradaic admittance. The faradaic impedance Z_F can be written as:

$$Z_F = \frac{1}{Y_F} = R_{ct} + \frac{R_a}{1 + j\varpi R_a C_a} \tag{5.14}$$

R_a and C_a represent, respectively, the equivalent resistance and capacitance associated with the intermediate adsorption.

The relationship between the electrical elements in the equivalent circuit and the electrochemical parameters in the faradaic admittance can be pointed out by comparing Eqs. 5.9 and 5.14. Accordingly:

$$B = \frac{-1}{R_{ct}^2 C_a} \tag{5.15}$$

$$A = \frac{1}{C_a}\left(\frac{1}{R_a} + \frac{1}{R_{ct}}\right) \tag{5.16}$$

It follows that two capacitive loops must be expected in impedance diagrams connected with the faradaic process. An additional element was added to the equivalent electrical circuit to take into account the capacitive response of the oxide film. This modifies the equivalent electrical circuit shown in Figure 5.8 into that schematically depicted in Figure 5.9.

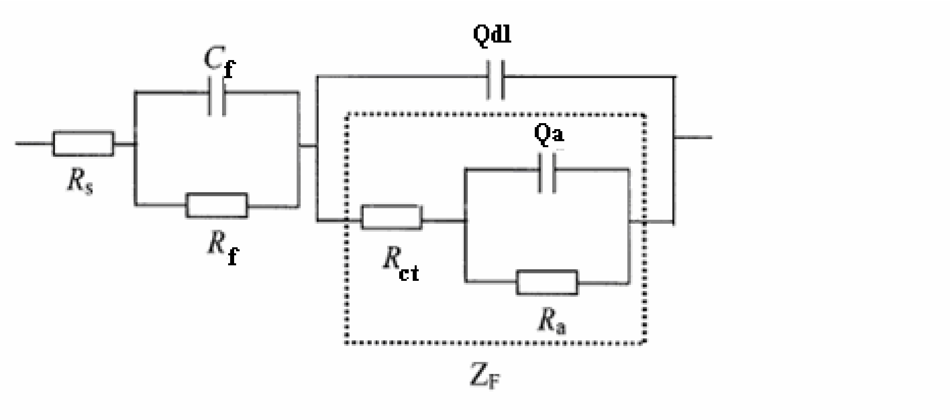

Figure 5.9. *Modified equivalent electric circuit for oxide electrodes during O_2 evolution reaction.*

Constant phase elements *(CPEs)* were used instead of capacitors *(C)* to fit experimental data. According to literature [65-67], using *CPEs* is a good approach for studying solid electrodes with different degrees of surface roughness and nonuniform structure or distribution of reactive surface sites. The *CPE* impedance can be expressed as:

$$Z_{CPE} = \frac{1}{Q(j\varpi)^n} \tag{5.17}$$

Q representing the capacity parameter expressed in S cm^{-2} s^{n} and n accounting for the deviation from the ideal behaviour, n being 1 for a perfect capacitor.

Figure 5.10 depicts an example of the fit between experimental data and fitting curves based on the complex nonlinear least squares (*CNLS*) method for the sample *NM*.

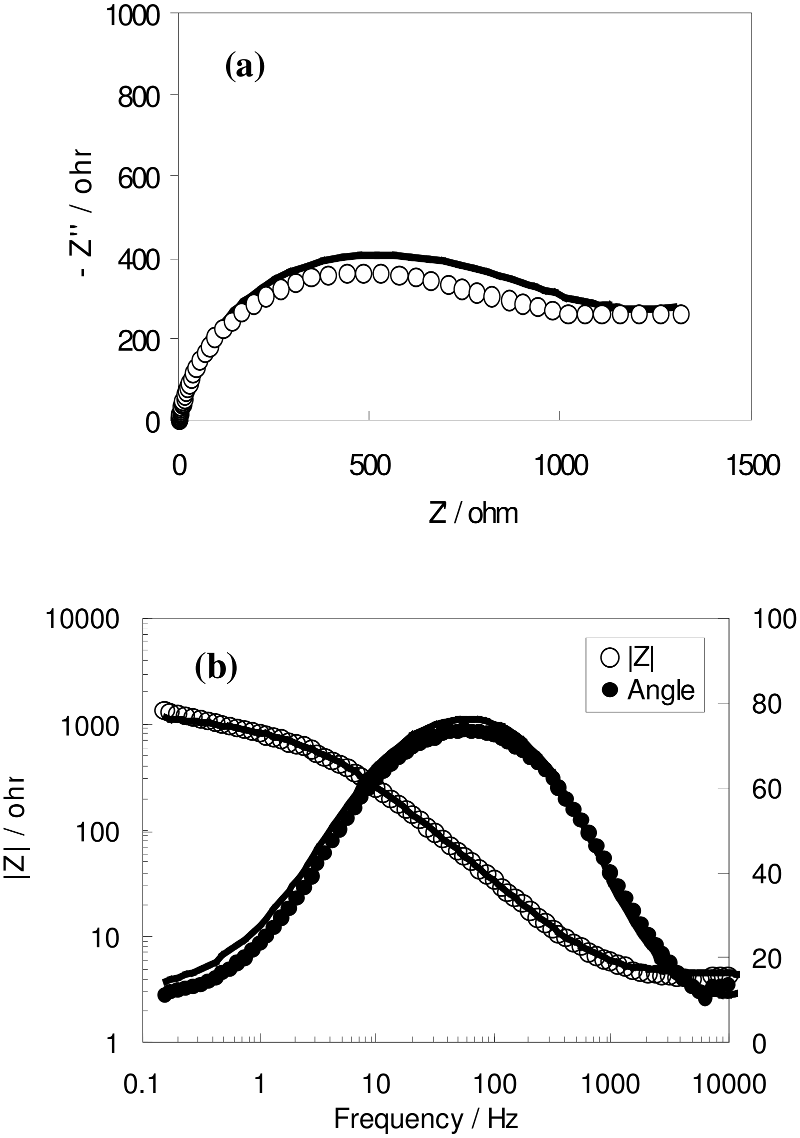

Figure 5.10. *Example of the fit between calculated and experimental Nyquist (a) and Bode (b) modulus and phase angle plots at E = 2 V. Range of investigated frequency 100kHz -1Hz.*

The equivalent electrical circuit parameter values obtained for the different samples at a potential E value of 2 V are quoted in Table 5.2.

E = 2 V vs SCE		***NM***	***S3***	***S16***	***S24***
R_s	ohm	0.2	0.03	0.01	0.01
C_f	μF	0.4	0.7	0.2	0.1
R_f	ohm	4.0	4.4	8.3	9.7
Q_{dl}	μS s^n	60	54	27	34
n	-	0.96	0.94	0.97	1
R_{ct}	ohm	800.5	782.2	45.7	26.3
Q_a	mS s^n	0.3	0.5	0.4	2.1
n	-	0.9	0.96	0.64	0.46
R_a	ohm	1002.1	725.4	164.1	50.9

Table 5.2 . *Values of the parameters of the equivalent electrical circuit reported in Figure 5.9, derived for the different samples from runs performed at E = 2 V.*

It can be seen that the film resistance increases with the milling time *t*. The mechanical treatment determines a comminution of powder particles, with a corresponding increase of the specific free surface, and an increase in their lattice defect content. The decrease in average crystallite size corresponds to an increase in grain boundary extension area. As a consequence, the intensity of scattering events involving charge carriers at grain boundaries also increases. A decrease of the overall charge carrier mobility is therefore observed and, in turn, an electrical resistivity increase [68]. The formation of highly defective grain boundaries is further highlighted by the decreasing *CPE* exponent of the electrical element connected with the reaction intermediate $SnO_2(HO^{\bullet})$ absorption: high values of n are measured for samples milled up to 3 hours which becomes 0.46 for sample *S24*. Additional evidence of the capability of mechanical processing of enhancing the chemical reactivity of powders via the disordering of crystalline lattice is provided by the progressively decreasing R_{ct} and R_a values.

5. 3.2.4. Preliminary investigation at RuO_2-SnO_2 mixed oxide systems

The purpose of using mixed oxides is to modulate the electrochemical properties of the active layer by modifying its composition. Various outcomes can be reached, depending on the degree of mixing of the constituent oxides. The properties of the pure oxides may add up proportionally to their content if a phase mixture is obtained, while a true synergistic effect can be expected if intimate mixing (solid solution) is achieved.

Several attempts were made in the past to prepare mixed $(Sn\text{-}Ru)O_2$ solid solutions. However, most early attempts yielded to the formation of oxide material with more than one phase. Ito et al. reported the formation of RuO_2-SnO_2 binary oxide by a sol-gel process, although both unmixed RuO_2 and metallic Ru were found in some samples [3]. Heat treatment of the binary oxides at elevated temperature (>600 °C) yields to phase separation, confirming the fact that SnO_2 and RuO_2 do not form a solid solution at equilibrium. Mixed SnO_2-RuO_2 oxides have also been prepared by the thermal decomposition method, by limiting the firing temperature and the firing time [5]. However, most samples exhibit two different oxide phases, one richer in RuO_2 than the other one. In that respect, the use of high-energy ball milling to prepare mixed $(Sn\text{-}Ru)O_2$ oxide can be more interesting being the resulting material made of a single phase [1].

On these bases, in this study, binary oxides will be prepared by high-energy ball milling over the whole composition range. However, at the present, only the system RuO_2 -SnO_2 (15:85 at. %) were analysed. A complete kinetic study of oxygen evolution at RuO_2-SnO_2 electrodes was not carried out, so it is not possible to establish a precise mechanism for this family of electrodes. However, an example of the Nyquist diagrams obtained for the SnO_2-RuO_2 electrodes at a potential of 2 V is shown in Figure 5.11.

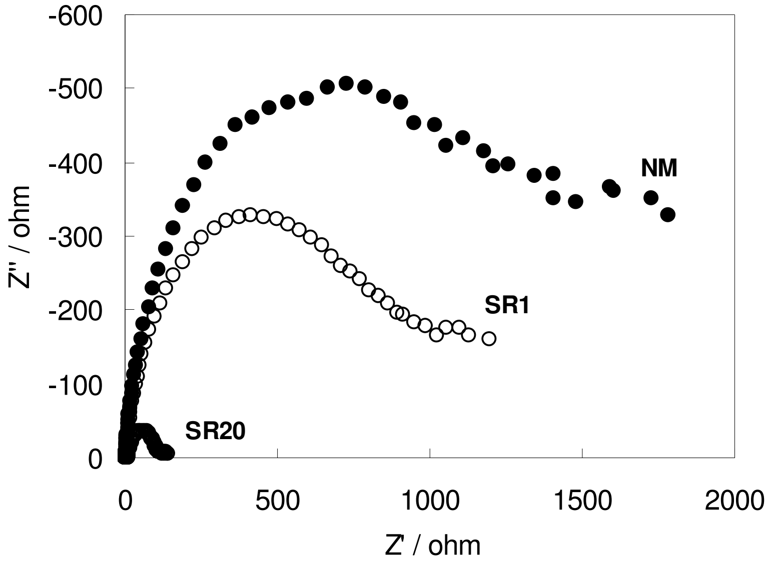

Figure 5.11. *Nyquist plots obtained at a potential of 2 V for the different samples. Range of investigated frequency 100 kHz -1Hz.*

As we can see, in the samples processed for 1 hour (*SR1*), the introduction of a 15% of RuO_2 does not improve significantly the catalytic activity with respect to the *NM* sample. Actually, in this condition, SnO_2 and RuO_2 probably do not form a solid solution, and it is not easy establish the real contribute of the phase rich in RuO_2. After 20 hours of milling, the samples (*SR20*) showed higher electrocatalytic activity towards oxygen evolution reaction. Further work is need to verify the possible enhanced of the catalytic activity of the samples, in particular the formation of a possible single phase (tetragonal) (Sn-Ru)O_2 solid solution will be verified through XRD analysis.

5.4 Conclusions

The present work represents a preliminary investigation of the electrochemical properties of mixed oxide powders subjected to mechanical processing relative to the oxygen evolution reaction in acid medium. The use of high-energy ball milling to prepare these electrodes demonstrated to be a promising method to produce active powder oxide. Cyclic voltammetry, electrical polarization and electrochemical impedance spectroscopy experiments have been carried out to gain information on the mechanistic scenario underlying the chemical reaction and, indirectly, on the modifications connected with powder particle deformation. This latter determined a significant decrease in the average crystallite size and the accumulation of structural disorder. According to the equivalent circuit approach, such processes resulte in an increase in the thin film resistance. The larger grain boundary extension related to the crystallite size decrease determined indeed a corresponding decrease in the charge carrier mobility. At the same time, evidence has been found suggesting that the enhanced catalytic activity of processed powders can be related not only to the grain boundary extension increase, but also to the generation of surface active sites with different reactivity. Further work is needed to study the catalytic activity of the mixed oxide samples, in particular the possible formation of a single phase solid solution will be verified.

5.5 References

[1] J. Gaudet, A.C. Tavares, S. Trasatti, D. Guay, Chem. Mater. 17 (2005) 1570

[2] W. Badawy, K. Doblhofer, I. Eiselt, H. Gerischer, S. Krause, J. Melsheimer, Electrochim. Acta 29 (1984) 1617

[3] M. Ito, Y. Murakami, H. Kaji, H. Ohkawauchi, K. Yahikozawa, Y. Takasu, J. Electrochem. Soc. 141 (1994) 1243

[4] M. Ito, Y. Murakami, H. Kaji, K. Yahikozawa, Y. Takasu, J. Electrochem. Soc. 143 (1996) 3

[5] L. Nanni, S. Polizzi, A. Benedetti, A. De Battisti, J. Electrochem. Soc. 146 (1999) 220

[6] E.N. Balko, P.H. Nguyen, J. Appl. Electrochem. 21 (1991) 678

[7] C.P. De Pauli, S. Trasatti, J. Electroanal. Chem. 396 (1995)161

[8] D.T. Shieh, B. Hwang, J. Electrochim. Acta 38 (1993) 2239

[9] A. Bandi, I. Vartires, A. Mihelis, C. Haina˜sürosie, J. Electroanal. Chem. 157 (1983) 241

[10] J.F.C. Boodts, S. Trasatti, J. Electrochem. Soc. 137 (1990) 3784

[11] A.I. Onuchukwu, S. Trasatti, J. Appl. Electrochem. 21 (1991) 858

[12] R. Hutchings, K. Mu¨ller, R. Ko¨tz, S. Stucki, J. Mater. Sci. 19 (1984) 3987

[13] T.A.F. Lassali, L.O.S. Bulho˜es, L.M.C. Abeid, J.F.C. Boodts, J. Electrochem. Soc. 144 (1997) 3348

[14] J. Forti, P. Olivi, A.R. Andrade, Electrochim. Acta 47 (2001) 913

[15] S. Wen, S. Chen, D. Tang, J. Chlor-Alkali Ind. 8 (1996) 23

[16] Z. Jin, H. J. Zhou, Z.-L. Jin, R.F. Savinell, C. C. Liu, Sens. Actuators B 52 (1998) 188

[17] O.K. Varghese, L.K. Malhotra, G.L. Sharma, Sens. Act. B. 55 (1999) 161

[18] A.P. Rizzato, L. Broussous, C.V. Santilli, S.H. Pulcinelli, A.F. Craievich, J. Non-Cryst. Solids 284 (2001) 61

[19] G. Korotchenkov, V. Brynzari, S. Dmitriev, Sens. Actuators B. 54 (1999) 197

[20] J.R. Brown, P.W. Haycock, L.M. Smith, A.C. Jones, E.W. Williams, Sens. Actuators B. 63 (2000) 109

[21] A.K. Mukhopadhyay, P. Mitra, A.P. Chatterjee, H.S. Maiti, Ceram. Int. 26 (2000) 123

[22] R.K. Sharma, P.C.H. Chan, Z. Tang, G. Yan, I. Hsing, J.K.O. Sin, Sens. Actuators B 72 (2001) 160

[23] S. I. Rembeza, E. S. Rembeza, T. V. Svistova, O. I. Borsiakova, Phys. Stat. Sol. A. 179 (2000) 147

[24] A. Cirera, A. Cornet, J.R. Morante, S.M. Olaizola, E. Castaño, J. Gracia, Mater. Sci. Eng. B 69–70 (2000) 406

[25] R.W. Siegel, E. Hu, M.C. Roco (Eds), Nanostructure Science and Technology,. WTEC, Loyola College, Maryland, 1999

[26] C. Suryanarayana, Prog. Mater. Sci. 46 (2001)1

[27] P.Yu Butyagin, Sov. Sci. Rev. B Chem. 14 (1989) 1

[28] E.M. Gutman, Mechanochemistry of Materials, Cambridge International Science Publishing, Cambridge (1998)

[29] F.Kh.Urakaev, V.V. Boldyrev, Powder Tech. 107 (2000) 93

[30] F. Delogu, C. Deidda, G. Mulas, L. Schiffini, G. Cocco, J. Mater. Sci. 39 (2004) 1

[31] T.H. Courtney, Mater. Trans. JIM 36 (1995)110

[32] P. Bellon, R.S. Averback, Phys. Rev. Lett. 74 (1995) 1819

[33] R.G. Hoagland, M.I. Baskes, Scripta Mater. 39 (1998) 417

[34] X.Y. Fu, M.L. Falk, D.A. Rigney, Wear 250 (2001) 420

[35] A.C. Lund, C.A. Schuh, Appl. Phys. Lett. 82 (2003) 2017

[36] P.Yu Butyagin, A.N. Streletskii, Phys. Solid State 47 (2005) 856

[37] V.I. Levitas, Phys. Rev. B 70 (2004) 184118

[38] S. Odunuga, Y. Li, P. Krasnochtchekov, P. Bellon, R.S. Averback, Phys. Rev. Lett. 95 (2005) 045901

[39] F. Delogu, G. Mulas, S. Enzo, L. Schiffini, G. Cocco, Chem. Sust. Develop. 15 (2007) 157

[40] Y.V. Pleskov, Russ. Chem. Rev. 68 (1999) 381

[41] G. Sine´, Ch. Comninellis, Electrochim. Acta 50 (2005) 2249

[42] F. Montilla, E. Morallon, I. Duo, Ch. Comninellis, J.L. Vazquez, Electrochim. Acta 48 (2003) 3891

[43] B. El Roustom, G. Foti, Ch. Comninellis, Electrochem. Comm. 7 (2005) 398

[44] N. Vinokur, B. Miller, Y. Avyigal, R. Kalish, J. Electrochem. Soc. 146 (1999) 125

[45] A.J. Saterlay, S.J. Wilkins, K.B. Holt, J.S. Foord, R.G. Compton, F. Marken, J. Electrochem. Soc. 148 (2001) E66

[46] F. Marken, A.S. Bhambra, D.H. Kim, R.J. Mortimer and S.J. Stott, Electrochem. Commun. 6 (2004) 1153

[47] K.J. McKenzie, F. Marken, Electrochem. Solid State Lett. 5 (2002) E47

[48] S. Ferro, A. De Battisti, J. Phys. Chem. B 106 (2002) 2249

[49] K.J. McKenzie, F. Marken, Electrochem. Solid-State Lett. 5 (2002) E47

[50] C. Terashima, T.N. Rao, B.V. Sarada, N. Spataru, A. Fujishima, J. Electroanal. Chem. 544 (2003) 65

[51] K.J. McKenzie, D. Asogan, F. Marken, Electrochem. Commun. 4 (2002) 820

[52] Y. Zhang, S. Asahina, S. Yoshibira, T. Shirakashi, Electrochim. Acta 48 (2003) 741

[53] K.B. Holt, G. Sabin, R.G. Compton, J.S. Foord, F. Marken, Electroanalysis 14 (2002) 797

[54] F. Montilla, E. Morallon, I. Duo, C. Comninellis, J.L. Vazquez, Electrochim. Acta 48 (2003) 3891

[55] L. Lutterotti, R. Ceccato, R. Dal Maschio, E. Pagani, Mater. Sci. Forum 278 (1998) 87

[56] H.P. Klug, L.E. Alexander, X-Ray Diffraction Procedures, Wiley-Interscience, New York (1974)

[57] P.S. Patil, P.S. Chigare, S.B. Sadale, S.H. Mujawar, P.S. Shinde, Solar Energy Materials & Solar Cells 91 (2007) 859

[58] G.N. Martelli, R. Ornelas, G. Faita, Electrochim. Acta 39 (1994) 1551

[59] R. Amadelli, A. Maldotti, A. Molinari, F.I. Danilov, A.B. Velichenko, J. Electroanal. Chem. 534 (2002) 1

[60] M.A.Q. Al faro, S. Ferro, C.A. Martinez-Huitle, Y.M. Vong, J. Braz. Chem. Soc. 17 (2006) 227

[61] F.B. Li, R. Hillman, S.D. Lubetkin, Electrochim. Acta 37 (1992) 2723

[62] K.C. Fernandes, L.M. Da Silva, J.F.C. Boodts, L.A. De Faria Electrochim. Acta 51(2006) 2809

[63] L. Meilin, W. Zhonglin, Solid State Ionics 107 (1998) 105

[64] C.N. Cao, Electrochim. Acta 35 (1990) 831

[65] U. Rammelt, G. Reinhard, Electrochim. Acta 35 (1990) 1045

[66] S. Gudic, J. Radosevic, M. Kliskic, J. Appl. Electrochem. 26 (1996)1027

[67] N. Spataru, J.G. Lehelloco, R. Durand J. Appl. Electrochem. 26 (1996) 397

[68] V. Bilgin, S. Kose, F. Atay, I. Akyuz, Mater. Lett. 58 (2004) 3686

Chapter 6

Non-active electrodes: Boron-doped diamond

6.1 Introduction

Since the first paper about the electrochemistry of boron doped diamond (*BDD*) published in 1987 by Pleskov et al.[1], *BDD* thin films are found to be particularly attractive due to their outstanding properties, which are significantly different from those of other conventional electrodes, e.g. glassy carbon or platinum electrode. The peculiar characteristics of *BDD*, including an extremely wide potential working range with low background currents in aqueous and non-aqueous solutions [2] and an extreme physical and chemical stability, make it one of the most ideal electrode materials for electroanalysis and electrosynthesis [3,4]. In the recent years, attention has been paid also on application of this material in oxidation of organics and electrochemical treatment of industrial wastes [5].

Actually, the attention which boron doped diamond has attracted in this last decade is so great that citation of all the papers which have appeared in the literature is very difficult. Wide-ranging work has been carried out by several research groups, such as those of Swain [6-10], Fujishima [11–17], Comninellis [17–20] and Pleskov [21–24], just to cite some of their more recent papers. Some scientific journals and several congresses have been specifically devoted to the presentation of results obtained, both in basic studies and for possible applications of this material in electroanalytical devices and electrochemical processes [25–29].

Despite this, many questions are still open and the comprehension of the electrochemical behaviour of *BDD* is not yet completely achieved. Several attempts were made in order to study the factors that can influence the behaviour of *BDD* electrodes, which easily pass from metal like behaviour for highly doped films (in outer sphere redox solutions they operate as nearly reversible electrodes) to semi-insulating behaviour, for moderately doped films which demonstrate irreversible electrochemical behaviour [30].

Actually, several factors may heavily influence the electrochemical performance of this material, such as doping level, morphological features (grain boundaries and point defects), non-diamond impurity content and surface group functionalities [31]. Several results have been published and different hypotheses have been proposed, but unfortunately an objective comparison between them is hard, due to the lack of a standard diamond electrode material to compare results against. Moreover, it is also necessary to point out that reproducible results could be achieved only if we have the exact knowledge of the “history” of the electrode.

With this objective, an experimental study was started in our laboratory to investigate the effect of an oxidative process on the structure of a highly doped *(HD) BDD* sample. The results from Raman analysis were combined with those from electrochemical investigation in order to explain the evolution of electrochemical activity and structural changes of *BDD* samples as the ageing time was increased. Great attention has been paid on the effect of possible graphitic domains or superficial defects, but overall on the hydrogen contained in the structure, which can play a fundamental role in determining the conductivity and the global electrochemistry of the sample.

Then, the study was extended in this work to less doped samples *(LD)*. The study was completed by an investigation of the capacitance-voltage characteristics that allowed calculation of the flat band potential and the energetic levels of conduction and valence bands of diamond, very important parameters in understanding the evolution of the sample behaviour with time.

6.2 Experimental conditions

The samples - Commercial *BDD* films (CSEM, the Swiss Center for Electronics and Microtechnology, Inc.), 1 μm thick, were grown by hot filament chemical vapor deposition (*HFCVD*) at 850 °C from a 0.5% H_2/CH_4 mixture at a pressure of about 5000 Pa (40 torr). The substrate was a p-type polished silicon wafer (1 mm) with a resistivity of about 10 mΩ cm^{-1}. Boron doped diamond with a doping level of 4000 and 1300 ppm was used in the experimental runs.

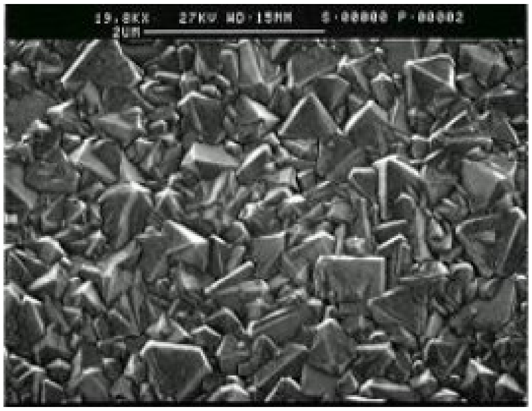

Figure 6.1. *SEM image of a BDD*

The electrodes were assembled over a stainless steel base and electrical contacts were made with a silver-based paste to the backside of the substrate. The lateral faces were isolated with silicon wax. If not differently specified, a surface area of 1 cm^2 has to be considered as exposed working area in the experiments. The assembly was mounted as working electrode in a conventional three electrode cell with *SCE* (saturated calomel electrode) as a reference electrode. A large area platinum sheet was used as counter electrode. The electrodes did not suffer surface pre-treatment before the electrochemical ageing tests.

The cell was controlled by a potentiostat (Amel 7200), whereas the electrical impedance measurements were performed by a frequency response analyser (AMEL FRA 7050) in conjunction with the previous set-up.

Ageing tests - Ageing tests were performed in which the samples in 0.5 M sulphuric acid were submitted to potentiostatic runs (E = 2.8 V) for about 500 h. At suitable intervals of time, the tests were stopped and the samples were submitted to specific electrochemical investigation carried out both in direct current and in alternating current to evaluate their catalytic activity towards specific test reactions. For reason of clarity, in the rest of the text, the tested samples will be indicated as Si where i is the number of hours in the ageing test. Ageing tests were also repeated at samples which, after 350 working hours, were left at rest for about 5 months: these samples will be indicated as *SRi.*

Raman measurements - Micro-Raman measurements have been carried out in back scattering geometry by using the polarized 514.5 nm line of an Argon-ion laser. Raman scattering measurements have been performed in air at room temperature with a triple spectrometer Jobin-Yvonne Dilor integrated system with a spectral resolution of about 1 cm^{-1}. Spectra have been recorded in the Stokes region by a 1200 grooves/mm grating monochromator and CCD detector system. Confocal microscope Olympus B-201 has been used, with an objective ×100 with 0.90 numerical aperture. The spatial resolution was less than 1 μm. In order to verify the homogeneity of the samples and the reproducibility of the reported data, all the measurements have been repeated in different random points of the samples.

Electrochemical characterisation - The reactions of the redox couple ferro/ferri cyanide (0.5 M KNO_3, 5 mM $K_4Fe(CN)_6$, 5 mM $K_3Fe(CN)_6$) and the oxygen evolution from sulphuric acid (0.5 M) were selected in order to test the catalytic activity of the differently aged samples. A range of potential between –0.6 and 0.6 V vs SCE was investigated in the cyclic voltammetric runs, whereas a potential bias of 0.2 V was applied in the case of electrochemical impedance measurements at which a sinusoidal signal with an excitation amplitude of 10 mV was superimposed. The impedance spectra were recorded in the frequency range 0.1 Hz – 100 kHz. The resulting curves were fitted to suitable equivalent circuits by using the ZsimpWin software. Moreover, to get information on the electronic structure of the samples, the Mott Shottky *(MS)* analysis was performed through *EIS* carried out in a wide range of potential.

6.3 Results and discussion

6.3.1 Relationship between electrochemical activity and ageing time at highly doped BDD sample.

The good quality of boron doped diamond utilised during the measurements has been revealed by its Raman spectrum (Figure 6.2): silicon substrate peaks are located at 520.7 and 950 cm^{-1}, whereas the Raman peak at 1332 cm^{-1} is attributed to the contribution of undoped diamond [32].

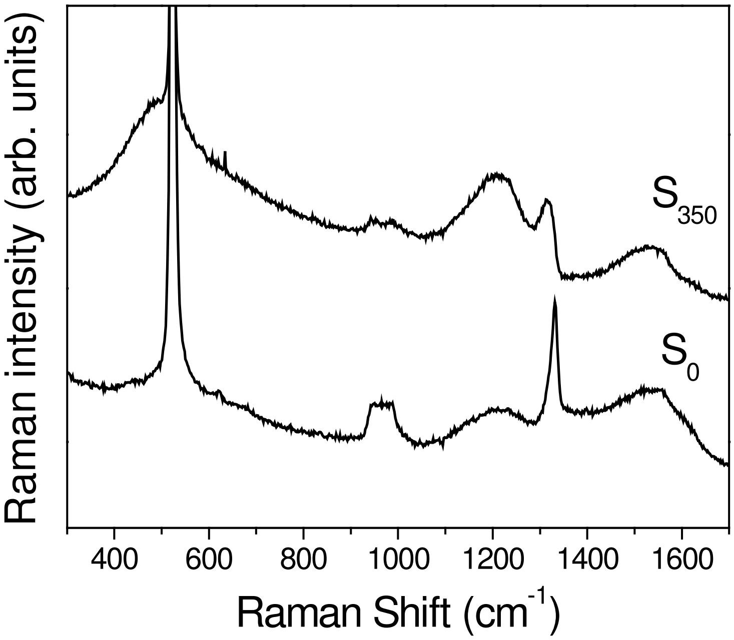

Figure 6.2. *Raman Spectra of the newly prepared sample (S_0) and of the same sample after 350 anodic working hours (S_{350}).*

The wide band located at about 1200 cm^{-1} has been previously attributed to reticular distortion or q≠0 phonons contribution activated by disorder [32,33] and to the presence of diamond nanocrystallites in the bulk of the sample [34,35]. However, this peak can be also related to the contribution of trans-polyacetylene segments at grain boundaries and surfaces [36-38]. The peak at about 1500 cm^{-1} has been attributed to the G mode of disordered carbon [32,39]. The presence of a graphite phase in commercial samples is not unusual; the possibility to reveal a few percentage of the graphite phase in the diamond lattice through the Raman analysis is due to the high Raman efficiency of the graphite band with respect to the diamond signal: actually, sp^2 sites have much larger cross section for visible Raman than sp^3 sites, about 50–250 times [36].

Figure 6.3 shows the behaviour of the samples in acid solution. In particular, it shows the current–potential curves recorded for up to 1 h aged samples: the curve related to the newly prepared sample (S_0) is higher than the others and the current decreases as the working time increases, indicating a fast decrease of the conductivity of the sample.

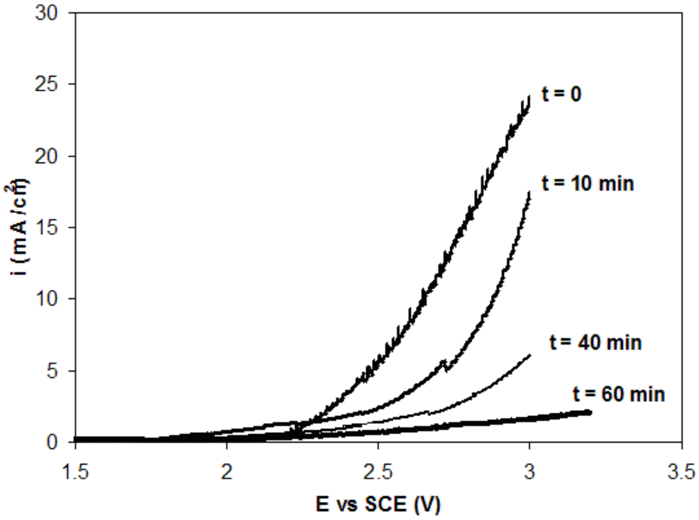

Figure 6.3. *Trend of current density vs potential curves obtained at the newly prepared sample and during the first hour of work.*

Information about the sample structure can be deduced from the results of electrochemical impedance spectroscopy analysis. The answer of the system to an alternating current signal is generally measured in terms of Nyquist (real vs. imaginary impedance) or Bode (phase angle vs. frequency, modulus vs. frequency) plots, and it can be interpreted with equivalent circuits in which capacitors and resistors are combined in series and/or in parallel to simulate the real answer of the system.

In the present case, the general trend of the Nyquist diagram was always constituted by two elements, more or less evident depending on the sample. The global answer of the system has been described by an equivalent circuit in which the solution resistance R_s is combined with two elements R and C in series, related to the resistive/capacitive answers of the diamond film and of the electrode/solution interface. Depending on the respective values of parameters involved, these two elements will play a different role, the higher resistive element being controlling for the total current through the electrode [39-40]. Actually, *CPEs* (constant phase elements) are used instead of *C*, in order to take account for possible not ideal behaviour of the capacitors. Two parameters determine the *CPE* conductance ($Y=Y_0(j\omega)^n$): Y_0 which represents the frequency-independent parameter and n which represents the deviation from the ideal behaviour, being $n=1$ for perfect capacitor. The behaviour of a Warburg element *W*, which takes into account possible diffusion effects, may be also represented by *CPE* when $n=0.5$.

Figure 6.4 illustrates a typical trend of the *EIS* spectra obtained at S_0, S_1, S_2 and S_{350} samples.

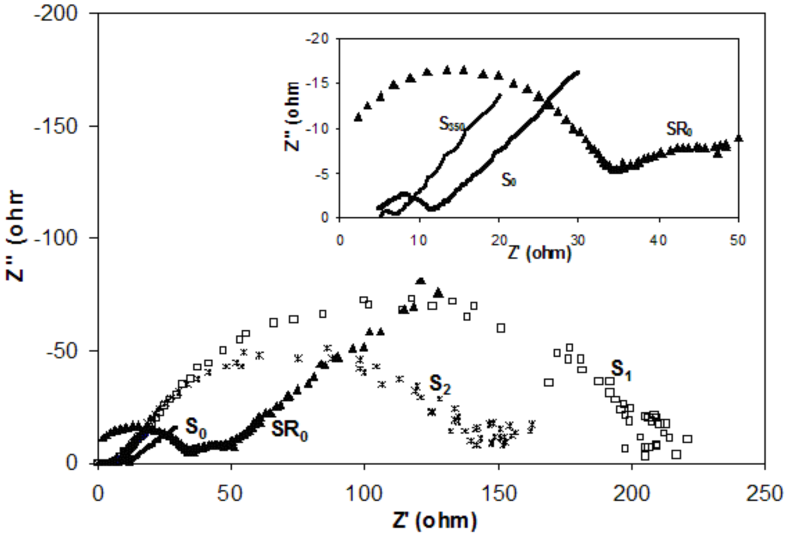

Figure 6.4. *Imaginary vs real part of impedance (Nyquist plot) obtained at newly prepared (S_0), passivated (S_1, S_2), and activated (S_{350}) samples, compared with that related to the sample SR_0. Electrolyte was ferri/ferrocyanide; bias potential E = 0.2 V; range of frequency investigated 100 kHz to 0.1 Hz. Inset: Enlargement of the high frequency zone of the plot.*

Increasing impedance values are measured from the Nyquist diagrams related to the initial working time: the answer of the system, which in the S_0 was represented by two well distinct elements, is characterised by just one semicircle in case of S_1 and

S_2 samples. As the working time increases, not only a variation of the impedance values, but also a variation in the shape of the diagram is observed, indicating the different ratio between the capacitive/resistive answer of the film with respect to that of the electrode/solution interface.

Table 6.1 resumes the values of the parameters of the equivalent circuits, calculated by fitting the experimental *EIS* data on the basis of a complex non linear least square algorithm (ZsimpWin software).

Sample	Equivalent circuit	Parameters					
		Y_{01} (S s ^{n})	n_1	R_1 (Ω)	C_2 (F)	R_2 (Ω)	W (S s $^{0.5}$)
S_0	$R_s(Q_1R_1)W$	1.x10^{-4}	0.7	7.2			0.05
S_1	$R_s(Q_1R_1)$	8.6x10^{-5}	0.8	198			
S_2	$R_s(Q_1R_1)$	1.x10^{-4}	0.8	141			
S_{350}	$R_s(Q_1R_1)W$	1.x10^{-4}	0.7	2.04			0.66
SR_0	$R_s(Q_1R_1)(C_2R_2)W$	1.x10^{-4}	0.9	10.8	1.4x10^{-7}	32	0.0056

Table 6.1. *Equivalent circuits and relevant fitting parameters calculated for the differently aged samples. Subscripts 1 and 2 refer to parameters related to the capacitive response of the bulk and boundary grains, respectively. The capacitive answer of the electrode/solution interface is always represented by a Warburg element W; the solution resistance Rs (not reported), was always less than 10 Ω.*

The resistances of the film obtained from the fitting are also reported in this table where the maximum value of resistance measured for S_1 is well evident. The high values of the resistance of the film measured for S_1 and S_2 samples make the capacitive/resistive answer of the film prevailing with respect to that of the electrode/solution charge transfer process, so that a single loop is visible in the spectrum.

The cyclic voltammetry (Figure 6.5) registered after 1 h of anodic treatment reveals an asymmetric shape, typical of a semiinsulating electrode [41].

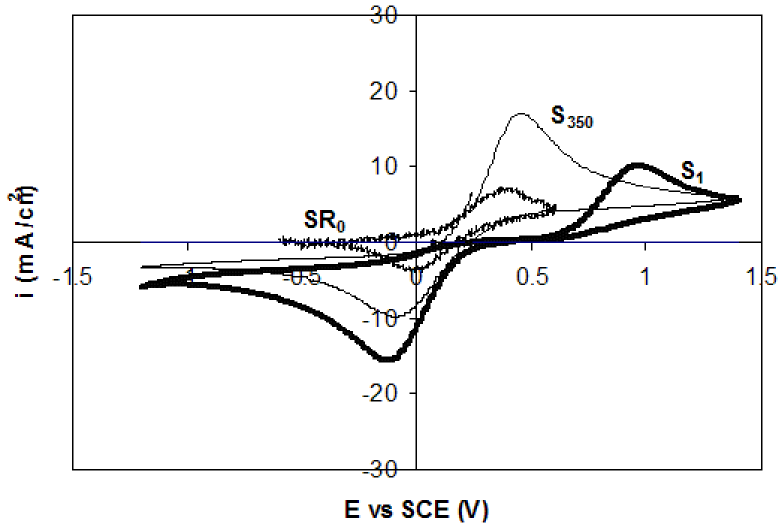

Figure 6.5. *Comparison between cyclic voltammetries in ferro/ferrycyanide solution obtained after 1 hr, 350 hrs, and after the sample was maintained at rest for 5 months (SR_0). Scan rate: 100 mV/s.*

Moreover, the separation between the anodic and cathodic peaks is about 1 V and the peak potential is strongly depending from the scan rate, indicating a slow charge exchange process between the solution and the electrode.

Several authors reported a strict relationship between the ageing time and the electrochemical properties of *BDD* electrodes. Duo et al. [17] proposed that the variation of *BDD* electrode is related to the oxidation of the sp^2 states present in the surface leading to a "non-active" polycrystalline diamond surface. Other authors [40] asserted that the changes in the *BDD* electrodes during the anodic process are related to the variation of the high concentration of H at the surface and to the terminations of the surface itself.

As it well known, an excess of H, which is used to stabilise B in the lattice, may result during the film deposition of *BDD*, so that at the electrode surface, the H concentration is higher than that of B [42-45]. During the *HFCVD* growth process the H atoms can form B-H pairs which gives rise to a passivation of B acceptors. As suggested by some authors [42], two different types of behaviour of H can be supposed: H^+B^- dimers, that is H strongly bonded to B, and H^-h^+ pairs, in which H is linked to the holes and works as an acceptor. Depending on the superficial state of the film and on the electrode potential, these different H atoms could be involved in the charge transfer.

In such a case, H atoms could produce H^-h^+ pairs in the first layer of the film (about 10 nm) [46-47]. During the first times of oxidation, the concentration of H and H^- would be depleted at the electrode surface, because the weakly bonded H is oxidised to H^+ and released to the solution.

As the oxidation proceeds, an increasing depletion of H occurs, especially in the superficial region, and after about one hour, a minimum of current is measured and a corresponding high resistivity superficial region is originated in which all the excess of H has been removed: the electrode is passivated. It is worth to note that no significant differences have been revealed in the Raman spectra collected during the first working hour, in particular no variation can be detected in the band at 1550 cm^{-1} attributed to *G* mode of graphite phase.

A different behaviour is observed at more aged samples. Figure 6.6 shows the trend of potentiodynamic curves obtained at these samples which is increasing with the working time.

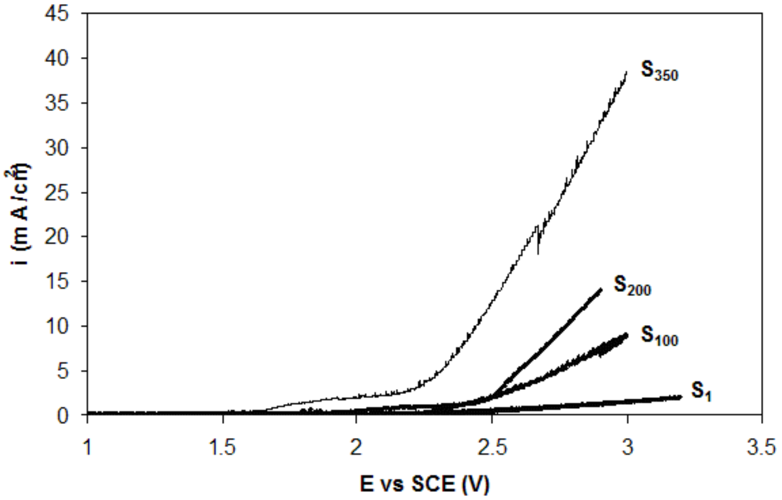

Figure 6.6. *Trend of current density vs potential curves obtained in sulphuric acid at differently aged samples.*

At the same time, decreasing resistance values are obtained from the fitting procedure of the *EIS* data (Table 6.1), ranging from about 200 Ω at S_1 to 2 Ω at S_{350}. In accordance with these data, a second loop reappears in the *EIS* spectrum at S_{350} assessing the increased relevance of the charge transfer resistance with respect to that of the film. Moreover, cyclic voltammetries more regular are obtained (Figure 6.5). In Table 6.2 the values of the peak potentials are resumed, as well as the ratio Ia/Ic between the related anodic and cathodic currents measured at different potential scan rate and at differently aged samples. Even if the observed peak separation (ΔEp) was found to be always higher than that corresponding to one electron-transfer reaction kinetics of ferri/ferrocyanide (59 mV), it tends to decrease at more aged electrodes, as well as the dependence of the peak potentials on the scan rate tends to be less evident as the working time increases.

Sample	*Scanrate* (mV/s)	E_{pa} (V)	E_{pc} (V)	ΔE_p (V)	I_a/I_c	K^0 (cm/s)
S_1	20	0.91	-0.15	1.06	0.53	$3.2\text{x}10^{-5}$ $1.4\text{x}10^{-4}$
	50	0.99	-0.24	1.23	0.59	
	100	1.11	-0.32	1.43	0.55	
S_{100}	20	0.39	-.12	0.51	0.81	$9.5\text{x}10^{-5}$ $1.2\text{x}10^{-5}$
	50	0.4	-.19	0.59	0.96	
	100	0.46	-.25	0.71	0.92	
S_{350}	20	0.28	0.12	0.16	1.5	$2.5\text{x}10^{-4}$ $4.0\text{x}10^{-4}$
	50	0.31	0.09	0.22	1.3	
	100	0.33	0.08	0.25	1.3	

Table 6.2. *Quantitative data from voltammetric runs at different aged samples:* E_{pa}, E_{pc}*: potential of the anodic and cathodic peaks;* ΔE_p *separation between anodic and cathodic peaks,* I_a/I_c *ratio between the anodic and cathodic peak currents,* K^0*: kinetic constants of anodic (up) and cathodic reaction (down).*

Increasing values of the kinetic constants related to the oxidative process from about $3x10^{-5}$ to $4x10^{-4}$ cm/s are calculated from these data at S_1 and S_{350} respectively. Moreover, the ratio between the anodic and the cathodic peak currents, which was 0.5 at the newly prepared sample, tends to be greater than unity at the sample which worked 350 hrs.

Useful information can be derived from Raman analysis in order to interpret this behaviour. Drastic changes are observable in the spectrum of sample S_{350}, compared with that of S_0 in Figure 6.2: the appearance of a new broad band centred at about 500 cm^{-1} and a great enhance of the band at 1200 cm^{-1} were measured, whereas no variation in the bands assigned to graphite can be detected also after longer anodic treatment. As reported in a previous work [48], the observed downshift and the increasing asymmetry of the 1332 cm^{-1} diamond peak can be related to an increasing in the acceptor levels concentration. Actually, in the heavily doped *BDD* samples this band was assigned by numerous authors to the so-called Fano’s interaction generated by quantum mechanical interference between the discrete phonons state and the interband electronic continuum [49-53]. The Fano’s interaction is strictly related to the acceptor level concentration and its increasing during the anodic process indicates that the acceptor level concentration increases too. However, no new B atoms have been added to the lattice so that the increase of the Fano interaction has been correlated to the increased concentration of “free” B levels [48]. During long anodization processes, the B-H complex can dissociate following two different reactions [54]:

$$B{:}H \rightarrow B^- + H^+ \qquad (6.1)$$

$$B{:}H \rightarrow B^- + H^0 + h^+ \qquad (6.2)$$

Both the processes can make free the acceptor levels associated to the B atoms, giving rise to the observed increase of conductance, as well as the great enhancement of the oxidation kinetic constant and the increased symmetry of voltammetric curves for the reaction $Fe(CN_6)^{-3}/Fe(CN)_6^{-4}$.

The bands at 500 cm^{-1} as well as the band at about 1200 cm^{-1} can be assigned to the increasing of the contribution of a distorted diamond structure [35]. In particular the band at 1200 cm^{-1} seems formed by two different contributions: the sp^3 contribution of distorted diamond, i.e. the $q \neq 0$ phonons activated by disorder at 1260 cm^{-1} and 1175 cm^{-1} (the maximum in the VDOS of diamond at L and X point, respectively) and the sp^2 contribution at 1150 cm^{-1} assigned to trans-polyacetylene lying in the grain boundaries. All these bands rise with the *BDD* anodic working time and this can be explained by the occurring of the reactions (6.1) and (6.2). Actually, the distorted diamond can be related to the vacancies of H atoms close to the B atoms. B atoms are included in the lattice as sp^2 terminations and the presence of the H brings the valence to sp^3; the diamond structure will be distorted if B without H is included in the lattice. At the same time, an increase of free H atoms in the lattice can form trans-polyacetylene segments at the grain boundaries and at the surface [36].

Particular attention has to be paid to examine the behaviour of the sample left at rest for a certain time. The trend of potentiodynamic curves obtained at this sample is shown in Figure 6.7, whereas the related *EIS* spectrum and the voltammetry were compared in Figure 6.4 and 6.5 with the behaviour registered before the period of rest.

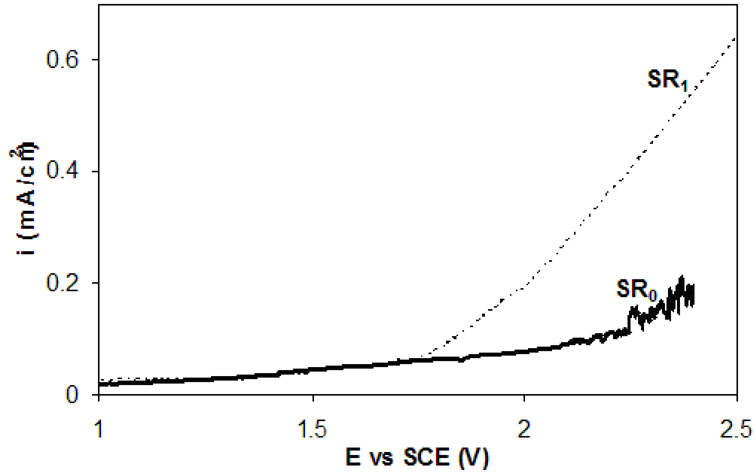

Figure 6.7. *Trend of current density vs potential curves at the sample which was left at rest for 5 months (SR$_0$) and after one further hour of ageing (SR$_1$).*

It is worth to be noticed that the voltammetry obtained at this sample is still symmetric, but the values of the measured currents are lower than those obtained before the rest. Values of total resistance of the film ranging from 2 Ω to about 40 Ω are measured respectively before and after the rest. The conductivity of the film tends to re-increase if the sample is submitted to one further hour of oxidative ageing (SR_1 sample, Figure 6.7).

Nevertheless, the results seem to globally indicate that the main effect of the period of rest is a decrease of conductivity.

Once more, Raman results can be useful to explain the particular behaviour which, in our opinion, is hardly explained only on the basis of possible formation and removal of graphitic points. In particular, the range of major interest in the spectrum of the sample SR_0 is presented in Figure 6.8, compared with that of sample S_{350}: a lower contribution of sp^2 and distorted sp^3 vibration (at 1150 cm^{-1} and 1250 cm^{-1}, respectively) is measured at SR_0 sample that could be interpreted as a partial rearranging of the lattice.

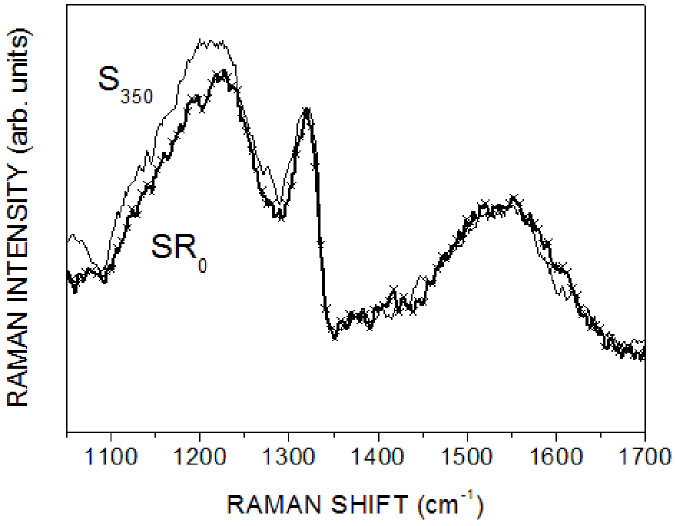

Figure 6.8. *Raman spectra of the sample after 350 anodic working hour (S_{350}) and of the same sample after 5 months at rest (SR_0).*

Actually, during the oxidation process a concentration gradient of H is originated near the surface region, due to the continuous removal of H which is oxidised to H^+ and released to the solution. Thus, a depletion zone is originated in the H concentration profile, near the electrode surface, which gives rise to a slow diffusion process of H atoms from the bulk to the surface and to a consequent decrease of the concentration gradient. This slow diffusion process should be taken into account to explain the results obtained after the samples remained at rest for about 5 months. We suppose that during the diffusion path, the H atoms are captured by the B atoms giving rise to the improvement of the reticular structure observed by the Raman spectra analysis. At the same time, the partial compensation of B atoms could justify the decrease of the free acceptor levels revealed by the Raman analysis and the decreased conductivity measured at these samples.

This increasing in conductivity can also be the indirect reason for the observed trend of the *EIS* spectrum at the SR_0 sample. An equivalent circuit including a new element (C_2R_2 in Table 6.1) is able to describe the experimental data, whereas the capacitive answer of the electrode/solution interface is always represented by a Warburg element. The new element which appears in the spectrum can be reasonably attributed to the capacitive answer of the grain boundaries at which poly-acetylene terminations were originated during the ageing tests: this was not evident in the spectrum of S_{350} just because, in that case, the individuation of the two contributions (bulk and boundary grains) was hindered by the higher value of the charge transfer resistance which partially masked the capacitive answer of the film.

6.3.2 Relationship between electronic structure and electrochemical activity

In this section the research was extended: linear sweep voltammetry and impedance spectroscopy measurements were carried out at less doped (*LD*) samples (1300 ppm of B), aiming at improved characterization of the electronic structure of the samples to reveal a possible relation between semiconductor properties and kinetic behaviour in redox solution. Also in this case the outer-sphere redox reaction of ferro/ferri cyanide was used to test the activity of the surface towards the charge transfer, while specific runs carried out in sulphuric acid were devoted to obtaining information on the electronic structure of the samples.

6.3.2.1 Mott-Shottky analysis - Runs in sulphuric acid

To get information on the electronic structure of the samples, the Mott Shottky (*MS*) analysis was performed through *EIS* carried out in a wide range of potential. As reported in chapter 2, the Mott-Shottky analysis is based on the assumption that in depletion conditions, the capacitance of the space charge layer is very low with respect to that associated with the diffusion layer, which may be, in turn, completely ignored.

In such conditions it can be demonstrated that:

$$\frac{1}{C_{SC}^2} = \frac{2}{q\varepsilon\varepsilon_0 N_a A^2}\left(\left|E - E_{fb}\right| - \frac{kT}{q}\right) \tag{6.3}$$

in which C_{sc} = capacitance of the space charge layer; q = electron charge; ε = dielectric constant of diamond; ε_0 = permittivity of free space; A= area of the electrode; E applied bias potential; E_{fb}= flat band potential; N_a= acceptor concentration; k = Boltzman constant, and T = absolute temperature.

The reciprocal of the square of the capacitance per unit area gives a straight line when plotted as a function of the electrode potential: the acceptor concentration can be easily derived from the slope of the straight lines, while the flat band potential E_{fb} can be determined by extrapolation to $1/C^2=0$.

To obtain reliable data for *MS* analysis, impedance data for new and aged samples were obtained in the wide range of water stability window (Figure 6.9): the low faradaic currents measured in this range provided favourable conditions for the measurement of the impedance diagrams. In fact, in the absence of appreciable faradaic current, *EIS* measurements performed at potential lower than the flat band potential value can give useful information on the depletion layer charge distribution at p-semiconductors: in particular, just one semicircle should appear in the Nyquist diagram corresponding to the capacitive response of the space charge region [55].

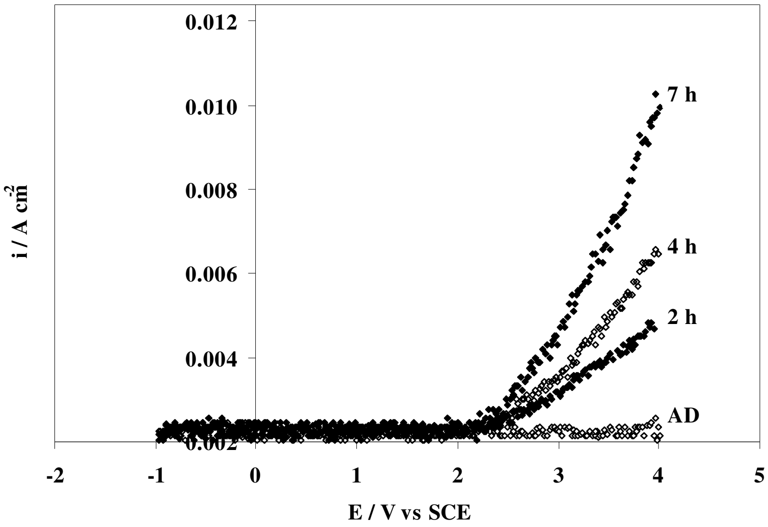

Figure 6.9. *Trend of linear sweep voltammetries (100 mV* s^{-1}*) in sulphuric acid at differently aged samples*

Examination of the Nyquist plots shown in Figure 6.10 shows that the behaviour of the "as deposited" *(AD)* samples is quite different from the ideal: in a wide range of potential two semicircles are always present, even at potentials far from the flat band value.

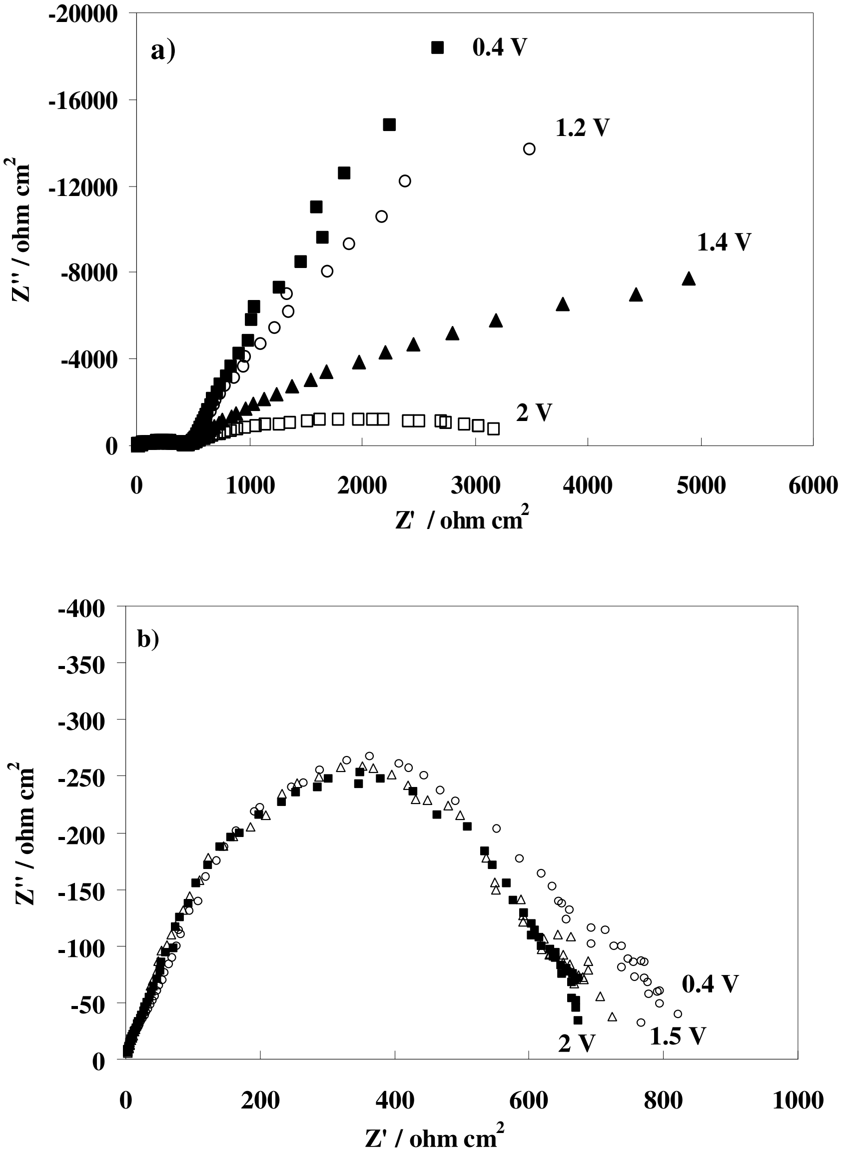

Figure 6.10. *Nyquist plot in sulphuric acid at AD (a) and aged (b) samples*

The parameters of the equivalent circuits utilised to fit the experimental data (Table 6.3) indicate that the high frequency semicircle may be attributed to the response of a passivated layer since its capacitive term is scarcely influenced by potential [42].

Potential /V vs SCE	Y_{01} /μS s^n	n_1	R_1 /Ω cm^2	Y_{02} /μS s^n	n_2	R_2 /MΩ cm^2
0.4	0.23	0.88	461	11.02	0.93	5.76
0.8	0.22	0.89	461	12.20	0.92	0.97
1.2	0.23	0.88	452	13.65	0.92	0.35
1.4	0.21	0.89	449	21.22	0.85	0.03
1.8	0.22	0.89	458	38.41	0.76	0.012

Table 6.3. Values of the fitting parameters evaluated from the equivalent *(R(QR)(QR))* circuit at different potentials.

Furthermore, the whole response of the electrode/solution interface may be correlated to the low frequency loop: as the potential is increased the capacitance component increases and, at the higher potential values, the effect of the capacity of the Helmoltz layer can also be included in the response. In such conditions, *MS* analysis is hardly applicable; indeed, difficulties in the application of this analysis at *BDD* electrodes are not infrequent [42,56-59]. In the vicinity of the flat band potential, the capacitance term is extremely sensitive to substrate polarisation due to change in the space charge within the semiconductor. Reliable data can only be obtained far from E_{fb}, so its value must be calculated by an extrapolation method. Following the suggestions of some authors [55,57], more reliable information can be obtained from the resistance component of the circuit, which, in depletion conditions, assumes very high values. The trend of *1/R* with the potential can be effectively used: its value is almost zero in all the depletion region and suddenly rises to almost infinity when the potential approaches E_{fb}, which in turn can be evaluated without any extrapolation procedure. An example of 1*/R vs E* data for the *AD* sample is shown in Figure 6.11 from which the sharp variation of conductance is noticeable at about 1.2V.

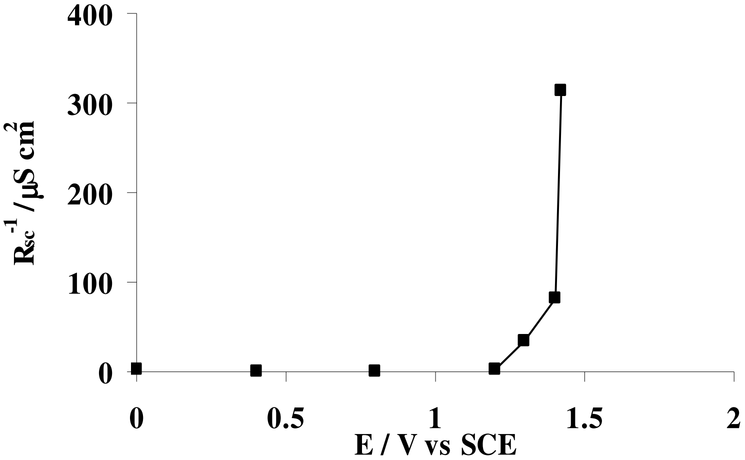

Figure 6.11. Trend of the reciprocal of the depletion layer resistance for the flat band potential determination

When aged samples are considered (Figure 6.10b), the effect of the passivated layer is less evident (the high frequency loop is absent) and a more linear trend of the *MS* plot is obtained. Figures 6.12a and 6.12b show the trend of *MS* data calculated for aged *LD* and *HD* samples.

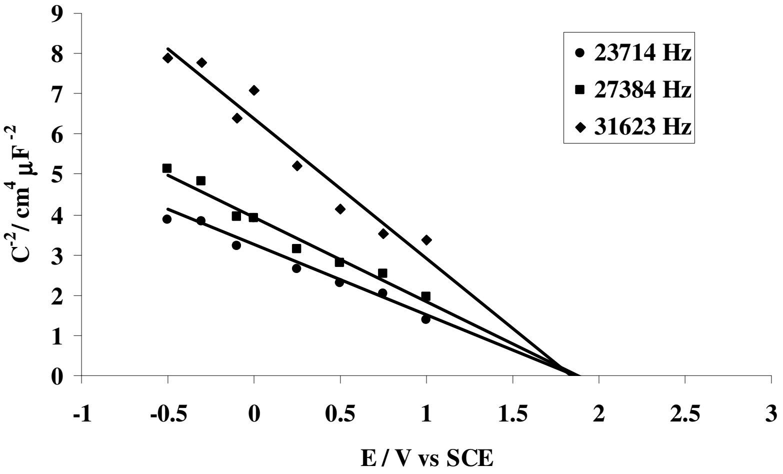

Figure 6.12.a Mott Shottky plot obtained from EIS data at various frequencies, at LD aged samples.

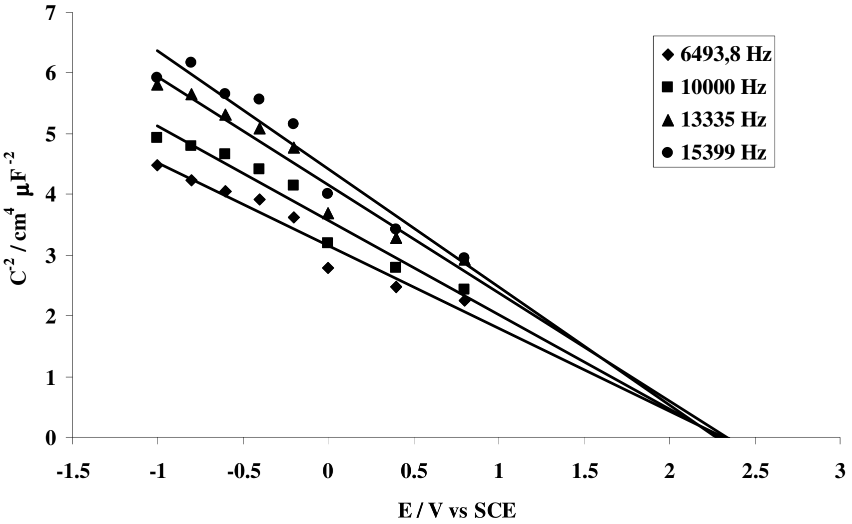

Figure 6.12.b *Mott Shottky plot obtained from EIS data at various frequencies, at HD aged samples.*

As is often reported for semiconductor/electrolyte interfaces [59], in the present case frequency dependent capacitances are observed here. Frequency dispersion may be due to a combination of factors such as surface roughness and dielectric relaxation phenomena in the depletion layer, which can give rise to a frequency dependent dielectric constant [60].

Table 6.4 resumes the values of acceptor density and flat band potential calculated from the *MS* plot for *HD* and *LD* samples at different ageing times.

Sample	Low doped		Highly doped	
	LD_{AD}	LD_{7hr}	HD_{2hr}	HD_{350hr}
Flat band potential / V vs SCE	1.2	1.8	1.3	2.5
Acceptor density / cm^{-3}	$3.0x10^{18}$	$1.0\ x10^{19}$	$1.1x10^{19}$	$1.9\ x10^{19}$
Conduction band / eV	-0.5	-1.2	-0.7	-1.6
Valence band / eV	-5.8	-6.5	-6.1	-7

Table 6.4. *Parameters deduced from the Mott-Shottky analysis for the different samples (subscripts indicate the ageing time)*

The table also reports the energy levels of conduction and valence bands, which were calculated by the following:

$$E_{BV} = E_{BP} + KT \ln \frac{N_a^{SC}}{N_{BV}} \tag{6.4}$$

where N_a represents the acceptor concentration in the space charge deduced from the *MS* plot, and N_{BV} is the effective density of the states in the valence band, which is a characteristic of the material (for diamond $N_{BV} = 10^{19}$ cm^{-3}).

As seen from data in Table 6.4, the oxidative treatment generates a shift in flat band potential to more positive values, as well as an increase in the concentration of the acceptors.

6.3.2.2 Electrochemical activity – Runs in ferro/ferri cyanide

AD samples - Figures 6.13a and 6.13b show the Nyquist plots obtained in ferro/ferri cyanide solution at different potentials for *AD* sample.

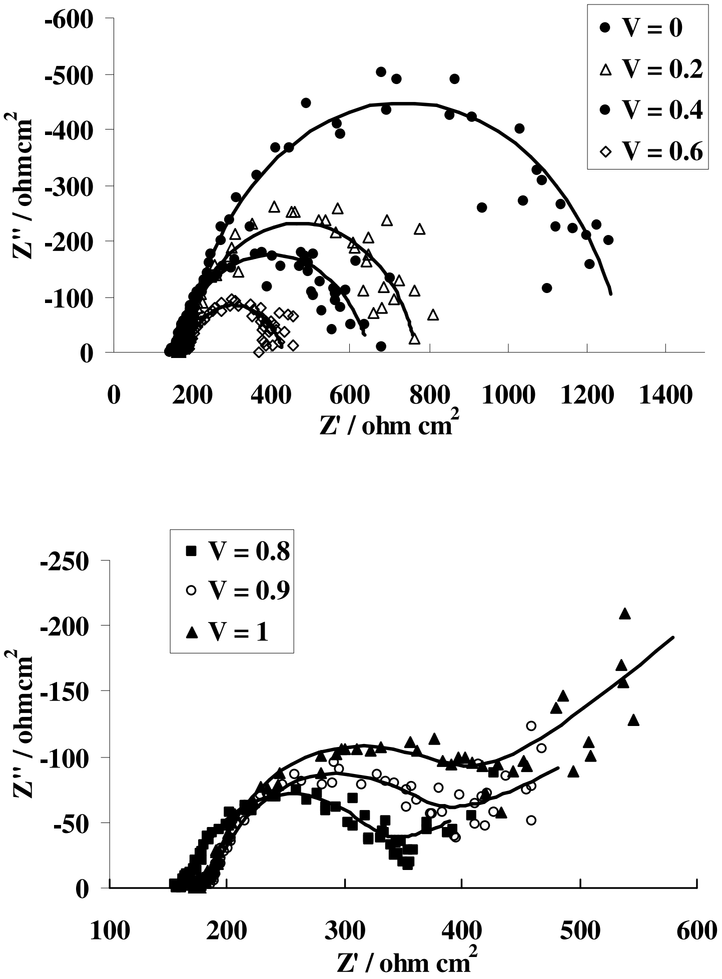

Figure 6.13. *Nyquist plot in ferro/ferri cyanide at AD sample at different potential bias. Full lines are calculated by fitting experimental data with equivalent circuits response.*

Full lines were obtained by fitting the experimental data to suitable equivalent circuits by using ZsimpWin software (Table 6.5). As can be observed, just one semicircle prevails up to a certain potential value, the global trend indicating a charge-transfer controlled process [61]. In fact, the low-frequency cut off on the real axis was found to decrease exponentially with the potential, according to a Buttler Volmer trend. At potential greater than 0.7 V the trend is inverted: the intercepts of the circles increase with the potential and a linear trend is registered at lower frequency range, which could indicate a mass transport control: a Warburg element W has to be inserted in the equivalent circuits to interpret data in this range of potential.

Potential / V vs SCE	Equivalent circuit	Parameters			
		Y_0 /S s ^{n}	n	R /Ω cm^2	W /S s $^{0.5}$
0.1	R_s(QR)	2.1.x10^{-5}	0.83	900	--
0.2	R_s(QR)	2x10^{-5}	0.84	597	--
0.4	R_s(QR)	3.4x10^{-5}	0.78	499	--
0.6	R_s(QR)	4.1x10^{-5}	0.75	253	--
0.7	R_s(QR)W	2.9x10^{-5}	0.82	172	0.016
0.8	R_s(QR)W	2.9x10^{-5}	0.83	169	0.0054
0.9	R_s(QR)W	3.6x10^{-5}	0.80	200	0.003

Table 6.5. *Values of the fitting parameters evaluated from the equivalent circuit at different potentials at AD sample in ferro/ferri cyanide solution.*

On the basis of the results obtained at *HD* samples, the observed behaviour can be justified by the lower doping level of *LD* samples examined in the present work: the lower excess of H, added in the structure to compensate B, determines the absence of the first state of initial high conductivity which was observed in *HD* samples. The *AD* sample should be in a passivated state, determined by a superficial layer where all B atoms are compensated by H. Thus, low current and high impedance values are registered at the surface.

To analyse the charge transfer activity of the different samples, data from voltammetric runs in ferro/ferri cyanide can also be considered. Particular attention has to be paid to the first voltammetric cycle registered at the *AD* sample (Figure

6.14): just a reduction peak was observed, while no signal of the corresponding peak was obtained in the oxidative scan, although the substrate is a p-type semiconductor.

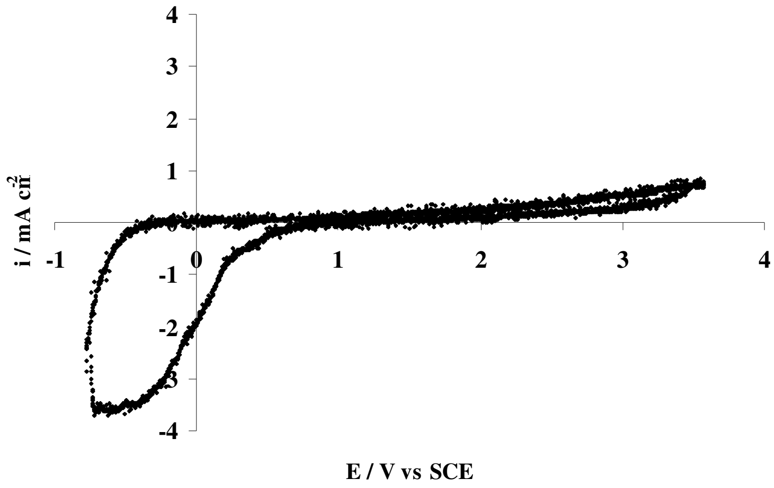

Figure 6.14. *Cyclic voltammetry at 100 mV s^{-1} in ferro/ferri cyanide at AD sample*

So on the basis of the Gerisher electronic model [62], the current density measured at the electrode surface of a semiconductor can be expressed as:

$$i^{-}(E) = -zF\int k(E)N_o(E)D_{ox}(E)dE \tag{6.5}$$

where k is the transition coefficient, N_O is the number of occupied states in the conduction band, and D_{ox} is the number of vacant states due to oxidising species in solution. Naturally, a reciprocal expression will give the oxidation current i^{+}.

In our case, N_O is extremely low and should result in a vanishing small cathodic current, a prediction which is in complete disagreement with results in Figure 6.14. Other authors [63] have also underlined the unexpected absence of charge carrier supply limitations in reduction processes at *BDD*. In their case, having used solutions in which just the oxidised species was present, these authors justified the observed trend by assuming a direct involvement of the valence band of diamond in the charge exchange. In the present case, as specified above, a E_{fb} value of about

1.2V was estimated, which leads to a position of the valence band at about – 6 eV. Moreover, since the solution is equimolar in oxidised and reduced species, the Fermi level of the redox couple is surely higher than the valence band level, so a direct exchange of carriers has to be excluded; in any case, it could not explain the strong asymmetry between anodic and cathodic loops in the voltammetry.

Two different arguments can be used to justify the observed trend of current: on the one hand the formation of new superficial states originated by H which acts as donor:

$H \rightarrow H^+ + e^-$ (6.6)

gives electrons which may be available for cathodic reaction. In this case the current may be expressed by the Equation (6.5) which is modified by a term g_s, which represents the surface generation rate of the charge carriers. An analogous justification was given to explain the behaviour of p-silicon in reduction reactions [55].

On the other hand, depending on the applied potential, either the displacement of the superficial passivated layer within the bulk or its maintenance at the surface can be obtained [64], the two situations being strongly dependent on the charge of the H which is generated by the B:H complex reactions (6.1) and (6.2).

In the specific case, during the cathodic scan the H present in the structure as H^+ should drift in the electric field, thus being swept out of the depletion layer, and finally recaptured at the end of the space charge region by an unpassivated boron acceptor. As a consequence, the boron acceptors in the depletion layer will be reactivated and the passivated layer will be shifted deeper into the bulk. This may explain why the application of a reducing potential, although reverse biasing for a p-type semiconductor, leads to local reactivation of the surface with consequent increase in current, whereas an oxidative potential, which should be direct biasing, tends to maintain the H^+ in the passivated layer and to limit the observed anodic current.

Aged samples - As the working time increases, a net increase in anodic current is measured. At the same time, as observed from Figure 6.15, the impedance registered in the *EIS* measurements falls and the diffusive regime is achieved at a potential lower than that for the *AD* sample.

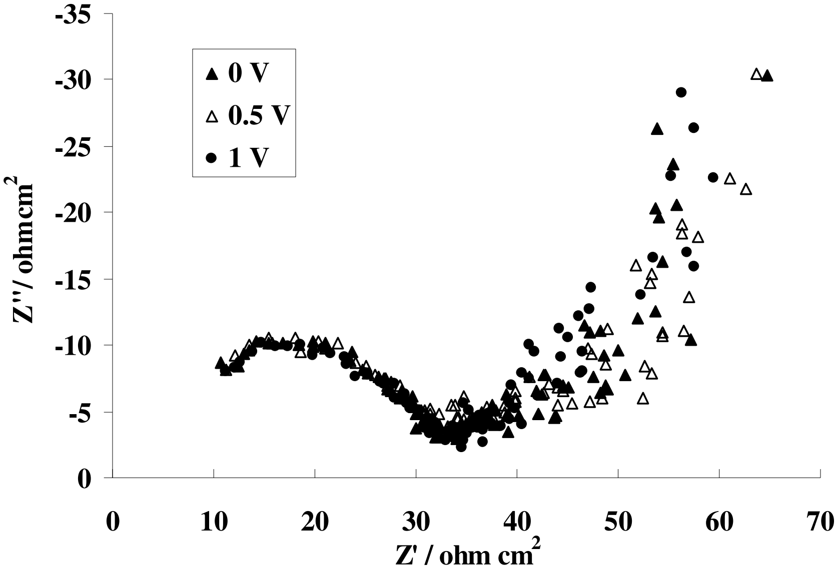

Figure 6.15. *Nyquist plot in ferro/ferri cyanide at aged sample at different potential bias.*

Moreover, analogously to what was observed for *HD* samples, cyclic voltammograms in ferro/ferri cyanide are more regular and the oxidative peak appears in the loop, indicating a more activated surface; the peaks are more symmetrical (Figure 6.16), although still widely separated, indicating that reversibility of charge transfer is not yet achieved.

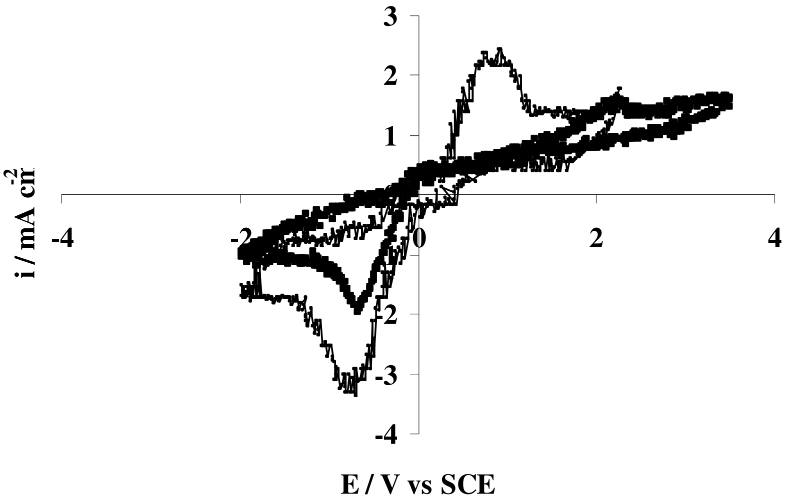

Figure 6.16. *Cyclic voltammetries (100 mV s^{-1}) at aged samples in ferro/ferri cyanide solutions.*

Analysis of the electronic structure of the sample is useful in determining the factors that play the major role in the observed behaviour. As reported above, one of the main effects of the ageing is the increase in acceptor concentration, which in turn leads to an increase in current (Equation 6.5). However, the shift of the valence band towards energetic values far from the Fermi level of the solution suggests that the valence band is not directly involved in the charge exchange, so new states, caused by superficial defects or changes in the grain boundaries of the polycrystalline diamond film, could be responsible for the observed metallic-like character.

This argument is supported by the *EIS* measurements obtained at aged samples which were left at rest for some months. A new capacitive element is observed in the Nyquist diagram (Figure 6.17), which was attributed to the capacitive response of the grain boundaries at which poly-acetylene terminations originated during the ageing tests. Due to the high ratio R_{ct}/R_F between charge transfer and film resistances, the capacitive response of the film was not visible in the previous spectra, which were registered before the rest period of the samples.

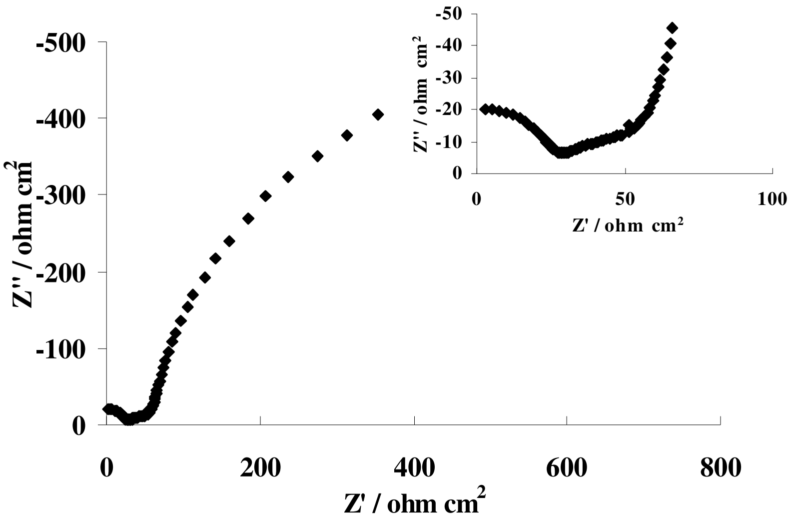

Figure 6.17. *Nyquist plot in ferro/ferri cyanide at an aged sample which was left at rest for 1 month.*

Analogous behaviour observed at more doped samples was justified by considering that after a sufficiently long period of time, the H concentration gradient, originating during the previous working period, was partially compensated by a slow diffusive process of H from bulk to surface. This caused a decrease in conductivity due to the partial re-compensation of B atoms and the consequent decrease in the free acceptor levels. Thus, the increased value of film resistance allows its capacitive response to be revealed.

6.4 Conclusions

In discussing the behaviour of *BDD* electrodes as the ageing time is increased, we start from the results obtained at highly doped samples. The results showed that the behaviour of the samples, as well as the changes in their electronic structure, can be explained by the movement of H which is contained in the doped-diamond film. So, the decrease of conductivity, observed in the first oxidation times, can be connected to the removal of the weakly-bonded H which is added in strong excess to stabilise B during the film deposition. During oxidation, an increasing depletion of H occurs, until a passivated state is reached, in which a superficial region with high resistance is originated when all the excess of H is removed.

The removal of the strong-bonded H of the B-H dimers could be the responsible for the increased availability of the acceptor levels measured at more aged samples, which could explain the observed increase of conductivity and the great enhancement of the oxidation kinetic constant for the reaction $Fe(CN_6)^{-3}/Fe(CN)_6^{-4}$.

As the working time is increased, the oxidative process generates an increasing concentration gradient of H, which in turn gives rise to a diffusion process of H from the bulk to the surface of the film. The results of measurements carried out at samples left at rest showed that, after a sufficiently long period of time, a new situation can be reached, in which the concentration gradient may be partially compensated by this slow diffusive process. This causes a decreasing in conductivity due to the partial re-compensation of B atoms and the consequent decrease of the free acceptor levels.

Moreover, it may be worth to consider that H in the structure may be also responsible for the instability of the film when longer oxidation times are considered. Actually, when ageing tests were protracted for several months, the samples presented drastic damaging: some regions looked paler at optical microscope and some small regions were detected in which the diamond film was totally absent. Such a behaviour may be justified by the removal of a great amount of H due to the long oxidative process, that may create strong distortion of the lattice. The increase of sp^2 terminations at the surface can bring to the formation of a graphitic phase at the grain boundaries, and accelerate the degradation of the diamond crystals. In fact, due to the great instability of the graphite at higher oxidative potential, a fast breaking of sp^2 C-C bonds may occur, thus generating the random degradation observed at the sample surface.

The results obtained at medium doped *BDD* show that the behaviour of the sample is similar to that observed at more doped samples. The most significant differences may be related to the lower conductivity of the less doped samples. Because of the lower doping level, the excess of H added to the structure to compensate B is lower. This determines the absence of the first state of initial high conductivity which was observed in highly doped samples. The as deposited sample should be in a passive state determined by a superficial layer where all B atoms are compensated by H. Thus, low current and high impedance values are registered at the surface.

However, this situation tends to be rapidly modified, and as the working time is increased, the samples tend to be more conductive.

Analysis of the electronic structure indicates that the main effect of the oxidative ageing is a shift of the flat band potential to more positive potentials which, in turn, determines a shift of the energy levels of the bands towards more negative values. This excludes direct involvement of the valence band in the charge transfer process.

As was verified at more doped samples, the generation of new superficial states can be reasonably assumed to justify the increased metallic behaviour of the samples.

6.5 References

[1] Y.V. Pleskov, M.D. Krotova, L.L. Bouilov, B.P. Spitsyn, J. Electroanal. Chem. 19 (1987) 228

[2] H.B. Martin, A. Argotia, U. Landau, A.B. Anderson, J.C. Angus, J. Electrochem. Soc., 143, (1996), 133

[3] Y.V. Pleskov, in: R.C. Alkire, D.M. Kolb (Eds.), Advances in Electrochemical Science and Engineering, 8, Wiley-VCH, N.Y. 2003.

[4] G.M. Swain, in: A.J. Bard, I. Rubinstein (Eds), Electroanalytical Chemistry, 22, M. Dekker, N.Y. 2004

[5] G. Foti, Ch. Comninellis, in: R.E White, B.E Conway, M.E. Gamboa-Adelco (Eds.), Modern Aspects of Electrochemistry, 37, Kluwer Academic/Plenum Publisher, N.Y. 2004

[6] K.B. Holt, A.J. Bard, Y. Show, G.M. Swain, J. Phys. Chem. B. 108 (2004) 15117

[7] A.E. Fischer, G.M. Swain, J. Electrochem. Soc. 152 (2005) B369

[8] G.W. Muna, V. Quaiserova-Mocko, G.M. Swain, Anal. Chem. 77 (2005) 6542

[9] G. W. Muna, N. Tasheva, G.M. Swain, Environ. Sci. Technol. 38 (2004) 3674

[10] K.L. Soh, W.P. Kang, J.L. Davidson, S. Basu, Y.M. Wong, D.E. Cliffel, A.B. Bonds, G.M. Swain, Diamond and Rel. Mater. 13 (2004) 2009

[11] J. Wang, G. Chen, M.P, Chatrathi, A. Fujishima, D. A. Tryk, D. Shin, Anal. Chem. 75 (2003) 935

[12] C. Terashima, T. N. Rao, B. V. Sarada, D. A. Tryk, A. Fujishima, Anal. Chem. 74 (2002) 895

[13] C. Terashima, T. N. Rao, B. V. Sarada, Y. Kubota, A. Fujishima, Anal. Chem. 75 (2003) 1564

[14] K. Honda, Y. Yamaguchi, Y. Yamanaka, M. Yoshimatsu, Y. Fukuda, A. Fujishima, Electrochim. Acta 51 (2005) 588

[15] T. Kondo, K. Honda, D.A. Tryk, A. Fujishima, J. Electrochem. Soc. 152 (2005) E18

[16] A. Manivannan, N. Spataru, K. Arihara, A. Fujishima, Electrochem. and Solid-State Letters 8 (2005) C138

[17] I. Duo, C. Levy-Clement, A. Fujishima, Ch. Comninellis, J. Appl. Electrochem. 34 (2004) 935

[18] G. Siné, Ch. Comninellis, Electrochim. Acta 50 (2005) 2249

[19] E. Mahé, D. Devilliers, Ch. Comninellis, Electrochim. Acta 50 (2005) 2263

[20] L. Ouattara, M.M. Chowdhry, Ch. Comninellis, New Diamond and Frontier Carbon Technol. 14 (2004) 239

[21] Yu. V. Pleskov, Yu.E. Evstefeeva, M.D. Krotova, P.Y. Lim, S.S. Chu, V.G. Ral'chenko, I.I. Vlasov, (…), H.C. Shi, Russ. J. of Electrochem. 41 (2005) 337

[22] Yu.V. Pleskov, Yu.E. Evstefeeva, V.P. Varnin, I.G. Teremetskaya, Russ. J. Electrochem 40 (2004) 886

[23] Yu.V. Pleskov, Yu.E. Evstefeeva M.D. Krotova, V.Ya. Mishuk, V.A. Laptev, Yu.N. Palyanov, Yu.M. Borzdov, J. Electrochem. Soc. 149 (2002) E260

[24] Yu.V. Pleskov, M.D. Krotova, Yu.E. Evstefeeva, V.G. Ral'chenko, I.I. Vlasov , A.V. Khomich, Russ. J. Electrochem 37 (2001) 1123

[25] N. Bensalah, A. Gadri, P. Canizares, C. Saez, J. Lobato, M. A. Rodrigo, Environ. Sci. Technol. 39 (2005) 7234

[26] X. Chen, G. Chen, F.Gao, P.L. Yue, Environ. Sci. Technol. 37 (2003) 5021

[27] C.A. Martínez-Huitle, S. Ferro, A. De Battisti, J. Appl. Electrochem. 35 (2005) 1087

[28] A.M. Polcaro, A. Vacca, S. Palmas, M. Mascia, J. Appl. Electrochem. 33 (2003) 885

[29] M.A. Rodrigo, P.A. Michaud, I. Duo, M. Panizza, G., Cerisola, Ch. Comninellis, J. Electrochem. Soc. 148 (2001) D60

[30] Y.V. Pleskov, Y.E. Evstefeeva, M.D. Krotova, A.V. Laptev, Electrochim. Acta 44 (1999) 3361

[31] I. Duo, A. Fujishima, and Ch. Cominellis, Electrochem. Commun. 5 (2003) 695

[32] P.G. Buckley, T.D. Moustakas, L.Ye, J. Varon, J. Appl. Phys. 66 (1989) 3595

[33] P. Gonon, E. Gheeraert, A. Deneuville, F. Fontaine, L. Abello and G. Lucazeau, J. Appl. Phys. 78, (1995) 7059

[34] R.J. Nemanich, J.T. Glass, G. Lucovsky and R.E. Shroder, J. Vac., Sci. Technol. A 6 (1988) 1783

[35] S. Prawer, K.W. Nugent, D.N. Jamieson, J.O. Orwa, L.A. Bursill, J.L. Peng, Chem. Phys. Lett. 332 (2000) 93

[36] A.C. Ferrari, J. Robertson, Phys. Rev., B 63 (2001) 121405R

[37] E. Ehrenfreund, Z. Vardeny, O. Brafman, B. Horovitz, Phys. Rev., B 36 (1987) 1535

[38] R. Pfeiffer, H. Kuzmany, N. Salk, B. Gunther, Appl. Phys. Lett. 82 (2003)

[39] Y. Hishiyama, H. Irumano, Y. Kaburagi, Y. Soneda, Phys. Rev. B 63 (2001) 2454061

[40] R. Ramesham, Thin Solid Films 315 (1998) 222

[41] R. Ramesham, M.F. Rose, Diamond Relat. Mater. 6 (1997) 17

[42] T. Kondo, K. Honda, D.A. Tryk, A. Fujishima, Electrochim. Acta 48 (2003) 2739

[43] F. Weerdt, Y.N. Palyanova, A.T. Collins, J. Phys., Condens. Matter 15 (2003) 3163

[44] K. Iakoubovskii, A. Stesmans, J. Phys., Condens. Matter 14 (2002) R 467

[45] H.J. Looi, M.D. Whitfield, J.S. Foord, R.B. Jackman, Thin Solid Films 343 (1999) 623

[46] R. Zeisel, C.E. Nebel, M. Stutzmann, Diamond Relat. Mater. 9 (2000) 413

[47] C. Uzan-Saguy, A. Reznik, C. Cytermann, R. Brener, R. Kalish, E. Bustarret, M. Bernard, A. Deneuville, E. Gheeraert, J. Chevallier, Diamond Relat. Mater. 10 (2001) 453

[48] P.C. Ricci, A. Anedda, C.M. Carbonaro, R. Corpino, Thin Solid Films 482 (2005) 311

[49] Y.Wang, H. Li, Y. Xiong, S. Zhang Zlin, K. Feng, Diamond Relat. Mater. 9 (2000) 1708. 446

[50] F. Pruvost, A. Deneuville, Diamond Relat. Mater. 10 (2001) 531

[51] K. Ushizawa, M.N. Gamo, F. Watanabe, I. Sakaguchi, Y. Sato, T. Ando, J. Raman Spectrosc. 30 (1999) 957. 449

[52] M. Cardona, G. Guntherodt, Light Scattering in Solids IV, Springer, Berlin, 1984

[53] J.W. Ager, W. Walukiewicz, M. McCluskey, M.A. Plano, M.I. Landstrass, Appl. Phys. Lett. 66 (1995) 616

[54] S.P. Mehandru, A.B. Anderson, J. Mater. Res. 9 (1994) 383

[55] M. Chemla, J.F. Dufreche, I. Darolles, F. Rouelle, D. Devilliers, S. Petitdidier, D. Levy, Electrochim. Acta 51 (2005) 665

[56] Yu.V. Pleskov, V.M Mazin, Yu.E. Evstefeeva, V.P.Varnin, I.G Teremetskaya, V.A. Laptev, Electrochem. and Solid-State Letters 3 (2000) 141

[57] V. Bretagna, R. Erre, F. Rouelle, M. Chemla, S. Petitdidier, D. Levy, Electrochim. Acta 47 (2001) 129

[58] G. Pastor-Moreno, D. J. Riley, Electrochim. Acta 47 (2002) 2589

[59] J. van de Lagemaat , D. Vanmaekelbergh, J.J. Kelly, J. Electroanal. Chem. 475 (1999) 139

[60] W.P.F .Gomes Cardon, Progr. Surf. Sci. 12 (1982) 155

[61] Meilin Liu, Zhonglin Wu, Solid State Ionics 107 (1998) 105

[62] H Gerisher, Electrochim. Acta 35 (1990) 1677

[63] A.D. Modestov, Yu.E. Evstefeeva, Yu.V. Pleskov, V.M. Mazin, V.P Varnin, I.G. Teremetskaya, J. Electroanal. Chem. 421 (1997) 211

[64] R. Zeisel, C.E. Nebel and M. Stuzmann, Diamond and Rel. Mater. 9 (2000) 413

Chapter 7

Conclusions

The Thesis is concerned with the study of different materials used as electrodes for evolution of oxygen. This reaction plays a key role in several electrochemical processes: oxygen evolution reaction is very often the most difficult of the two reactions in the water electrolysis and it is the most important side reaction of many other electrochemical applications such as electrosynthesis, incineration of organic pollutants for wastewater treatment and water disinfection.

The different reaction mechanisms of oxygen evolution have been evaluated by studying both “active” and “non-active” electrodes. Strong interactions with hydroxyl radicals exist at active materials and the oxygen evolution reaction occurs via the formation of higher oxides. In contrast, at non active electrodes, the substrate does not participate in the process and the oxidation is assisted by hydroxyl radicals that are weakly adsorbed at the electrode surface.

Actually, many factors affect the electrochemical behaviour of the electrode materials so, depending on the cases, the work was addressed to clarify some of these aspects in light of the results obtained.

When the attention was focused on the spinel-type Ti/Co_3O_4 electrodes obtained by a sol-gel method, particular attention has been paid on the study of the reaction mechanism. The behaviour of cobalt powder electrodes was examined in alkaline solution during oxidative process at different potentials. The results indicated that different redox transitions are possible during the oxidative process leading to Co(III) and Co(IV) containing phases which constituted specific sites for OH- adsorption. The results also confirmed that Co(IV) containing species are the catalytic sites for *OER*. Moreover, the time constants evaluated from *EIS* measurements at different potentials allowed to individuate the transformation Co(III)/Co(IV) as the slowest step in the oxidative process: the diffusion of OH- in the pore solution, slower with respect to the quasi - reversible charge transfer step, limits the whole process. The combination of the equivalent electrical circuit approach with the mathematical modelling of the faradaic impedance was used to derive the kinetic parameters for *OER* at this electrode. A quantitative fitting of the experimental data was performed and an exact physical meaning was maintained for every parameter of the model. The method gave optimum results which were in agreement with data previously obtained from polarization experiments and impedance analysis. These electrodes can be considered as a very attractive anode material for oxygen evolution in alkaline media. However, their catalytic activity and stability can be still increased. One possibility to achieve this goal would be the introduction of an other component in the layer. So, the study will be extended to mixed spinel oxide electrodes.

The experimental results on SnO_2 and SnO_2-RuO_2 electrodes, investigated in acid media during oxidative runs, showed that the properties of the resulting oxide layer are strictly connected with the preparation technique of the mixture. The use of high-energy ball milling to prepare these electrodes demonstrated to be a promising method to produce active powder oxide. Information on the mechanistic scenario underlying the chemical reaction and, indirectly, on the modifications connected with powder particle deformation were derived by cyclic voltammetry, electrical polarization and electrochemical impedance spectroscopy experiments. Significant decrease in the average crystallite size as well as accumulation of structural disorder were measured in the processed powders. According to the equivalent circuit approach, such processes result in an increase in the thin film resistance: the larger grain boundary extension related to the crystallite size decrease determined a corresponding decrease in the charge carrier mobility. At the same time, evidence was found suggesting that the enhanced catalytic activity of processed powders can be related, not only to the grain boundary extension increase, but also to the generation of surface active sites with different reactivity. However, further work is needed to study the catalytic activity of the mixed oxide samples, in particular the possible formation of a single phase solid solution will be verified.

As the non active electrodes were concerned, important results were obtained on the stability of *BDD* anodes. In particular, in order to investigate on their service life, samples of *BDD* with different doping levels, were submitted to ageing tests and the variation of their structure was investigated with time. The results obtained at highly doped *BDD* samples as the ageing time is increased showed that the behaviour of the samples, as well as the changes in their electronic structure, can be explained by the movement of H which is contained in the film. So, the decrease of conductivity, observed in the first oxidation times, was connected to the removal of the weakly-bonded H which is added in strong excess to stabilise B during the film deposition. During oxidation, an increasing depletion of H occurs, until a passivated state is reached, in which a superficial region with high resistance is originated when all the excess of H is removed. The removal of the strong-bonded H of the B-H dimers was assumed to be the responsible for the increased availability of the acceptor levels measured at more aged samples, which explains the observed increase of conductivity and the great enhancement of the oxidation kinetic constant for the reaction $Fe(CN_6)^{-3}/Fe(CN)_6^{-4}$. As the working time is increased, the oxidative process generates an increasing concentration gradient of H, which in turn gives rise to a diffusion process of H from the bulk to the surface of the film. The results of measurements carried out at samples left at rest showed that, after a sufficiently long period of time, a new situation can be reached, in which the concentration gradient may be partially compensated by this slow diffusive process. This causes a decreasing in conductivity due to the partial re-compensation of B atoms and the consequent decrease of the free acceptor levels.

Moreover, it may be worth to consider that H in the structure may be also responsible for the instability of the film when longer oxidation times are considered. Actually, when ageing tests were protracted for several months, the samples presented drastic damaging: some regions looked paler at optical microscope and some small regions were detected in which the diamond film was totally absent. Such a behaviour may be justified by the removal of a great amount of H due to the long oxidative process, that may create strong distortion of the lattice. The increase of sp^2 terminations at the surface can bring to the formation of a graphitic phase at the grain boundaries, and accelerate the degradation of the diamond crystals. In fact, due to the great instability of the graphite at higher oxidative potential, a fast breaking of sp^2 C-C bonds may occur, thus generating the random degradation observed at the sample surface.

The results obtained at medium doped *BDD* show that the behaviour of the sample is similar to that observed at more doped samples. The most significant differences may be related to the lower conductivity of the less doped samples. Because of the lower doping level, the excess of H added to the structure to compensate B is lower. This determines the absence of the first state of initial high conductivity which was observed in highly doped samples. The as deposited sample should be in a passive state determined by a superficial layer where all B atoms are compensated by H. Thus, low current and high impedance values are registered at the surface. However, this situation tends to be rapidly modified, and as the working time is increased, the samples tend to be more conductive.

Analysis of the electronic structure indicates that the main effect of the oxidative ageing is a shift of the flat band potential to more positive potentials which, in turn, determines a shift of the energy levels of the bands towards more negative values. This excludes direct involvement of the valence band in the charge transfer process.

As was verified at more doped samples, the generation of new superficial states can be reasonably assumed to justify the increased metallic behaviour of the samples.

As the future developments of the work are concerned, it can be intriguing to explore the photoelectrocatalytic properties of *BDD* samples. So, the study will be extended to hybrid systems containing *BDD* with the possible application for efficient oxidation of ethanol. This could be of great importance in fuel cell applications.

In all these cases, the results showed that the nature of the anodic material strongly influences the process selectivity and efficiency. Various aspects of electrochemical behaviour must be reviewed for characterising and understanding the electrochemical processes. Active surface area, specific activity, electronic resistance and particle/layer structure are all important properties which need to be optimised in order to achieve high efficiency and performance. Moreover, when we consider electrode materials for industrial applications a compromise between electrocatalytic activity, long-term stability and cost must be achieved. However, the range of improvement of a mono-component can be rather limited. So hybrid systems can be used to modulate the electrode properties through synergetic effects arising from the intimate electronic interaction of the components.

Table of symbols

Roman symbols

A	Surface area	cm^2
A_k	Active area	cm^2
b	Tafel slope	$mV\ dec^{-1}$
C^*	Concentration of specie i in the bulk	$mol\ cm^{-3}$
C_i	Concentration of specie i at the surface	$mol\ cm^{-3}$
C_{di}	Internal differential capacity	$\mu F\ cm^{-2}$
C_{de}	External differential capacity	$\mu F\ cm^{-2}$
C_{dl}	Double layer capacitance	$\mu F\ cm^{-2}$
C_{dt}	Total differential capacity	$\mu F\ cm^{-2}$
C_{sc}	Capacitance of the space charge layer	$\mu F\ cm^{-2}$
D	fractal dimension	-
D_i	Diffusion coefficient of specie i	$cm^2\ s^{-1}$
E	Potential of an electrode vs a reference	V
E^0	Standard potential	V
E_{eq}	Equilibrium potential	V
E_{fb}	Flatband potential	V
E_p	Peak potential	V
f	Frequency of sinusoidal oscillation	s^{-1}
F	Faraday’s constant	$C\ mol^{-1}$
i	Current density	$A\ cm^{-2}$
i_0	Exchange current density	$A\ cm^{-2}$
i_c	Capacitive current density	$A\ cm^{-2}$
i_F	Faradaic current density	$A\ cm^{-2}$
I_p	Peak current	A
I	Current intensity	A
L	Crystallite size	nm
k	Boltzman constant	$J\ K^{-1}$
k^0	Standard rate constant	$cm\ s^{-1}$
k_b	Rate constant of oxidation (backward)	$cm\ s^{-1}$
k_f	Rate constant of reduction (forward)	$cm\ s^{-1}$
n	Electron numbers	-
N	Donor density	cm^{-3}
N	Avogadro's Number	mol^{-1}
q^*	Voltammetric charge	$C\ cm^{-2}$
q_i^*	Inner surface charge	$C\ cm^{-2}$
q_o^*	Outer surface charge	$C\ cm^{-2}$
q_t^*	Total surface charge	$C\ cm^{-2}$
R	Gas constant	$J\ mol^{-1}\ K^{-1}$
R	Resistance	Ω
R_{ct}	Charge transfer resistance	Ω

R_p	Polarization resistance	Ω
R_S	Ohmic solution resistance	Ω
S_e	Number of oxygen evolution sites per unit area	sites cm^{-2}
S_p	Specific surface area of crystallites	$m^2\ g^{-1}$
t	Time	s
T	Absolute temperature	K
Z	Impedance	Ω
Z_F	Faradaic impedance	Ω

Greek symbols

α_a	Transfer coefficient of anodic reactions	-
α_c	Transfer coefficient of cathodic reactions	-
Γ	Number of covered electroactive sites	mol cm^{-2}
Γ_{max}	Saturation number of electroactive sites	mol cm^{-2}
ε	Dielectric constant of diamond	μF/cm
ε	Microstrain content	-
ε_0	Permittivity of free space	μF/cm
η	Overpotential	V
ϑ	Fractional coverage of the adsorbed species	-
λ	Wavelength	nm
λ	Switching time in cyclic voltammetry	s
ν	Potential scan rate	V s^{-1}
φ	Morphology factor	-
τ	Time constant	s
ω	Angular frequency of rotation	s^{-1}

Acronyms

BDD	Boron doped diamond
CNLS	Complex nonlinear least squares
CPE	Constant Phase Element
DSA	Dimensionally stable anode
EIS	Electrochemical impedance spectroscopy
HFCVD	Hot filament chemical vapor deposition
MS	Mott Shottky
OCV	Open circuit potential
OER	Oxygen evolution reaction
SCE	Saturated calomel electrode
SSSRT	Solid state surface redox transitions
XRD	X-ray diffraction